Tectonic Exhumation and Climate Driven Erosion in Extensional Mountain Blocks: Two Examples from California, USA

Cody Curtis Mason

Dissertation submitted to the faculty of the Virginia Polytechnic Institute and State University in partial fulfillment of the requirements for the degree of

Doctor of Philosophy
In
Geosciences

Brian W. Romans. Co-Chair
James A. Spotila. Co-Chair
Benjamin C. Gill
Richard D. Law

April 19th, 2017
Blacksburg, Virginia

Keywords: Sedimentary Systems, Tectonics, Low-temperature Thermochronometry, Cosmogenic Radionuclides, Climate Change

Tectonic Exhumation and Climate Driven Erosion in Extensional Mountain Blocks: Two Examples from California, USA

Cody Curtis Mason

ABSTRACT

The Pacific-North America plate boundary in central and southern California has a complex tectonic history, and constraints are poor for inception of an extensional fault system linked to the southern San Andreas fault, a major tectonic element of this plate boundary. Furthermore, decades of research has shown relationships between climate, tectonics, and surface processes in most orogens across the globe (*e.g.* Alps, Himalaya, Andes, Alaska Ranges), however the role climate plays in modulating erosion and mass fluxes from extensional mountains blocks to sedimentary basins over $10^{4\text{-}5}$ yr timescales is debated. In the eastern California-Walker Lane shear zone, exposures of sedimentary basin fill allow inversion of erosion- and sediment-flux rates from a linked catchment-fan system within an extensional block. In this dissertation, I present two field and geo-thermochronology based studies that explore research topics related by common tectonic setting and geography within the Pacific-North America plate boundary. First I present new low-temperature thermochronology (apatite U-Th-Sm/He) and thermal history modeling to document the kinematic evolution of the Santa Rosa mountains, where the cooling history constrains initiation timing of the west Salton Detachment fault, and the southern San Andreas fault system. I document an age of ca. 8 Ma for exhumation initiation of the Santa Rosa block, from paleodepths of ~4.5–3 km, at vertical rates of ~0.15–0.36 mm/yr, accelerating to ~1.3 km/Ma since ca. 1.2 Ma during initiation of the San Jacinto fault zone. Second, I present a new data set of cosmogenic radionuclide-derived burial ages and paleodenudation rates ($^{26}Al/^{10}Be$) from the Pleasant Canyon complex in the Panamint Range, and show that denudation rate and sediment flux have varied by a factor of ~2x since the middle Pleistocene. I conclude high frequency variability is driven by climate change, and not tectonic perturbations, as supported by published constraints for exhumation timing. The middle Pleistocene transition from 40–100 ka periodicity may drive the observed changes, a tentative conclusion that makes testable predictions for stratigraphic records of past climate in other locations. Empirical evidence for climate-modulated erosion and sediment flux provides valuable constraints for numerical models of landscape evolution and sedimentary basin architecture.

Tectonic Exhumation and Climate Driven Erosion in Extensional Mountain Blocks: Two Examples from California, USA

Cody Curtis Mason

GENERAL AUDIENCE ABSTRACT

Vertical motions along faults produce uplift of mountain blocks, often with steep high topography, which is accompanied by subsidence of adjacent sedimentary basins. Understanding cycles of fault initiation, uplift, and eventual degradation of mountainous fault blocks through erosion is a fundamental goal of the geoscience community, as is inversion of records of past environmental conditions preserved in sedimentary basins. The Pacific-North America plate boundary in California, USA, is composed of several major fault systems that provide an opportunity to study vertical uplift and erosion of mountains, and the sedimentary basins that preserve records of changes in erosion rates through time. In this context, I present a dissertation composed of two original research articles. In Chapter Two, I use thermochronometry in the Santa Rosa Mountains, Coachella Valley, to constrain initiation timing and vertical uplift rates for an extensional fault system called the west Salton detachment fault (WSDF). Localization of the plate boundary in Coachella Valley led to initiation of the WSDF and the southern San Andreas fault system at ca. 8 Myr ago, timing which may reflect a global plate-tectonic driver. Vertical uplift of the Santa Rosa Mountains via the WSDF was moderate during the time between ca. 8–1.2 Myr, then vertical uplift increased four-fold during the initiation of a new strike-slip fault within the southern San Andreas system. In Chapter Two, I use rare isotopes called cosmogenic radionuclides in sediment from basin stratigraphy to constrain the magnitude and variability of erosion in the Pleasant Canyon catchment of the Panamint Mountains since ca. 1.5 Myr ago. The mean erosion rate for Pleasant Canyon is 36 ± 8 mm/kyr, and individual samples vary by up to 2x, indicating erosion rates were not constant through time. The timescales of variability, and evidence from basin stratigraphy suggest that glacial-interglacial climate change produced the observed changes in erosion in this mountain block. This conclusion makes testable predictions for other unglaciated catchments in extensional fault blocks, while evidence of climate-induced changes in sediment fluxes from mountains to basins has potential implications to recovering information about past climate change from stratigraphy.

ACKNOWLEDGEMENTS

I thank the committee and my academic advisors Dr. Brian W. Romans and Dr. James A. Spotila for this opportunity, for their guidance with research and writing, and for their advice and assistance negotiating various aspects of school-work-life. Brian, has been particularly patient and nurturing, and an all-around great advocate. Thanks also to Bill Craddock for assistance with cosmogenic workflows used in Chapter Three.

Next, and most importantly, I wish to acknowledge my wife and best friend Sarah, who provided much needed support and encouragement at every step during the last five, no, the last ten years(!) of schooling and during my insipient career as a geoscientist. This achievement would not have been possible without her unfailing encouragement. She has been a terrific ally, fierce advocate, and loving mother to our young and beautiful child, Siena, who we joyously welcomed to the world while living in Virginia. I love you both, Sarah and Siena. Thank you for all the love and support these years.

I wish to acknowledge my parents; my mother Christine Curtis, and father Randy Mason, for helping to guide me to this point in life. Their thoughtful and judicious advice saw me through numerous goals including staring a new career and a family of my own.

In the spring of 1980, when I was just four weeks old, my mother and father placed me in a cardboard box inside their VW van, and sped away from Arizona straight toward the Canadian Rockies and the recent eruption of Mt. St. Helens. We famously toured through our nation's National Parks on a shoe-string, and infamously rented *the last* room in a Yellowstone lodge during a serious blizzard. I thank my father for taking me on hikes, and giving me my first rock hammer, then promptly taking it away, only to re-gift it some 20 years later. All this must have contributed to a desire to carry 80 lbs. of rocks on my back, down a mountainside, in the middle of nowhere. Thank you for those experiences. I love you both.

I thank my grandmother Charlotte for helping my family through many years of school with little income. Her charity and understanding were legendary, and I hope to honor her memory by living a long, happy, fulfilling life, as she did.

Thanks to Michelle Fame and Josh Valentino for training, tutoring, and at times spoon feeding me various tectonic and geomorphic workflows. Thanks to Neal Auchter and Teddy Them for keeping me from killing myself or losing my mind in the field.

Thanks to Andrea Fildani for mentoring me during two summers in Austin Texas, and for expanding my horizons. My experiences in the Statoil Austin office were invaluable and I look forward to collaborating on future project.

I must acknowledge the good folks with whom I've shared an office over the last five years; our hijinks of indoor baseball, hacky sack, and *occasional* lunch beers made this time more fun than it might have been. Cheers!

I suppose I could thank our old cat and dog, Brian and London, for companionship during late nights writing this dissertation and the chapters within. But then I might go on thanking every beverage and pizza I ever consumed at the Pub or the Cellar. Nah.

Finally, thanks to ol' Ballarat Rocky for helping to save a valuable field notebook from the clutches of jeep-driving tourists.

FINANCIAL SUPPORT

Financial support for Chapter Two was provided by National Science Foundation grant EAR-1145115 (Spotila), and EAR-0125307, EAR-0337775 and EAR-0809638 (Axen), and EAR-1144946 (Dorsey).
Financial support for Chapter Three was provided by an American Chemical Society-Petroleum Research Fund-Doctoral New Investigator grant (#53553-DNI8) to BWR with additional analytical support from a seed grant from PRIME (Purdue Rare Isotope Measurement Laboratory) to CM and BWR.
CM was awarded a Virginia Tech College of Science-Graduate Student Doctoral Award that supported a research assistantship, and financial support was provided to CM in the form of a graduate research grant from the Department of Geoscience.

ATTRIBUTIONS

Chapter Two has been submitted to Tectonics and is currently under review. The co-authors are James A. Spotila, Gary Axen, Rebecca J. Dorsey, Amy Luther, and Daniel F. Stockli. I collected and processed samples, conducted analyses, interpreted data, conducted thermal modeling, and wrote the manuscript. JAS assisted in sample analyses and manuscript editing, and GA and RJD contributed to manuscript editing to a lesser extent. GA, AL, and DFS collaborated by supplying unpublished sample data.
Citation:
Mason, C. C., Spotila, J. A., Axen, G., Dorsey, R. J., Luther, A., and Stockli, D. F., (in review; Tectonics), Two-phase exhumation of the Santa Rosa Mountains: low- and high-angle normal faulting during initiation and evolution of the southern San Andreas fault system.

Chapter Three is in preparation for submission to Earth and Planetary Science Letters. I conducted field work, sample preparation, and data analyses, and wrote the manuscript. Co-author BWR participated in field work, and assisted in manuscript editing.
Citation:
Mason, C.C., and Romans, B.W., (in prep.), Climate-driven unsteady denudation and sediment flux in a high-relief unglaciated catchment-fan system using ^{26}Al and ^{10}Be: Panamint Valley, California.

TABLE OF CONTENTS

Academic Abstract…..…….ii

General Audience Abstract…..……...iii

Acknowledgements…….iv

Financial Support...……..v

Attributions…….....v

Table of Contents……vi

List of Tables……..…….x

List of Figures…….xi

List of Appendices……xiii

CHAPTER ONE

Introduction……..…….....1

Summary of Chapters Two and Three…….5

References……8

CHAPTER TWO

Two-phase exhumation of the Santa Rosa Mountains: low- and high-angle normal faulting during initiation and evolution of the southern San Andreas fault system……..…….....11

Index Words and Highlights.……..….....11

Abstract …….……..….....12

Introduction……....13

Background……16

Regional Tectonic Setting……..16

West Salton Detachment Fault……...19

Central Salton Block and the Santa Rosa Mountains……21

Methods…….....23

AHe Thermochronometry……..23

Thermal History Modelling……...26

Results……26

Apatite U-Th/He Thermochronometry……..27

Post-WSDF tilt corrections……32

Thermal History Modeling……..……..36

Discussion……..39

8-Ma onset of exhumation of the WSDF footwall……..……..39

Rates and Magnitudes of Exhumation……...41

Implications……45

Conclusions……49

Acknowledgements…….…...51

References…….....51

Appendix 2.1 Supporting Information (Table S1: A-He Data) …….....68

CHAPTER THREE:

Climate-driven unsteady sediment flux and denudation in a high relief unglaciated catchment-fan system using ^{26}Al and ^{10}Be: Panamint valley, California….....73

Keywords and Highlights……..73

Abstract…….....74

Introduction……75

Background……80

Pleasant Canyon Complex source-to-sink parameters ……..80

Late Cenozoic Tectonic History……82

Pleistocene Climate History……...85

Previous Regional Paleodenudation Studies……..86

Methods……..87

Sedimentary Lithofacies & Stratigraphic Architecture……..87

Field Sampling, Laboratory Preparation, and Measurement of cosmogenic $^{26}Al/^{10}Be$…….87

Sediment Provenance…….89

Cosmogenic $^{26}Al/^{10}Be$ Burial Dating and Paleodenudation Calculations……89

Assumptions Associated with Burial Age and Paleodenudation Rate Calculations……92

Mass Fluxes and Catchment Morphometrics…….93

Results……94

Depositional Lithofacies and Stratigraphic Architecture of the PCC……94

Alluvial Lithofacies Association……95

Transitional Lithofacies Association…….96

Lacustrine Lithofacies Association……97

Stratigraphic Architecture and Correlation……99

Depositional Evolution of the PCC……..100

CRN-derived Stratigraphic Ages and Paleodenudation Rates…….102

Volumetric-based Mass Flux Estimates……...107

Discussion……108

Climate-driven Variability in Catchment-fan System Response…….108

Implications for Pleistocene Tectonics of Panamint Valley……111

Implications to Stratigraphic Concepts……113

Conclusions……..115

Acknowledgements……..116

References……116

Appendix 3.1: Supplementary Figures…….....128

LIST OF TABLES

CHAPTER TWO

Table 2.1: Apatite helium (AHe) data……68

CHAPTER THREE

Table 3.1 AMS results, ^{26}Al and ^{10}Be burial ages and denudation rates for samples from the Pleasant Canyon Complex and modern catchment outlets, Panamint Range and Valley, USA…… 103

LIST OF FIGURES

CHAPTER ONE

Figure 1.1: Strain rate tensor model map for California, western Nevada, and northwest Mexico…….3

Figure 1.2: Schematic of sediment supply (Qs) signal propagation through a sediment routing system……..5

CHAPTER TWO

Figure 2.1: Simplified tectonic map, and shaded relief of topography and bathymetry of southern California and northwest Mexico……17

Figure 2.2: Shaded relief map and major faults of the Coachella Valley and western Salton Trough, California……..28

Figure 2.3: Detailed geologic map of the Santa Rosa Mountains with apatite U-Th/He (AHe) sample locations and ages, as well as topographic profiles.……...30

Figure 2.4: Topographic profiles across the southern and central Santa Rosa Mountains with sample locations and apatite U-Th/He (AHe) cooling ages in millions of years…..31

Figure 3.5: Elevation-age plots for samples of apatite U-Th/He from the Santa Rosa Mountains. A: samples form the eastern Santa Rosa Mountains (SRM) along the footwall of the west Salton detachment fault (WSDF)……33

Figure 3.6: QTQt thermal history model results for apatite U-Th/He (AHe) samples from the Santa Rosa Mountains……..37

Figure 3.7: Paleo elevation-age relationships for samples from the Santa Rosa Mountains (SRM) with structural block diagrams for each relevant time step……...47

CHAPTER THREE

Figure 3.1: Modeled changes in sediment flux (q_s per unit width) and associated timescales resulting from perturbations in tectonic and climatic boundary conditions in a catchment-fan system bound by a range-front normal fault …….....……....78

Figure 3.2: Study area shaded relief map and photopanorama of the Pleasant Canyon Complex (PCC)……..81

Figure 3.3: Pleasant Canyon catchment metrics……83

Figure 3.4: Lithofacies of the Pleasant Canyon complex……..98

Figure 3.5: Photomosaics and large scale facies associations and stratigraphic architecture of the Pleasant Canyon Complex…….101

Figure 3.6: Lithostratigraphy and cosmogenic radionuclide (CRN) sample location within the Pleasant Canyon complex……..104

Figure 3.7: Plot of cosmogenic radionuclide-derived denudation rate vs. composite stratigraphic depth……106

Figure 3.8: Pleistocene paleoclimate, Pleasant Canyon complex (PCC) stratigraphic framework, and paleodenudation rates for the PCC since ca. 1.5 Ma…….....109

Supplementary Figure S3.1: Clasts of augen gneiss (World Beater complex) unique to the Pleasant Canyon catchment……..129

Supplementary Figure S3.2: Syndepositional normal faulting in north wall of Middle Park Canyon……..130

LIST OF APPENDICES

Appendix 2.1 Supporting Information (Table S1: A-He Data) …….....67

Appendix 3.1 Supplementary Figures……..129

CHAPTER ONE

Introduction

Vertical motions of Earth's crust are common along strike-slip or transform fault zones (Mann, 2007), and lead to formation of topographic relief and subsidence of adjacent sedimentary basins (Allen and Allen, 2013). At timescales of $10^{6\text{-}7}$ yrs, multiple lines of evidence support a climatic control on catchment- to orogen-scale denudation rates, morphology, and sediment delivery to basins (Whipple, 2009). In the Andes, hemispheric-scale climate circulation patterns influence orogenic wedge dynamics via latitude dependent rates of mass removal and concomitant isostatic responses (Montgomery et al., 2001). In an elegant demonstration of climatic controls on orogenic processes, Willet (1999) showed that simply changing the direction of wind (direction of moisture flux) to a subduction related orogen greatly affects spatial patterns of exhumation, orogen width, and orogenic wedge symmetry. And paradoxically, tectonics may in turn influence long-term regional to global climate patterns via inception of monsoons in response to high topography, or perturbations to the global carbon cycle by increased weathering of silicate rocks, and burial or oxidation of geological sources of organic carbon during erosion of mountains (Molnar and England, 1990; Hilton et al., 2011). With inevitable global climate change driven by increased carbon emissions, the societal relevance of research on climate-surface process-tectonics dynamics should be apparent.

Stratigraphic patterns of basin fill record the rate and tempo of tectonic and climatic boundary conditions affecting sediment source areas, but inversion of these patterns from stratigraphy can be problematic (Jerolmack and Paola, 2010; Romans et al., 2016). Its widely agreed that in transtensional tectonic settings prone to the formation of endoreic basins, regional climate controls aspects of sedimentary basin fill architecture (Dong et al., 2011). Furthermore,

episodic flooding of rift basins may load faults and trigger ruptures, highlighting effects of climate on tectonics, basin accommodation, and stratigraphy at multiple timescales (Brothers et al., 2011). However, the extent to which climate change influences sediment fluxes from mountain catchments to endoreic basins over Milankovitch timescales is disputed, and though conceptual and numerical models agree that changes in precipitation and temperature modulate weathering and sediment transport (Allen and Densmore, 2000), empirical evidence for a Milankovitch-timescale climate forcing on denudation rates and sediment fluxes is conflicting in many cases (Charreau et al., 2011; Davis et al., 2012; Hidy et al., 2014; Puchol et al., 2016; Oskin et al., in press).

The active transform boundary between the Pacific and North America plates in central and southern California represents a premier natural laboratory to study processes of oblique rifting, the kinematics of transform or strike-slip deformation, as well as surface process response to tectonic and climatic forcings on mountainous source-to-sink sedimentary systems. This region hosts major population centers built upon active faults and geologically unstable substrates, underscoring the societal relevance of research concerning relationships between earthquakes, rock uplift, and sediment transport events (*e.g.* landslides & debris flows) in tectonically active regions. Yet despite generations of geologic research, fundamental questions persist regarding the kinematic evolution of the plate boundary. Specifically, initiation of the southern San Andreas fault system, a major tectonic feature of southern California, which is thought to be between ca. 10 – 5 Ma old (Powell and Weldon, 1992, and references therein). This location allows investigation of cycles of tectonic uplift and subsequent erosion, and specifically the role of changing climate on fluxes of mass from source to sink. Constraints to

climate-driven fluxes of sediment are important components to models of short- and long-term basin dynamics.

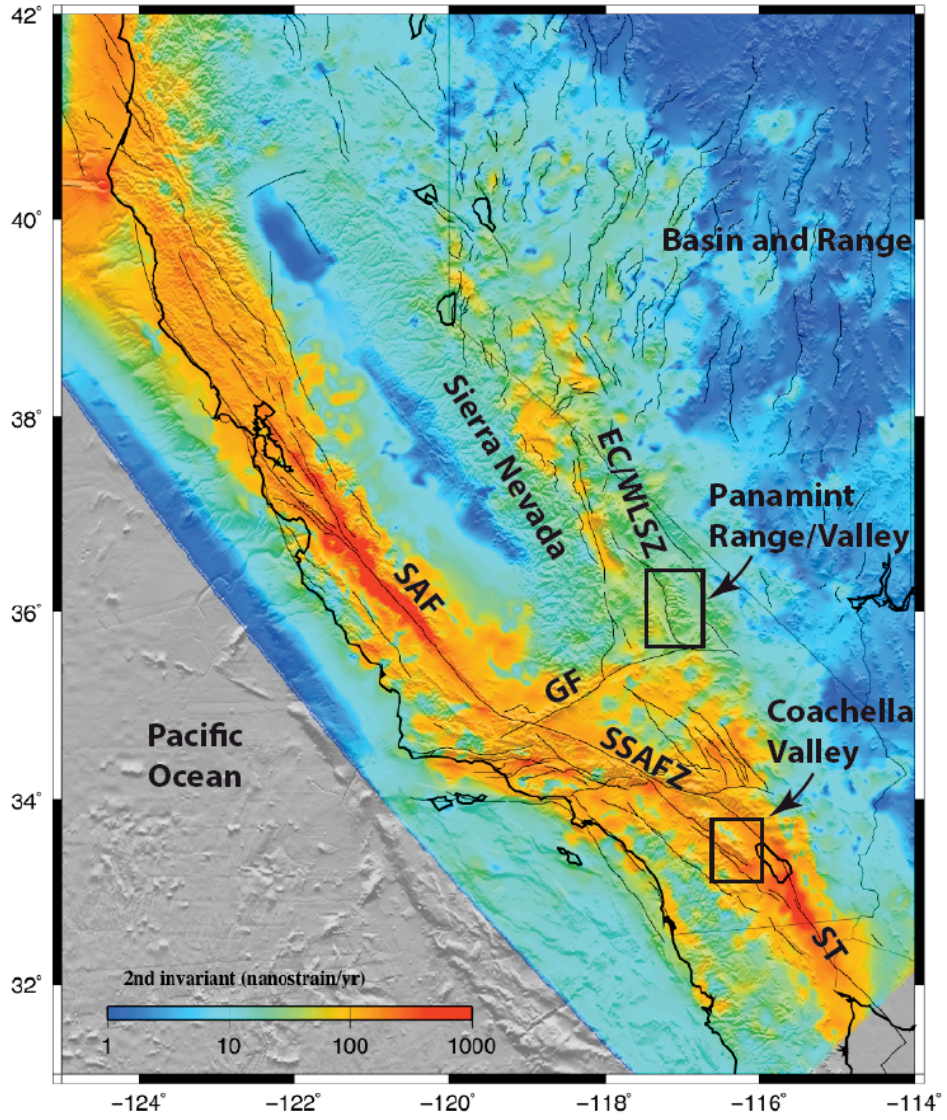

Figure 1.1: Strain rate tensor model map for California, western Nevada, and northwest Mexico. Boxes delineate study areas; Coachella Valley is the focus of Chapter Two, and Panamint Range/Valley is the focus of Chapter Three. EC/WLSZ = eastern California/Walker Lane shear zone, GF = Garlock fault, SAF = San Andreas fault, SSAFZ = southern San Andreas fault zone, ST = Salton Trough. Figure modified from Sandwell (2010).

Clarification of the role climate plays in landscape evolution has global implications to any high-relief, unglaciated sedimentary systems. Figure 1.1 displays a strain rate map for California, which highlights zones of active deformation associated with the Pacific North America plate boundary, and locations of the study areas discussed in this dissertation.

A major goal of the geoscience community is inversion of past climate and tectonics from the sedimentary record. However, quantifying a process, let alone a rate, from form, inevitably leads to problems of non-uniqueness. Determining the relative influence of accommodation vs. supply on stratigraphic patterns is a classic example of a conceptual framework widely used to infer geologic history from incomplete stratigraphic records (Barrell, 1917; Wheeler, 1958). A recent conceptual advancement in sedimentary geology and geomorphology is the idea of environmental signal propagation and preservation (reviewed by Romans et al., 2016). In this framework, signals are changes in sediment production, transport, or deposition that originate from perturbations in up-system boundary conditions (tectonics, climate, anthropogenic activities). Signal propagation has two end-member scenarios: a signal may propagate rapidly through the sediment routing system and become recorded in stratigraphy, or a signal may be 'buffered', delayed, or shredded by effects of sediment storage, remobilization, and autogenic system dynamics, ultimately resulting in additional degrees of freedom in the problem of stratigraphic non-uniqueness. This concept is illustrated in Figure 1.2, and highlights the utility of investigating signal propagation in simplified catchment-fan systems (Figure 1.2 C, D).

Tectonic exhumation and climate-driven erosion are aspects of a continuum of dynamic processes and feedbacks that operate to create and destroy relief. For the purposes of this dissertation, these themes are connected by threads of common geography and tectonic setting along the Pacific-North America plate boundary. However, some aspects of the results of

Chapter Two may be applicable to any strike-slip fault zone, while the results of Chapter Three may be applicable to collisional orogens, or tectonically quiescent settings where climate change may modulate surface process rates. Below I introduce Chapters Two and Three and give an overview of the findings.

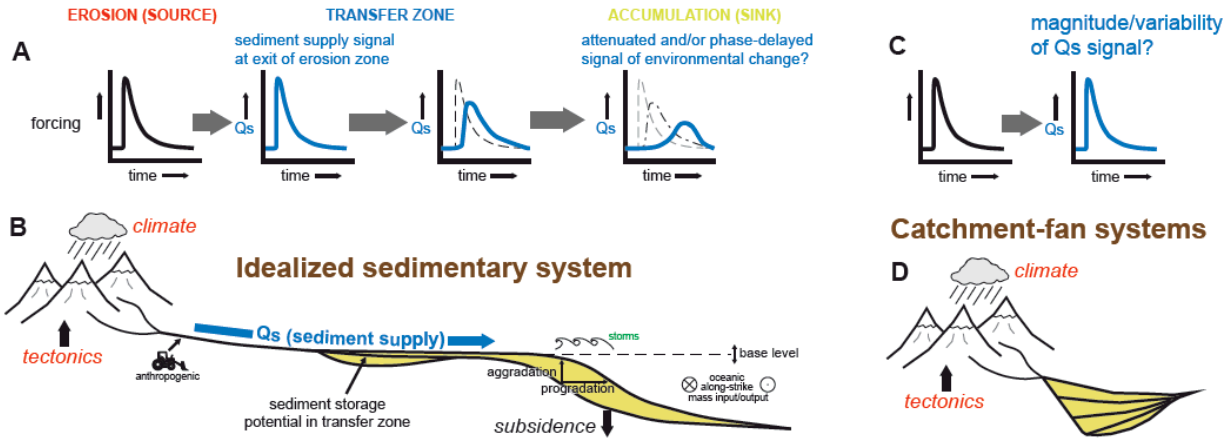

Figure 1.2: Schematic of sediment supply (Qs) signal propagation through a sediment routing system. **A, B**: Qs signal is emitted from the erosion zone and subsequently modulated by sediment storage and recycling in the fluvial transfer zone. **C, D**: Simplified sedimentary system with no transfer zone, used in Chapter Three to test magnitude and variability of signal. Figure modified from Romans et al. (2016).

Summary of Chapters Two and Three

In this dissertation, I present the results of two different research projects; (1) the evolution of the Pacific North American plate boundary in Coachella Valley, specifically the timing and kinematics for initiation of the southern San Andreas system, and (2) constraints on post-exhumation climate-driven erosion and sediment deposition rates within a single catchment-fan system in the Panamint Range, an extensional mountain block in eastern California.

Chapter Two focuses on the late Cenozoic tectonic history of the southern San Andreas fault system in the northern Salton Trough, the onshore expression of the Gulf of California rift system. I provide new constraints on the kinematics of tectonic exhumation of the Santa Rosa Mountains via extension along the west Salton detachment fault (WSDF), in Coachella Valley. The WSDF was kinematically linked to, and temporally coeval with localization of the plate boundary and formation of the San Andreas fault in Coachella Valley (Dorsey et al., 2011), thus the chronology for this tectonic element constrains inception of the southern San Andreas system. This work is underpinned by a new data set composed of low-temperature apatite U-Th-Sm/He thermochronology (AHe) from the Coachella Valley area, and thermal history modeling of those samples using a program called QTQt. I find that AHe samples began to cool, and thus the Santa Rosa Mountains began to exhume along a major extensional system called the west Salton detachment at ca. 8 Ma, and that the rate of exhumation was moderate, or ~0.15 – 0.36 km/Ma between ca. 8 – 1.2 Ma. At ca. 1.2 Ma the west Salton detachment was deactivated during initiation of a new strike-slip fault called the San Jacinto fault, and the vertical exhumation rate for the Santa Rosa Mountains increased three-fold to 1.3 km/Ma. This pulse of rapid uplift was associated with crustal tilting of the Santa Rosa block, on the order of 8 – 12 º northeast.

Chapter Two, titled "Two-phase exhumation of the Santa Rosa Mountains: low- and high-angle normal faulting during initiation and evolution of the southern San Andreas fault system" was submitted for publication to the Journal *Tectonics*, and is currently under review. The co-authors of Chapter Two are: James A. Spotila, Gary Axen, Rebecca J. Dorsey, Amy Luther, and Daniel F. Stockli.

During and after tectonic exhumation of a normal fault block, denudation modifies the morphology of drainage basins. Denudation, the sum of physical and chemical weathering, is accomplished via soil formation, hillslope sediment transport, mass wasting, fluvial incision, and sediment transport through fluvial networks that redistribute material from mountains to receiving basins. The second theme of this dissertation concerns the magnitude and variability in rates of denudation and sediment flux at ca. 10^{4-5} yr timescales from a single catchment in an uplifted normal-fault block. Chapter Three is underpinned by a new data set of cosmogenic radionuclide-derived paleodenudation rates collected from exhumed alluvial strata that was once a linked catchment-fan system in the Panamint Range and Valley. The use of a catchment-fan system greatly diminishes the uncertainty associated with sediment storage and remobilization in large fluvial systems. $^{26}Al/^{10}Be$ burial ages and stratigraphic characterization show that the succession, termed the Pleasant Canyon complex, was aggrading in a mixed alluvial fan-lacustrine environment as early as 1.5 Ma ago, and was abandoned after ca. 0.3 Ma. The mean and standard error of all paleodenudation rate (n=14) is 36 ± 8 mm/kyr (1 σ), the lowest rate is 24 ± .5 mm/kyr, and the highest rates range from 54 – 49 mm/kyr. High frequency fluctuations and a lack of monotonic trend support a Milankovitch climate forcing for rate changes on the order of 1.5 – 2x. Rates appear to fluctuate after ca. 0.6 Ma, and paleodenudation rate data across the Plio-Pleistocene transition (ca. 4 – 1 Ma) in the Fish Creek-Vallecito basin have an identical mean rate (ca. 38 ± 24 mm/kyr; 2 σ) lack temporal variability (Oskin et al., in press), and may indicate that a transition from 40 ky to 100 kyr climate periodicity is necessary to perturb denudation/sediment flux rates in semi-arid high relief, unglaciated catchments.

Chapter Three, titled "Climate-driven unsteady denudation and sediment flux in a high-relief unglaciated catchment-fan system using ^{26}Al and ^{10}Be: Panamint Valley, California" is in

preparation for submission to Earth and Planetary Science Letters, and Brian W. Romans is the sole co-author.

References

Allen, PJ., and Allen, J.R., 2013. Basin Analysis: Principles and Application to Petroleum Play Assessment, 3rd Edition. Wiley-Blackwell, 632 p.

Allen, P.A., Densmore, A.L., 2000. Sediment flux from an uplifting fault block. Basin Res. 12, 367–380. doi:10.1046/j.1365-2117.2000.00135.x

Barrell, J., 1917. Rhythms and the measurements of geologic time. Geol. Soc. Am. Bull. 28, 745–904.

Brothers, D., Kilb, D., Luttrell, K., Driscoll, N., Kent, G., 2011. Loading of the San Andreas fault by flood-induced rupture of faults beneath the Salton Sea. Nat. Geosci. 4, 486–492. doi:10.1038/ngeo1184

Charreau, J., Blard, P.-H., Puchol, N., Avouac, J.-P., Lallier-Vergès, E., Bourlès, D., Braucher, R., Gallaud, A., Finkel, R., Jolivet, M., Chen, Y., Roy, P., 2011. Paleo-erosion rates in Central Asia since 9 Ma: A transient increase at the onset of Quaternary glaciations? Earth Planet. Sci. Lett. 304, 85–92. doi:10.1016/j.epsl.2011.01.018

Davis, M., Matmon, A., Rood, D.H., Avnaim-Katav, S., 2012. Constant cosmogenic nuclide concentrations in sand supplied from the Nile River over the past 2.5 m.y. Geology 40, 359–362. doi:10.1130/G32574.1

Dong, W., Lin, C., Eriksson, K.A., Zhou, X., Liu, J., Teng, Y., 2011. Depositional systems and sequence architecture of the Oligocene Dongying Formation, Liaozhong depression, Bohai Bay Basin, Northeast China. Am. Assoc. Pet. Geol. Bull. 95, 1475–1493.

doi:10.1306/01281110074

Dorsey, R.J., Housen, B.A., Janecke, S.U., Fanning, C.M., Spears, A.L.F., 2011. Stratigraphic record of basin development within the San Andreas fault system: Late Cenozoic Fish Creek-Vallecito basin, Southern California. Bull. Geol. Soc. Am. 123, 771–793. doi:10.1130/B30168.1

Gulick, S.P.S., Jaeger, J.M., Mix, A.C., Asahi, H., Bahlburg, H., Belanger, C.L., Berbel, G.B.B., Childress, L., Cowan, E., Drab, L., Forwick, M., Fukumura, A., Ge, S., Gupta, S., Kioka, A., Konno, S., LeVay, L.J., März, C., Matsuzaki, K.M., McClymont, E.L., Moy, C., Müller, J., Nakamura, A., Ojima, T., Ribeiro, F.R., Ridgway, K.D., Romero, O.E., Slagle, A.L., Stoner, J.S., St-Onge, G., Suto, I., Walczak, M.D., Worthington, L.L., Bailey, I., Enkelmann, E., Reece, R., Swartz, J.M., 2015. Mid-Pleistocene climate transition drives net mass loss from rapidly uplifting St. Elias Mountains, Alaska. Proc. Natl. Acad. Sci.112 (49), 1–6. doi:10.1073/pnas.1512549112

Hidy, A.J., Gosse, J.C., Blum, M.D., Gibling, M.R., 2014. Glacial–interglacial variation in denudation rates from interior Texas, USA, established with cosmogenic nuclides. Earth Planet. Sci. Lett. 390, 209–221. doi:10.1016/j.epsl.2014.01.011

Hilton, R.G., Galy, A., Hovius, N., Horng, M.J., Chen, H., 2011. Efficient transport of fossil organic carbon to the ocean by steep mountain rivers: An orogenic carbon sequestration mechanism. Geology 39, 71–74. doi:10.1130/G31352.1

Jerolmack, D.J., Paola, C., 2010. Shredding of environmental signals by sediment transport. Geophys. Res. Lett. 37, 1–5. doi:10.1029/2010GL044638

Mann, P., 2007. Global catalogue, classification and tectonic origins of restraining-and releasing bends on active and ancient strike-slip fault systems. Geol. Soc. London Spec. Publ. 290,

13–142. doi:10.1144/SP290.2

Molnar, P., England, P., 1990. Late Cenozoic uplift of mountain ranges and global climate change: chicken or egg? Nature 346, 29–34. doi:10.1038/346029a0

Montgomery, D.R., Balco, G., Willett, S.D., 2001. Climate tectonic and the morphology of the Andes. Geology 29, 579–582. doi:10.1130/0091-7613(2001)029<0579:CTATMO>2.0.CO;2

Oskin, M.E., Longinotti, N.E., Peryam, T., Dorsey, B., Deboer, C., in press, Steady ^{10}Be-derived paleo-erosion rates across the Plio-Pleistocene climate transition, Fish Creek-Vallecito basin , California. J. Geophisical Res.

Powell, R.E., and Weldon, R.J., II, 1992, Evolution of the San Andreas fault: Annual Review of Earth and Planetary Sciences, 20, p. 431–468, doi:10.1146/annurev.ea.20.050192.002243.

Puchol, N., Charreau, J., Blard, P., Lavé, J., Dominguez, S., Pik, R., Saint-carlier, D., ASTER Team, 2016. Limited impact of Quaternary glaciations on denudation rates in central Asia. Geol. Soc. Am. Bull. 129, 1–21. doi:10.1130/B31475.1

Romans, B.W., Castelltort, S., Covault, J.A., Fildani, A., Walsh, J.P., 2016. Environmental signal propagation in sedimentary systems across timescales. Earth-Science Rev. 153, 7–29. doi:10.1016/j.earscirev.2015.07.012

Sandwell, D.T., 2010. Comparison of strain rate maps, UNAVCO.

Wheeler, H.E., 1958. Time-stratigraphy. Am. Assoc. Pet. Geol. Bull. 42, 1047–1063.

Whipple, K.X., 2009. The influence of climate on the tectonic evolution of mountain belts. Nat. Geosci. 2, 730–730. doi:10.1038/ngeo638

Willett, S.D., 1999. Orogeny and orography: The effects of erosion on the structure of mountain belts. J. Geophys. Res. 104, 28957. doi:10.1029/1999JB900248

CHAPTER TWO

Two-phase exhumation of the Santa Rosa Mountains: low- and high-angle normal faulting during initiation and evolution of the southern San Andreas fault system

Cody C. Mason[1], James A. Spotila[1], Gary Axen[2], Rebecca J. Dorsey[3], Amy Luther[4], and Daniel F. Stockli[5]

[1]Department of Geosciences, Virginia Polytechnic Institute and State University, 4044 Derring, Blacksburg, VA, 24061

[2]Department of Earth and Environmental Science, New Mexico Tech, MSEC 344, Socorro, New Mexico, 87801

[3]Department of Earth Sciences, University of Oregon, Eugene Oregon, 97403

[4]Department of Geology and Geophysics, Louisiana State University, 101/101A-B Howe-Russell-Kniffen, Baton Rouge Louisiana, 70803

[5]Department of Geological Sciences, University of Texas at Austin, Austin, Texas, 78712

Index words: Thermochronology (1140), Continental neotectonics (8002, 8107), Kinematics of crustal and mantle deformation (8011), Continental margins; transform (8106), Continental tectonics; extensional (8109)

Key Points:

- West Salton detachment initiated at ca. 8 Ma in Coachella Valley, signaling initiation of the southern San Andreas system

- Ca. 8 Ma plate-boundary localization in Salton trough contrasts progressive localization in the Gulf of California between ca. 12.5-6 Ma
- Local fault geometry, not plate-motion obliquity**,** exerts primary control on rock uplift rates in Santa Rosa Mountains since ca. 1.2 Myr

ABSTRACT

Low-angle detachment fault systems are important elements of active plate boundaries, yet kinematic relationships between detachment faults and inception of transform plate margins are poorly understood. The west Salton detachment fault (WSDF) is a major low-angle normal fault that formed coeval with localization of the Pacific-North America plate boundary in Coachella Valley. Low-temperature thermochronometry (apatite U/Th-He; AHe; n=29 samples) and thermal history modeling of samples from the Santa Rosa Mountains (SRM) reveal that initial exhumation along the WSDF began at ca. 8 Ma, and is responsible for exhumation of the footwall from depths of ~3 – 4 km. The timing of extension initiation suggests that perturbation of relative plate motions at 8 Ma is responsible for initiation of the southern San Andreas system in the Salton Trough, in contrast with evidence for progressive localization of plate boundary strain in the Gulf of California. Detachment-related extension proceeded at moderate rates; vertical exhumation was 0.15 – 0.36 km/Ma, with maximum fault slip rates of ~1.2 – 3.0 km/Ma. An uplifted fossil helium partial retention zone is present in the eastern SRM, while a deeper crustal section has been exhumed along the Pleistocene high-angle Santa Rosa fault (SFR) in the southwest SRM. AHe isochrons across the SRM indicate post-WSDF vertical exhumation along the SRF was ~1.3 km/Ma. Pleistocene regional tectonic reorganization was contemporaneous

with an abrupt transition from low- to high-angle faulting and indicates local fault geometry may at times exert a fundamental control on rock uplift rates along strike-slip-fault systems.

2.1.0 INTRODUCTION

Extensional kinematics of transform related basins may be complex, with phases of extension along both high-and low-angle structures. Low-angle normal faults (dip <30°) are a globally important feature in extensional continental tectonics [*Wernicke*, 1985; *Axen*, 1999; *Burchfiel et al*., 1992], yet may play an underappreciated role in the evolution of transform plate boundaries. Systems composed of semi-parallel low-angle normal faults and strike-slip faults occur in several localities along the Pacific-North America plate boundary [*Roeske et al*., 2007]. The northern Salton Trough in southern California hosts the late Miocene southern San Andreas fault (SAF) system, which includes the inactive West Salton Detachment fault (WSDF) and the semi-parallel active Coachella strand of the SAF. The WSDF and southern SAF in Coachella Valley are coeval structures [*Axen and Fletcher*, 1998; *Dorsey et al*., 2011], thus the kinematics of extension along the WSDF should inform us about the timing of plate boundary localization in the Salton Trough and the nature of the driving mechanisms.

The kinematics of plate boundary evolution within the Salton Trough—the northern extent of the Gulf of California—are debated, and several models have been proposed for the kinematic evolution of the Gulf of California [summarized by *Darin et al*, 2016]: 1) a model of strain partitioning between ca. 12.5 – 6 Ma with orthogonal extension in the proto-Gulf and transform style deformation within the Continental Borderlands, followed by transform plate boundary localization in the Gulf of California post ca. 6 Ma, 2) a distributed transtension model, where oblique rifting occurred between ca. 12.5 – 6 Ma, followed by strong dextral shear during

plate boundary localization at ca. 6 Ma, and 3) a model of progressive localization, with weak extension and minor dextral transtension between ca. 12.5 – 8 Ma, followed by strong oblique extension and plate boundary localization at ca. 8 – 6 Ma [*Stock and Hodges*, 1989; *Fletcher et al*., 2007; *Seiler et al*., 2011; *Bennett et al*., 2013; *Bennett and Oskin*, 2014]. Onset of major tectonic subsidence associated with plate boundary localization was synchronous along much of western Mexico between ca. 8 – 6 Ma [*Pacheco et al*., 2006; *Dorsey et al*., 2011; *Seiler et al*., 2013; *Bennett et al*., 2016]. The lack of well-documented timing for initiation of the WSDF—the major tectonic element of the western Salton trough—precludes complete assessment of kinematic models for plate boundary localization and evolution in the Salton Trough.

Tectonic deformation in the Salton Trough has been interpreted in the context of plate-boundary dynamics. Cessation of subduction along the plate boundary at ca. 12.5 Ma may have initiated early back arc extension in western Mexico and the Salton Trough. Then at ca. 8 Ma a clockwise rotation of relative Pacific-North America plate motions is associated with localization of dextral plate boundary deformation along the plate boundary south of the Salton Trough, and shortly after regional marine incursion occurred after ca. 6.5 Ma [*Atwater and Stock*, 1998; *Atwater*, 1970; *Crowell*, 1982; *Axen and Fletcher*, 1998; *Oskin et al.*, 2001; *Shirvell et al*., 2009; *Bennett et al*., 2015]. *Shirvell et al*. [2009] suggested that extension and WSDF footwall exhumation started as early as ca. 12 Ma, with rapid exhumation between ca. 7 or 5 – 2 Ma, nearly synchronous with onset of dextral strike-slip deformation along the southern SAF system [*Matti and Morton*, 1993; *Oskin and Stock*, 2003]. *Dorsey et al.* [2011] used stratigraphic evidence to show that syn-tectonic basin subsidence and related faulting initiated in the Salton Trough region at ca. 8 Ma, thus questioning the previous interpretation for an earlier initiation age for the WSDF. These two studies suggest very different tectonic models for the evolution of

the southern SAF system, and the timing of WSDF initiation should help constrain this major tectonic event.

The kinematics of strain partitioning along the southern SAF in Coachella Valley have influenced the late Cenozoic kinematics of the Salton Sea crustal block [*Meade and Haggar*, 2005]. Geological, geophysical, and geomorphological evidence reveal recent and active northeast tilt of the central Salton block, potentially driven by transpression and crustal loading along a northeast dipping SAF in Coachella Valley [*Dorsey and Langenheim*, 2015]. Hypotheses regarding the late Cenozoic kinematic history of the central Salton block cannot be fully assessed, however, due to the lack of strain markers in the WSDF footwall in the Santa Rosa Mountains (SRM). Uplift and erosion of crustal scale blocks elsewhere along the SAF system have proven to be informative regarding the nature of strain partitioning and evolving kinematic response to plate motion obliquity driving deformation within the plate boundary [*e.g. Spotila et al*., 1998; *Spotila and Sieh*, 2000; *Stockli*, 2005; *Dorsey and Roering*, 2006; *Spotila et al*., 2007]. The exhumation history of the SRM block similarly should be useful for constraining the tectonic evolution of the southern SAF system.

In this study we present new data from 29 new samples of apatite U-Th/He thermochronometry (AHe), in order to elucidate early WSDF behavior and late Cenozoic kinematic history of the SRM and central Salton block. Our data support an interpretation for two phases of normal faulting in the SRM. We document the initiation timing and magnitude of vertical exhumation along the WSDF footwall during the inception of the southern SAF transform system in the northern Salton Trough, and constrain the timing and kinematics of late-stage crustal-scale tilting and exhumation associated with tectonic reorganization of the southern SAF system.

2.2.0 GEOLOGIC BACKGROUND

2.2.1 REGIONAL TECTONIC SETTING

The modern southern SAF system (Fig. 1) has a long history of kinematic complexity and regional fault-system reorganization. Mid to late Miocene dextral plate boundary motion was focused west of Baja along the continental borderlands and along proto-SAF strands northwest of Coachella Valley in the central and western Transverse Ranges [*Spencer and Normark*, 1979; *Powell*, 1981; 1982; *Matti and Morton*, 1993; *Buscher and Spotila*, 2007; *Bennett and Oskin*, 2014]. The modern Gulf of California spreading system transfers slip north to the southern SAF system through right-stepping faults in the southern Coachella Valley. The southern SAF system consists of two major concentrations of dextral deformation; the San Jacinto fault zone (SJFZ) and the Coachella strand of the SAF [*Thatcher et al*., 2016]. The SJFZ is kinematically linked to the Mojave section of the SAF, whereas the Coachella segment of the SAF appears to transfer slip to the Eastern California shear zone [*Thatcher et al*., 2016]. The inactive WSDF lies between the SJFZ and the SAF Coachella strand along the western Salton Trough.

The "Big Bend" along the Mojave segment of the SAF represents an increase in obliquity along strike from several degrees in the Coachella Valley to 20 – 30° through the Mojave segment [*Spotila et al*., 2007]. This region has hosted a complex and protracted evolution of the Pacific-North America plate boundary since before early Miocene time; the East Pacific Rise first impinged on North America between 28 – 26 Ma [*Atwater* 1989; *Dickinson*, 1996].

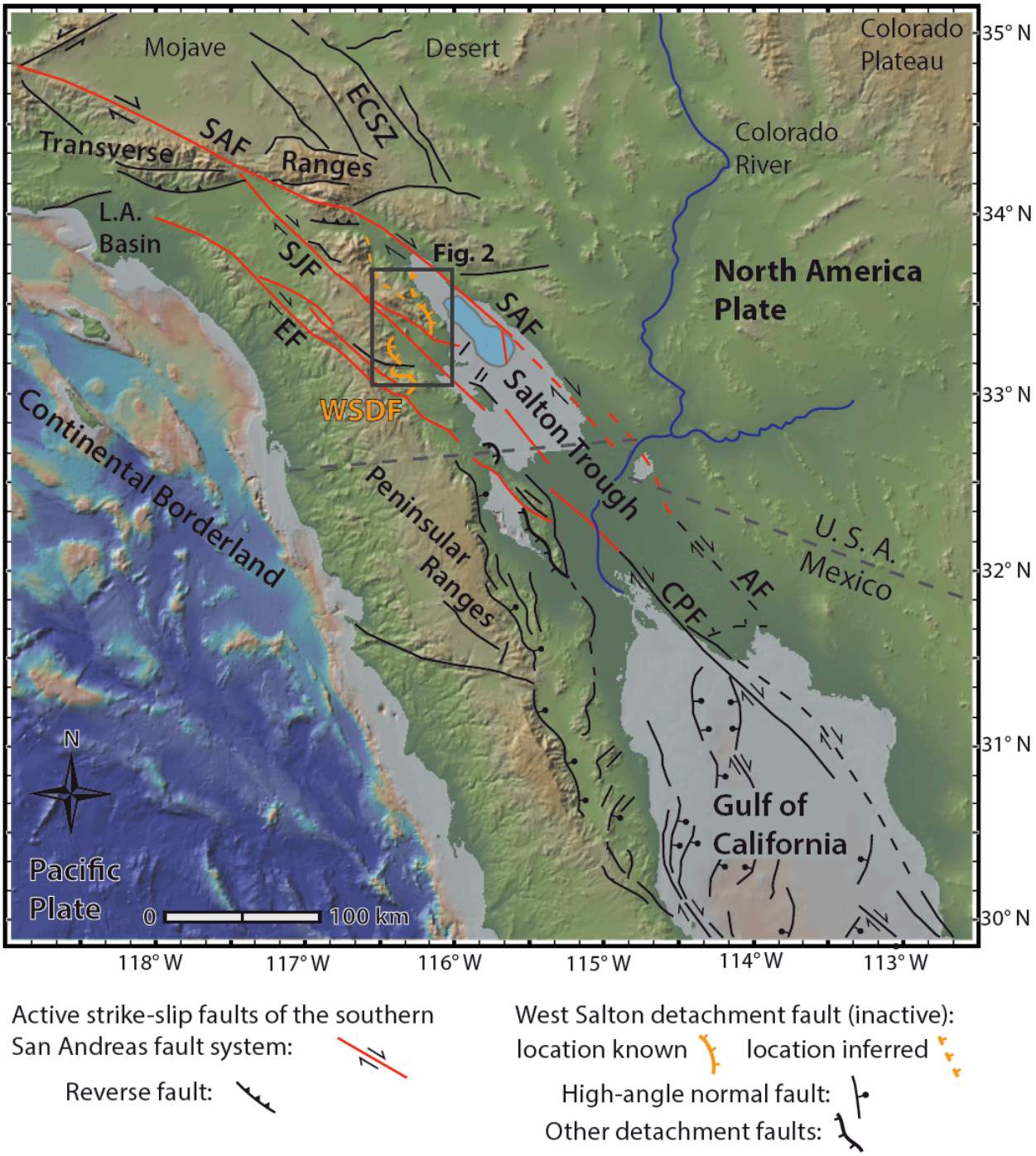

Figure 2.1: Simplified tectonic map, shaded relief of topography and bathymetry of southern California and northwest Mexico. Inset box outlines location of Figure 2. AF = Altar fault, CPF = Cerro Prieto fault, EF = Elsinore fault, L. A. = Los Angeles, SAF San Andreas fault, SJF = San Jacinto fault, WSDF west

Salton detachment fault. Fault locations from Quaternary fault and fold database, and *Dorsey et al*. (2013).

Dextral strike-slip faults in the central Transverse Ranges west of the Mojave Desert are thought to have acted as the main continental transform boundary between ca. 20 – 12 through 6 – 5 Ma [*Powell*, 1981; *Crowell*, 1982; *Ehlig*, 1982; *Matti and Morton*, 1993; *Weldon et al*., 1993]. Early- to mid-Miocene basins west of the Mojave Desert record an evolution from major through-going sediment dispersal systems to localized and segmented systems indicative of tectonic reorganization and localized relief generation during strike-slip offset [*Powell and Weldon*, 1992]. The San Gabriel fault was an active southern SAF strand beginning at ca. 10 Ma through 6 – 5 Ma [*Powell and Weldon*, 1992]. Inversion of Miocene basins at ca. 5 Ma signified the transfer of deformation from the San Gabriel fault to the active Mojave segment of the SAF system [*Crowell*, 1982; *Matti and Morton*, 1993], which now accommodates between ~30% – 70% of plate boundary motion [*Thatcher et al*., 2016, and references therein].

The Salton Trough is the northern continuation of the Gulf Extensional Province and is defined by evolving structural elements of the southern SAF system. The northern terminus of the modern Salton Trough is San Gorgonio Pass, while the east and west are bound by the SAF and WSDF, respectively. San Gorgonio Pass represents a structural knot inhibiting through-going ruptures of the SAF [*Langenheim et al*., 2005]. The SAF system has responded to the structural knot through initiation of the Elsinore and SJF zones at ca. 1.2 Ma [*Langenheim et al*., 2005; *janecke et al*., 2010; *Dorsey et al*., 2012; *Kirby et al*., 2007; *Lutz et al*., 2006; *Steely et al*., 2009]. When combined, the Elsinore – SJF zones reroute 25% – 35% of plate boundary slip budget to the west around San Gorgonio Pass [*Thatcher et al*., 2016]. The Coachella strand of the SAF accommodates between ~30 – 45% of total plate motion [*Behr et al*., 2010], and may

transfer a significant portion of motion (~12% – 36%) east of San Gorgonio Pass to the eastern California shear zone and the Walker Lane [*Thatcher et al*., 2016, and references therein]. Although timing of SAF initiation in Coachella Valley is debated, strike-slip fault displacement in the Salton Trough was ongoing by ca. 6 – 5 Ma along the Coachella Strand [*Crowell*, 1981; *Ehlig*, 1981; *Matti and Morton*, 1993; *Nicholson et al*., 1994; *Ingersoll and Rumelhart*, 1999; *Spencer and Normark*, 1979; *Stock and Hodges*, 1989; *Atwater and Stock*, 1998; *Oskin and Stock*, 2003]. Kinematic understanding of the initiation of early rifting and evolution of the modern SAF system in Coachella Valley is incomplete, however, and requires specific characterization of each stage and element of deformation.

Although timing of plate boundary deformation in the Salton Trough and Gulf of California may overlap, the Miocene tectonic and volcanic history of the Salton Trough differs from that of the northern Gulf of California [*Gastil et al*., 1979; *Herzig and Jacobs*, 1994; *Dorsey et al*., 2011]. First, no pre-WSDF extensional systems are documented in the Salton Trough, except for an isolated Oligo-Miocene basin east of the Salton Trough (*Law et al*., 2001). Second, Oligo-Miocene volcanic activity in the Salton Trough region was sparse, with limited activity between ca. 20 – 13 Ma probably associated with Basin-and-Range style extension, followed by sparse volcanism after ca. 4 Ma to present [*Ruisaard*, 1979; *Herzig and Jacobs*, 1994]. Volcanic activity and extension were closely linked in the Gulf Province [*Gans*, 1997], yet it is not clear if middle to late Miocene volcanism in the Salton Trough region was associated with extensional fault systems.

2.2.2 WEST SALTON DETACHMENT FAULT

The WSDF is the northernmost expression of a belt of northwest-trending extensional structures that stretch over 1000 km from southern Baja to northern Coachella Valley, and is interpreted to post-date low-angle structures of the Basin-and-Range [*Axen and Fletcher*, 1998]. The WSDF has been mapped in at least two east-dipping (~15° – 20°) strands through the central and eastern SRM [*Axen and Fletcher*, 1998; *Matti et al*., 2002]. This low-angle normal fault system was kinematically linked to and co-evolved with dextral faults of the southern SAF system and the Gulf of California since late Miocene time [*Dorsey et al*., 2011; *Bennett and Oskin*, 2014]. The evolution of the WSDF has been interpreted within a framework of regional plate-tectonic changes, including fault initiation during cessation of subduction west of Baja after ca. 12 Ma and a subsequent acceleration of detachment faulting between ca. 7 – 5 Ma, concurrent with an ca. 8 Ma regional plate-tectonic reorganization and migration of the Pacific-North America plate boundary into the Salton Trough [*Shirvell et al*., 2009]. Recent studies in the Gulf of California interpret phases of active extension between ca. 17 – 12.5 Ma, ca. 12.5 – 8 Ma, and then rapid and synchronous basin formation and transform plate boundary localization between 8 – 6 Ma to present [*Bennett et al*., 2013; 2016; *Bot et al*., 2016].

Few studies have constrained the timing and kinematics of the WSDF (Axen and Fletcher, 1998; Shirvell et al., 2009; *Dorsey at al*., 2011]. *Axen and Fletcher* [1998] favored a late Miocene initiation age that may have predated the active southern SAF in Coachella Valley, with slip ongoing through mid-Pleistocene time. *Shirvell et al*., [2009] used low-temperature thermochronometry (Apatite and zircon He) on WSDF footwall- and hanging-wall rocks (~30 km southwest of the SRM) to assess the timing and magnitude of slip along the detachment system. A high relief transect (~1300 m) at Mt. San Ysidro yielded AHe cooling ages that span ca. 14 – 5 Ma (Fig. 2) with no discernable break in slope [*e.g. Stockli*, 2005]. Further south at

Pinyon and Yaqui Ridge, low-elevation lateral transects yield AHe ages that span ca. 5 – 2 Ma, becoming younger in the hanging wall transport direction and indicating rapid Plio-Pleistocene cooling. Their results indicated that: (1) the WSDF was active by late Miocene through Pleistocene time (ca. 7 or 5 – 2 Ma), with rapid, high magnitude exhumation between ca. 5 – 2 Ma, and (2) possible WSDF initiation as early as ca. 14 – 12 Ma. However, stratigraphic analysis in the Fish Creek-Vallecito basin documented the onset of strong extension and fault-bounded basins at 8.1 ± 0.4 Ma [*Dorsey et al.,* 2011], nearly synchronous with the interpreted increase in WSDF slip rate at ca. 7 – 5 Ma. The age of WSDF initiation is still unclear from available data, particularly in the northern Salton Trough where the SRM lack constraints, and exposed footwall rocks in the San Jacinto Mountains yield mid-Miocene and older AHe cooling ages that predate WSDF-related extension [*Wolf et al*., 1997]. If the WSDF initiated close to 12 Ma, the timing would fit with that of regional but weak proto-Gulf extension, but an age of ca. 8 Ma indicates a very different plate-tectonic driver for strain localization in the Salton Trough, likely related to a clockwise rotation in relative Pacific-North America plate velocities at ca. 8 Ma.

2.2.3 CENTRAL SALTON BLOCK AND THE SANTA ROSA MOUNTAINS

The central Salton block consists of the subsiding Coachella Valley and the uplifting SRM, and is composed of relatively intact lithosphere bounded by the SJFZ in the southwest and the Coachella strand of the SAF in the northeast [*Meade and Hagar*, 2005; *Dorsey and Roering*, 2006; *Janecke et al*., 2010; *Dorsey and Langenheim*, 2015]. The central Salton block contains abundant evidence of recent and active northeast tilting, including asymmetric Coachella basin fill, and geomorphology of the SRM [*Dorsey and Langenheim*; 2015]. The southwest flank of the SRM in Clark Valley exhibits faceted spurs and juvenile drainages with low alluvial fan-

catchment area ratios, and has high-gradient slopes relative to the northeast SRM. The northeast flank of the SRM has lower average hillslope gradient, little indication of active faulting on the WSDF, contains relatively well-developed drainages with larger fan-catchment area ratios, and exhibits progressive tilting of several degrees of Pleistocene alluvial horizons relative to modern fans. The Coachella basin also displays asymmetric deepening from southwest to northeast, with growth strata that dip up to ~8° east and thicken and terminate at the SAF below the surface of the Salton Sea [*Fuis et al*., 2012]. This evidence points to broad, down-to-the-northeast tilting of the central Salton block, which could be driven by transpressive loading on the SAF [*Dorsey and Langenheim*, 2015]. The kinematic implications of central Salton block tilting are uncertain, however, because the local orientation of the SAF is not known. Some studies have implied or assumed a vertically dipping SAF [*Meade and Hagar*, 2005; *Smith-Konter and Sandwell*, 2009; *Loveless and Meade*, 2011; *Herbert and Cooke*, 2012; *Luo and Liu*, 2012; *Nicholson et al*., 2013], whereas other recent work suggests the SAF may dip 60° – 70° northeast [*Lin et al*., 2007; *Fuis et al*., 2012; *Lin*, 2013; *Lindsey and Fialko*, 2013; *Fattarusso et al*., 2014].

The SRM are structurally bounded on the southwest flank by the Santa Rosa fault (SRF), a west-dipping, high-angle (~67°) normal fault interpreted to merge at depth with the Clark strand of the SJFZ in Clark Valley [*Dibblee*, 1954; *Janecke et al*., 2010; *Dorsey and Roering*, 2006; *Dorsey and Langenheim*, 2015]. The trace of the SRF (~330°) is roughly parallel to the WSDF, and cuts WSD fault plane in the high SRM at an angle of approximately 80 – 90° to the direction of WSDF hanging wall transport (Fig. 4). The geometry of exhumed SRM block is thought to be a product of two phases of extension: (1) Miocene or early Pliocene low-angle detachment on the northeast flank, and (2) Pleistocene high-angle normal faulting on the

southwest SRM flank related to a releasing geometry within the SJFZ [*Dibblee*, 1984; *Matti et al*., 2006; *Dorsey and Langenheim*, 2015].

The bedrock lithology of the SRM is primarily Cretaceous crystalline plutonic, mylonite, and pre-Cretaceous metasedimentary units exposed in the footwalls of the SRF and the WSDF. Late Cretaceous top-to-the-east shearing produced the Santa Rosa Mylonite zone, which trends roughly parallel to the axis of the range and dips ~45° – 65° northeast along much of the range [*Simpson*, 1984]. The eastern SRM preserve up to 1.4 km of uplifted non-marine and marine, syn-and post-tectonic late Neogene strata [*Cox et al*., 2002; *King et al*., 2002; *Matti et al*., 2002; 2006]. Basal syntectonic stratigraphy on the northeast flank of the SRM correlates to the Split Mountain Formation and was thus deposited before 6.3 Ma [*Cox et al*., 2002], but the base of this section remains undated. The upper section correlates to the Canebreak Conglomerate, also known locally as the Zosel sequence [*Matti et al*., 2002; 2006]. Thermochronometric constraints on the rock uplift and exhumation history of the SRM represent important missing data for understanding the kinematics of extension during inception of the southern San Andreas system and late-phase central Salton block tilting associated with tectonic reorganization.

2.3.0 METHODS

2.3.1 AHe THERMOCHRONOMETRY

Low temperature thermochronometry (AHe) can be used to constrain large-scale structural deformation and kinematic histories of tectonic blocks where lack of geological datum precludes interpretation of uplift geometries [*Wolf et al*., 1997; *Spotila et al*., 1998; *Stockli*, 2005; *Spotila*, 2005]. We collected 29 bedrock samples in vertical and lateral transects in the SRM. Here we focus on three general locations along two range-bounding structures (Fig. 2): (1) the

SRF footwall in the southwest SRM ("*SRF", "SRR"* samples), (2) the WSDF footwall in the southeast SRM ("*ESR"* samples), and (3) the WSDF footwall near Martinez Canyon in the central eastern SRM ("*2912"* samples). We sampled structurally lowest locations along footwall localities at elevations between 3 – 300 m above sea level (asl), and in vertical transects to elevations ~1500 m asl. Sample lithology included Eastern Peninsular-Range-type granitoids, mylonites, and metasedimentary units. Generally, apatite yield and quality were high. We dated clear euhedral grains that were typically 65 – 100 μm in diameter, however samples from "*ESR"* localities contained sparse and small apatite grains, which frequently contained sub-micron scale inclusions of unknown origin.

Apatite U-Th/He thermochronometry is based on radiogenic ^{4}He production during alpha decay of parent isotopes (^{238,235}U, ^{232}Th, and ^{147}Sm) in the apatite crystal lattice [*Ehlers and Farley*, 2003; *Farley*, 2000; *Farley and Stockli*, 2002]. ^{4}He ingrowth and diffusion is temperature dependent, with total ^{4}He retention below ~40 °C and total loss of ^{4}He retention above ~85 °C [*Wolf, et al*., 1998]. The range of temperatures where ^{4}He is only partially retained is referred to as the helium partial retention zone (HePRZ), and is analogous to the partial annealing zone of the apatite fission track system. Effective closure temperatures range from 65 – 70 °C for standard Durango fluorapatite diffusion kinetics with a given cooling rate and grain size [*Dodson*, 1973; *Ehlers and Farley*, 2003; *Farley*, 2000]. Alpha ejection may decrease ^{4}He concentrations within < 20 μm of grain boundaries, and is thus corrected for using morphometric analysis and assuming homogeneous parent isotope distribution [*Farley et al*., 1996; *Farley*, 2000]. In practice, closure temperatures of sample apatite depend on cooling rate, α-ejection, crystal size and morphology, and radiation damage [*Dodson*, 1973; *Farley*, 2000; *Farley et al*., 1996; *Flowers et al*., 2009; *Shuster et al*., 2006; *Brown et al.*, 2013].

Apatite U-Th/He ages were primarily measured at Virginia Tech, however "*2912*" samples were processed and dated earlier at University of Kansas. Single and multi-grain aliquots of apatite (typically 3 – 6 aliquots per sample, with 1 – 4 grains per aliquot) were hand-picked under cross-polar magnification to avoid defects in morphology or inclusions. When possible, aliquots consisted of apatite grains > 70 μm in diameter, however scarce or small apatite in only a few samples required measurement of aliquots with diameters < 60 μm. Aliquots were loaded into Pt envelopes, degassed twice in a resistance furnace to 940 °C for 20 minutes. ^{4}He was measured by quadrupole mass spectrometry and ^{3}He spike method. Blank levels for ^{4}He detection were ~ 0.2 fmol. Radiogenic parent isotopes (^{238}U, ^{235}U, ^{232}Th, and ^{147}Sm) were measured at the University of Arizona by isotope dilution and ICP mass spectrometry [*Spotila and Berger*, 2010]. Effective Uranium (eU) content of aliquots ranged from ~10 – 200. We note only several instances where positive or negative age-eU correlation occurred, however reproducibility in those samples typically was not affected.

Predicted age uncertainty is ~5% (1σ) based on instrument precision, F_T calculations, and error in alpha-ejection correction factors [*Farley*, 1996]. Accuracy was checked against standards including Durango fluorapatite. Reported AHe age uncertainties are the standard deviation (1σ) of the replicate analyses (Table 1), however if standard deviation was < 5%, an error of 5% was assigned. Outliers in age populations were >50% higher than other aliquots from the same sample, and a total of 12 of 80 aliquots were discarded. The average standard deviation for all sample aliquots is 14.5% (after discarding outlier aliquots, and assigning 5% uncertainty to samples with <5% standard deviation). Samples from Martinez Canyon were processed at the University of Kansas in the Stockli Laboratory using the same basic methods as above, and as explained in *Shirvell et al*. [2009]. Analytical uncertainty was 3% (1σ) for these samples,

however none had standard deviations <3%, and thus reported uncertainties are standard deviations of the variance in sample aliquot ages.

2.3.2 THERMAL HISTORY MODELING

We used the software QTQt [*Gallagher*, 2012] to perform inverse thermal history modeling of vertical transects from the WSDF footwall in Martinez Canyon ("*2912"* samples) and the SRF footwall ("*SRF, SRR"* samples). QTQt uses Bayesian transdimensional Markov Chain Monte Carlo simulations that incorporate previous thermal and geological constraints. Early thermal history constraints for the Peninsular Range batholith are derived from U-Pb dating of zircons and $^{40}Ar/^{39}Ar$ of biotite, muscovite, and K-feldspar [*Axen et al*., 2000; *Grove et al*., 2003]. We modeled monotonic cooling of each aliquot for AHe samples collected in vertical transects using a Monte Carlo simulation that produced 10,000 possible temperature-time paths. We allowed a range in geothermal gradient of 20 – 30 °C/km, and a surface temperature of 10 ± 10 °C. Previous studies assign regional modern and paleogeothermal gradients that fall within the range we use to model thermal histories [*Dumitru*, 1990; *Spotila et al*., 1998; *Grove et al*., 2003; *Shirvell et al*., 2009; *Seiler et al*., 2011]. *Seiler et al*. [2011] determined an Eocene geothermal gradient of 20 – 25 °C/km in northern Baja, and argued that transient slab window heating should not have affected initial conditions of rifting in the northern Gulf Extensional Province. Despite the lack of numerous robust direct estimates of paleogeothermal gradients, we feel the use of 20 – 30 °C/km for modeling purposes is justified. We modeled the prior history for at least twice the duration of the oldest measured aliquot age.

2.4.0 RESULTS

2.4.1 APATITE U-Th/He THERMOCHRONOMETRY

AHe samples from the SRM generally display a strong positive correlation between age and elevation. Old AHe cooling ages at structurally high elevations are consistent with regional cooling histories of Peninsular-Range footwall blocks [*Wolf et al*., 1997; *Grove et al.*, 2003; *Shirvell et al*., 2009]. In general, ages become younger as elevation decreases, and the youngest AHe cooling ages (4.0 – 1.3 Ma) occur at structurally low positions and lower elevations in the SRM, and record recent and relatively rapid post-Miocene cooling.

In the northern SRM, three samples across a possible strand or northern continuation of the WSDF yield footwall ages of 50.8 ± 5.4 Ma and 8.8 ± 0.7 Ma, while the lone 'hanging wall' sample yields an age of 38.9 ± 3.5 Ma (Fig. 2). Another low elevation hanging wall sample in the east central SRM yields an age of 15.1 ± 1.2 Ma. The northern SRM contain morphological features that suggest possible fault offset along structures linked to the WSDF (Figs. 2, 3). Steep range-front topography and faceted-spur-like morphologies separate domains of high- and low-relief within the north central SRM block between Toro Peak and Deep Canyon and Palm Canyon (Fig. 2). However, colocation of disparate ages (8.8 and 50.8 Ma) along the footwall confuse the issue; a deep-seated landslide could have juxtaposed rocks from a structurally higher position against those with younger cooling histories, however kinematic interpretations based on these samples are inconclusive, and we thus focus on AHe samples from the central and southern SRM to elucidate the kinematic history of the range.

In the central eastern SRM, a vertical transect up the WSDF footwall in Martinez Canyon yields ages of ca. 5.5 ± 1.1 Ma and 6.0 ± 0.3 Ma at low elevations (190 – 260 m asl), while sample ages generally increase with elevation to 25.7 ± 3.3 Ma at the structurally highest position (960 m asl; Fig. 3). The elevation-age relationship for samples from Martinez Canyon

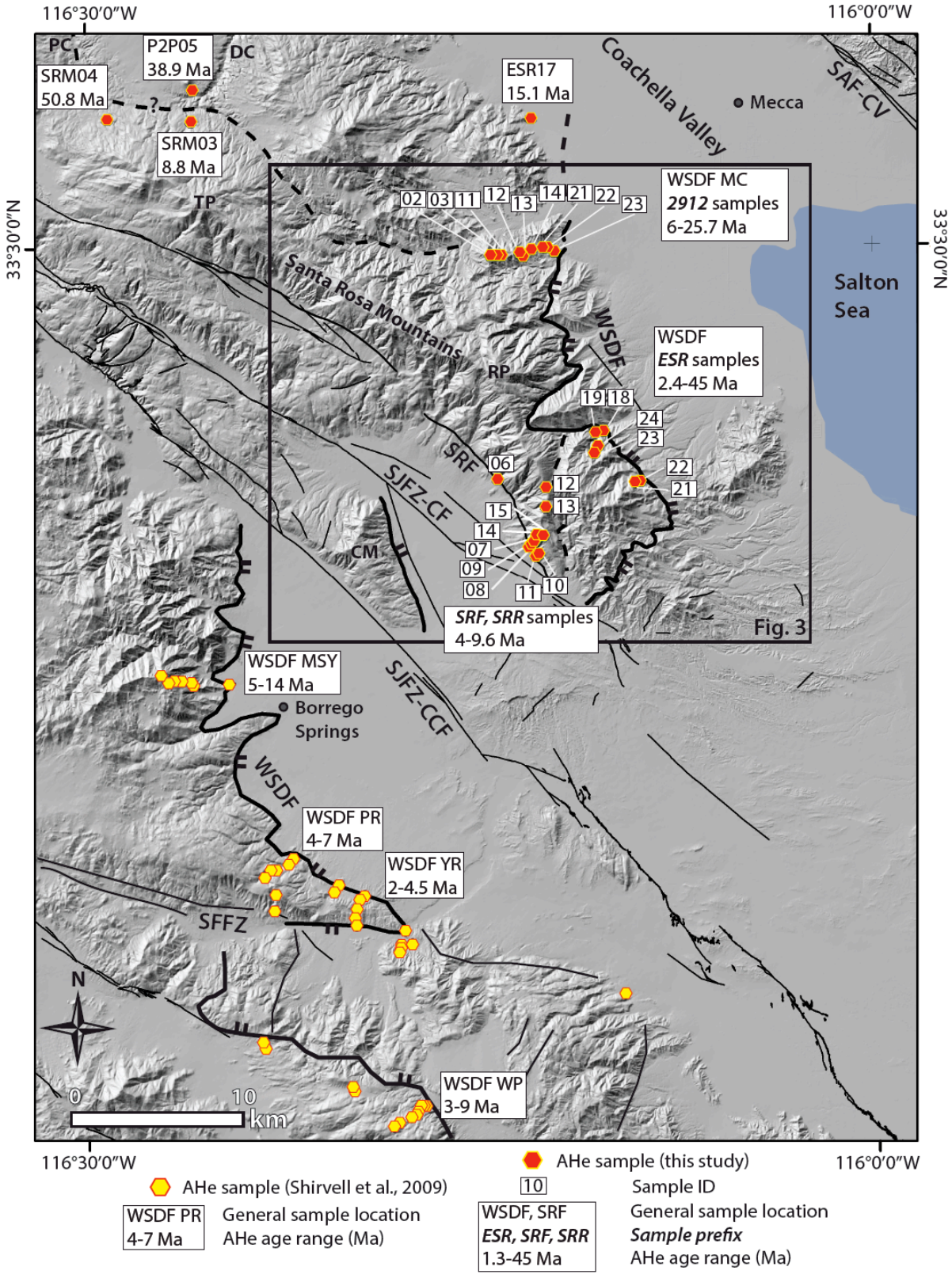
116°30′0″W
116°0′0″W
33°30′0″N
PC
P2P05
38.9 Ma
DC
SRM04
50.8 Ma
SRM03
8.8 Ma
TP
ESR17
15.1 Ma
Coachella Valley
Mecca
SAF-CV
WSDF MC
2912 samples
6-25.7 Ma
02 03 11 12 13 14 21 22 23
Santa Rosa Mountains
RP
WSDF
WSDF
ESR samples
2.4-45 Ma
19 18 24 23 22 21
Salton
Sea
SRF
06 12 13 15 14 07 09 08 11 10
SJFZ-CF
CM
SRF, SRR samples
4-9.6 Ma
Fig. 3
WSDF MSY
5-14 Ma
Borrego
Springs
SJFZ-CCF
WSDF
WSDF PR
4-7 Ma
WSDF YR
2-4.5 Ma
SFFZ
N
0
10
km
WSDF WP
3-9 Ma
AHe sample (this study)
AHe sample (Shirvell et al., 2009)
10
Sample ID
WSDF PR
4-7 Ma
General sample location
AHe age range (Ma)
WSDF, SRF
ESR, SRF, SRR
1.3-45 Ma
General sample location
Sample prefix
AHe age range (Ma)

Figure 2.2. Shaded relief map and major faults of the Coachella Valley and western Salton Trough, California. Apatite U-Th/He (AHe) sample locations from Shirvell et al. (2009) in yellow, and AHe sample locations from this study in red. Sample IDs are abbreviated after Supplementary Table S1. West Salton detachment fault = WSDF, Santa Rosa fault = SRF, San Jacinto fault zone-Clark Fault = SJFZ-CF, Coyote Creek fault = CCF, San Andreas fault-Coachella Valley = SAF-CV, Toro Peak = TP, Rabbit Peak = RP, San Felipe fault=SFF. Elevation data: U. S. Geological Survey National Map Viewer. Fault locations: Quaternary faults and folds database; *Dorsey et al*. (2011); *Shirvell et al*., (2009); *Steely et al*., (2009).

gives a gradient of ~0.036 km/Ma ($R^2 = 0.9$), with samples younging in the direction of footwall transport, and the lowest two samples yielding a vertical elevation-age gradient (Fig. 5). Samples from the southwest SRM along the SRF footwall define a good elevation-age relationship, and increase from 4.0 ± 0.7 Ma at the structurally lowest position, up to 9.6 ± 2.15 Ma along the high ridgeline. Together the SRF samples define a gradient in elevation-age space of 0.18 km/Ma ($R^2 = 0.59$; Fig. 5C).

Samples from the southeast SRM ("*ESR*" samples) represent two short vertical transects (Fig. 3). While some deviation from elevation-age relationship may be expected with multi km-scale lateral offset along a fault footwall, we note a significant deviation from expected elevation-age relationships for samples from the WSDF footwall in the southeast SRM. Sample ages from the southeast SRM ("*ESR*" samples) range from 1.3 ± 0.1 Ma to 44.9 ± 10.1 Ma, but display an inverse or inconsistent elevation-age relationship (Fig. 5A). This may relate to relatively poor apatite quality and quantity for some samples with fewer aliquots and significant age dispersion resulting in decreased precision. Possible reasons for age dispersion in "*ESR*" samples include (1) radiation damage, which can modulate closure temperatures and ^{4}He

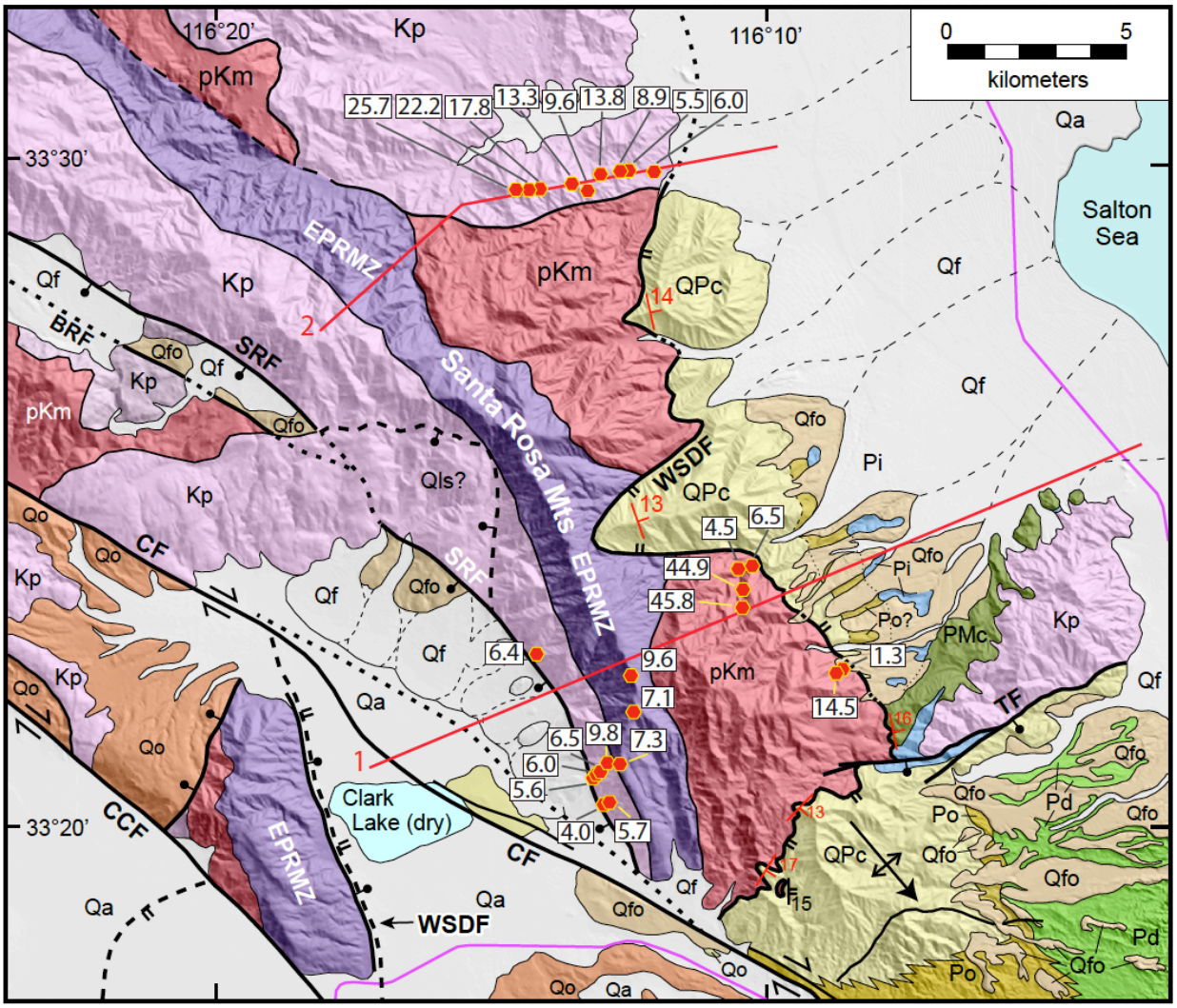

Post-Detachmt.

- Qa, Qf — Holocene: alluvium (Qa) and alluvial fans (Qf)
- Qfo — Late Quaterary: older alluvial fan deposits
- Qo — Pleistocene: Ocotillo Formation

Syn-Detachment Deposits

Palm Spring Gp

- QPc — Plio-Pleistocene: Canebrake Fm
- Po — Pliocene: Olla Formation
- Pd — Pliocene: Diablo Formation
- Pi — Pliocene: Imperial Group
- PMc — Miocene-Pliocene conglomerate: Split Mountain or Imperial Group (?)

- Kp — Cretaceous: tonalite and granodiorite
- EPR MZ — Eastern Peninsular Ranges mylonite zone
- pKm — pre-Cretaceous: metamorphic rocks

AHe sample location

6.5 AHe age (Ma)

numbered topographic profile: 1, 2

Strike and Dip of WSDF: 14 15

WSDF West Salton detachment fault

normal fault

strike-slip fault

anticline, with plunge direction

Figure 2.3: Detailed geologic map of the Santa Rosa Mountains with apatite U-Th/He (AHe) sample locations and ages, as well as topographic profiles. BRF = Buck Ridge fault, CCF = Coyote Creek fault, CF = Clark fault, WSDF = west Salton detachment fault, TF = Travertine fault. Geology compiled after *Dibblee* [1954], *Sharp* [1967], *Todd et al*. [1988], *Dorsey* [2002], *Janecke et al*. [2010]. Modified from *Dorsey and Langenheim* [2015].

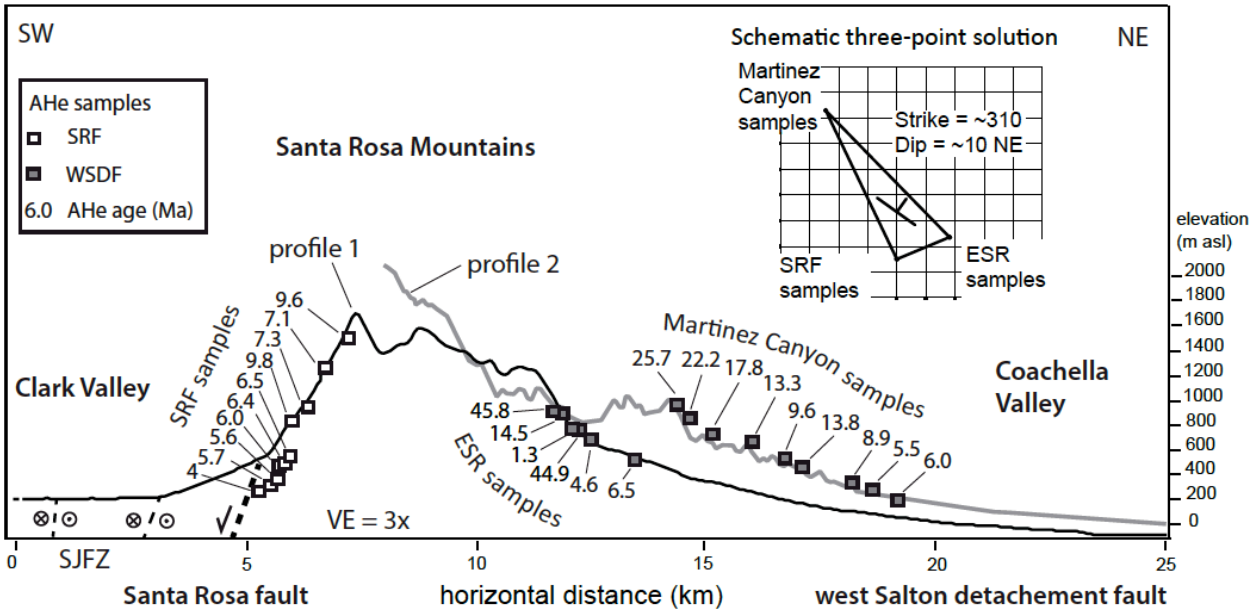

Figure 2.4: Topographic profiles across the southern and central Santa Rosa Mountains with sample locations and apatite U-Th/He (AHe) cooling ages in millions of years. Locations for profiles can be found in Figure 3. Inset schematic three-point solution for sample locations in this study, see text for details of three-point construction. SJFZ = San Jacinto fault zone. VE = vertical exaggeration.

retention systematics [*Flowers*, 2009], though there exists little evidence in our samples for systematic positive or negative age-eU correlation that affect age dispersion, or (2) Radiogenic microinclusions, (3) zonation of parent isotopes, or (4) loss of ^{4}He via microfractures. As a result of factors mentioned above, or possible unnoted structural complexity, the elevation-age gradient

for "*ESR*" samples is difficult to assess; our best guess is for a steep gradient between ca. 6.5 – 1.3 Ma, with a much lower gradient between ca. 6.5 – 14 Ma and older. This interpreted pattern for "*ESR*" samples is consistent with observations of elevation-age gradient from Martinez Canyon where samples display low gradients from ca. 25 – 6 Ma(?), and potentially a steeper gradient after ca. 6 Ma.

Elevation-age relationships from the WSDF and SRF footwalls indicate that the SRM block experienced an increase in cooling starting sometime between ca. 10 – 6 Ma, and that some regional-scale deformation has occurred since cooling of the SRM block (Fig. 4). SRF footwall samples do not appear to display the break in slope indicative of the initiation of faulting, or if so, a break in slope falls between 9.6 and 7.1 Ma (Fig 5C). Thus we speculate all or most samples resided near or below the base of the HePRZ at the time cooling initiated. Overall, samples from the WSDF in Martinez Canyon display a low gradient slope, possibly until ca. 7 – 6 Ma, which may indicate the initiation of cooling at that time. Differences in elevation between sample localities of the ~10 – 7 Ma isochrons are consistent with some degree of post-Miocene regional tilt toward the northeast [*Spotila*, 2005; *Stockli*, 2005; *Dorsey and Langenheim,* 2015]. Tilting of sample transects would change the vertical distance between samples slightly, and must be corrected in order to proceed with thermal modeling and accurate interpretation of thermochronologic data.

2.4.2 POST-WSDF TILT CORRECTIONS

Pleistocene high-angle normal faulting along the SRF was not sufficient to exhume reset AHe ages, however asymmetric Pleistocene-to-recent deformation of the central Salton block tilted Miocene isochrons within the SRM block. Quantification of the attitude of SRM tilting can

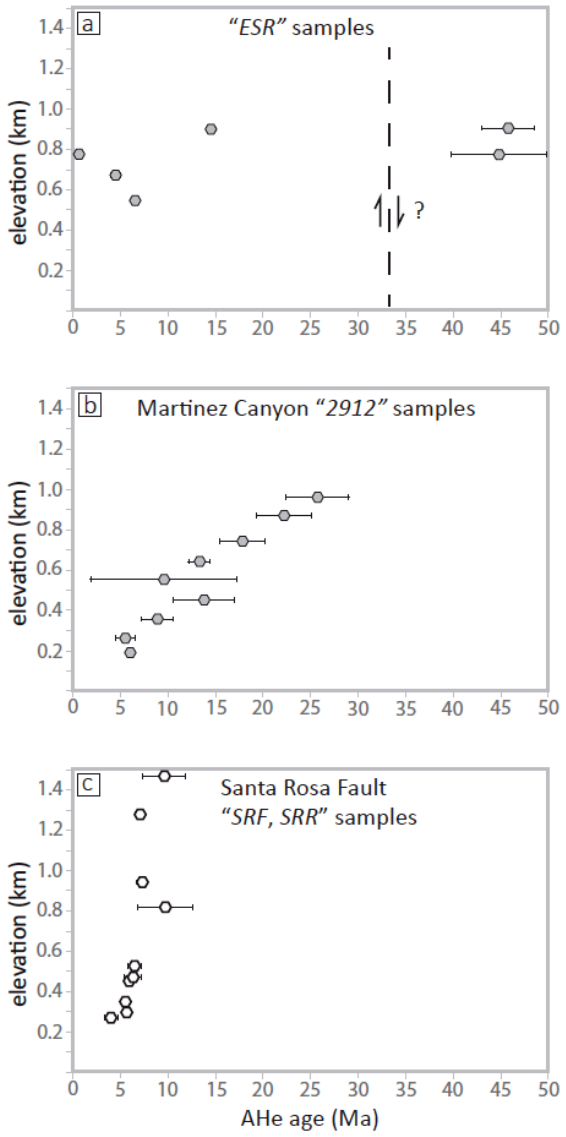

Figures 2.5: Elevation-age plots for samples of apatite U-Th/He from the Santa Rosa Mountains. **A**: samples form the eastern Santa Rosa Mountains (SRM) along the footwall of the west Salton detachment fault (WSDF). See text for discussion of elevation-age relationship, and possible structural complexity at this location. **B**: Elevation-age relationship for samples from Martinez Canyon along the WSDF footwall, eastern SRM. **C**: samples form the Santa Rosa fault (SRF) footwall in the southwest SRM. All error bars are standard deviations (1σ) of sample replicates.

be accomplished using AHe isochrons and a 3-point approach, and compared to independent estimates of tilting of the central Salton block [*e.g. Dorsey and Langenheim*, 2015]. The ~10 – 7 Ma isochrons may be projected from Martinez Canyon at ~350 – 450 m asl (ca. 9.8 – 7 Ma; "*2912*" samples) to ~1200 – 1470 m asl in the SRF footwall (ca. 9.6 – 7 Ma; "*SRR, SRF*" samples). Projecting the isochron to the southeast SRM introduces some uncertainty due to suboptimal elevation-age relationship in that locality. We allow for a range of elevations for the ~10 – 7 Ma isochron surface in the southeast SRM (700 ± 250 m; "*ESR*" samples). Magnitude of tilt is only affected by 2 – 3° using a range of isochron elevations. Another source of uncertainty is a potential oversimplification of isochron geometries, as warped or convex-up isochrons cannot be distinguished or ruled out with the resolution of our thermochronologic data set. We find the ~10 Ma isochron surface has a strike of ~310 – 315° and a dip of ~8 – 12° northeast. If the WSDF split into multiple strands in the central and northern SRM block, then restoration of any post late Miocene down-to-the-east slip (The most reasonable alternative kinematic interpretation) for Martinez Canyon samples would become necessary. However, even with ~600 m of slip restoration for Martinez Canyon samples, the 3-point calculation results are extremely similar, with the strike of the ~10 Ma isochron changing from ~310° to ~320°.

Tilting of the central Salton block by ~8° northeast is consistent with results from several other workers [Extensively reviewed in *Dorsey and Langenheim*, 2015]; an identical geometry of tilting for the central Salton block is indicated by catchment-and fan-area relationships for the southwest and northeast SRM, and gravity data showing progressive northeast deepening of sedimentary fill toward the SAF in Coachella Valley indicates some northeast tilt [*Langenheim et al*, 2005]. Subsurface stratigraphic patterns below the Salton Sea indicate growth strata dip 5 – 8° northeast toward the Coachella strand of the SAF [*Fuis et al*., 2012]. Late Neogene

sedimentary units in the eastern SRM have been uplifted and tilted northeast [*Cox et al*., 2002; *Matti et al*., 2002; 2006], thus large-scale isochron tilt estimates agree well with other lines of independent evidence.

Northeast tilt must be restored in order to correctly interpret the late Miocene kinematic history of the SRM block using thermal history modeling or elevation-age data. We use a regional tilt model with 8° of northeast tilt since inception of the SJFZ in the Pleistocene (ca. 1.2 Ma), and used a rotation matrix to restore the elevations of samples from the Martinez Canyon and SRF transects. We chose a fulcrum of tilt within the modern alluvial fans on the eastern bajada of the SRM [*Dorsey and Langenheim,* 2015]. We then pinned the base of the tilt-corrected transects to the lowest modern sample elevation for each transect, and adjusted the offset between samples to correspond to the tilt-corrected elevation offsets. We used these adjusted sample elevations to perform quantitative thermal modeling, as outlined in a following section.

Tilt-restored sample elevations result in lower elevation-age gradients for both transects (Fig. 7a, b). The modern inactive WSDF has a dip of ~15º northeast, but a pre-tilt WSDF may have had a much shallower dip of ~7º (also discussed in 5.2) A tilt-restored SRF transect has a new gradient of 0.15 km/Ma (R^2 = 0.54), while the Martinez Canyon transect has a corrected gradient of 0.012 km/Ma (R^2 = 0.88). The tilt-reconstructed zero-age depth for the SRF transect is ~2.1 km depth, compared to 0.55 km depth in the uncorrected transect [*e.g*. *Spotila*, 2005]. Tilt-corrected paleo-elevations place the highest SRF samples at similar positions to those of the lowest Martinez Canyon samples in paleo elevation-age space, improving the internal consistency of paleo elevation-age relationships across the SRM block. This method of tilt reconstruction takes a simplistic 2-D approach at restoration of recent deformation, and modeling

of previous thermal histories. A thermo-kinematic model might offer a more thorough 3-D thermal evolution. However, because these data are only consistent with a northeast tilt, and due to the localized scope of our study, such a modeling exercise seemed unjustifiably complex.

2.4.3 THERMAL HISTORY MODELING

Quantitative thermal modeling may be used to complement results of AHe elevation-age data [*Ketcham*, 2005; *Gallagher*, 2012]. Figure 6 shows T-t paths for inverse thermal history modeling of multi-sample transects from the WSDF and SRF footwalls. Parameters for inverse thermal history model runs, including prior thermal constraints and durations, are as outlined in section 3.2, and elevation corrections were made as outlined in section 4.2 above. "*ESR*" samples were not used in quantitative thermal history modeling due to their relatively poor elevation-age relationship. Nevertheless, this configuration of samples from low- and high-angle normal fault footwalls affords a unique thermal perspective through the WSDF footwall and insight into the thermal history of the SRM block.

Inverse model results from transects in Martinez Canyon and the SRF footwall indicate synchronous and rapid late Miocene cooling beginning at ca. 8 Ma. Figure 6A shows that the samples from Martinez Canyon may have resided within the HePRZ during early Miocene time, while the modeled T-t path may also indicate a prior history including a cooling event during late Oligocene through early Miocene time (ca. 30 – 20 Ma). The oldest aliquot age is ~28 Ma and the confidence envelopes are consistent with slow or rapid cooling during late Oligocene to early Miocene time. Samples remained nearly isothermal until they experienced an increase in cooling rate at ca. 8 Ma at a rate of 5 – 6 °C/Ma. Inverse model results from a transect of 10 samples on

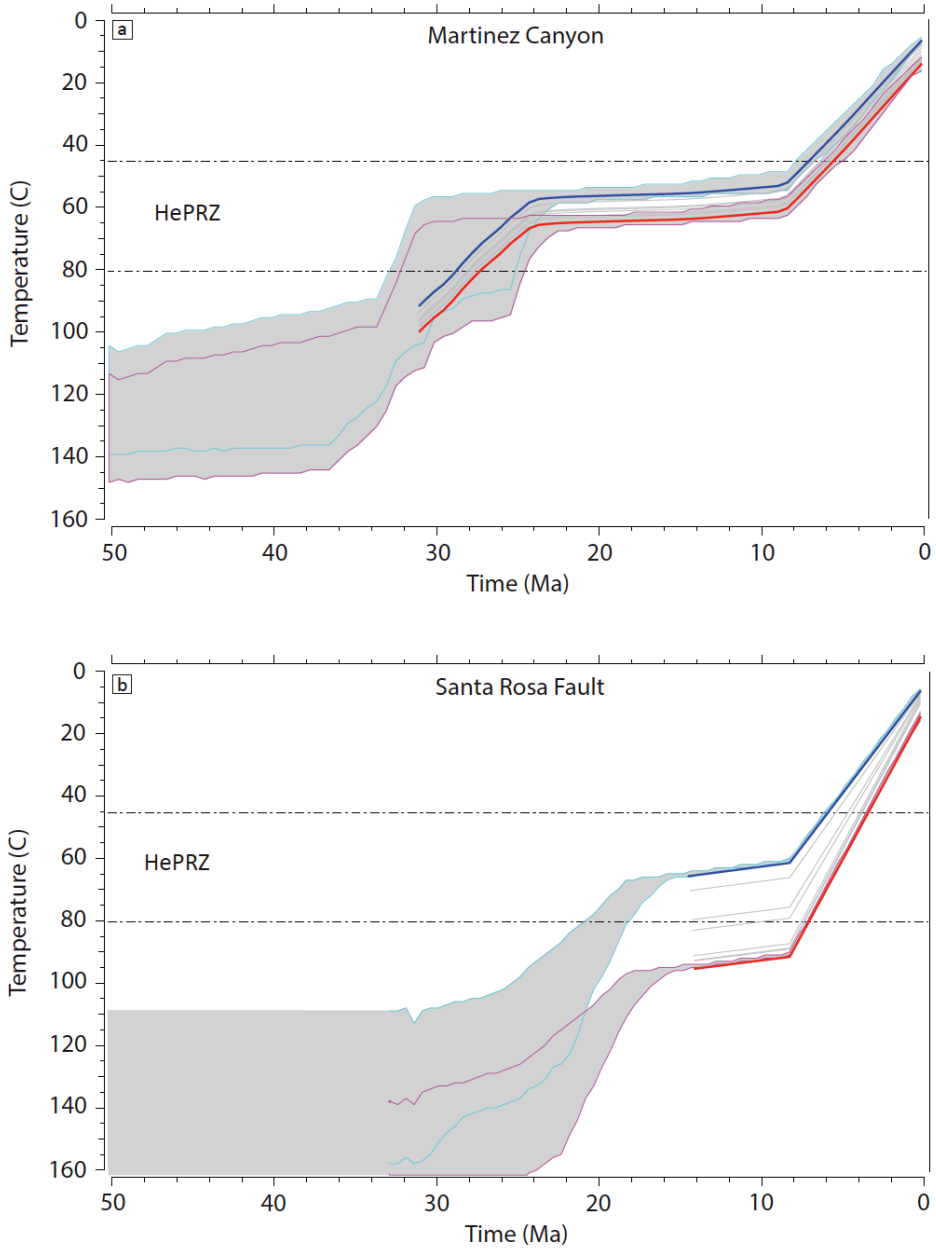

Figure 2.6: QTQt thermal history model results for apatite U-Th/He (AHe) samples from the Santa Rosa Mountains. **6a**: Inverse model results showing best fit temperature-time histories for samples from Martinez Canyon ("*2912"* samples*)*. **6b**: Inverse model results showing best fit temperature-time histories for samples from the Santa Rosa fault footwall ("*SRF*", "*SRR*" samples). Grey shaded areas are 95% confidence envelopes. Red and blue lines represent structurally lowest and highest samples, respectively,

with intermediate grey lines representing other sample elevations/temperatures. Pre-Miocene thermal constraints in model from *Grove et al*. [2003]. HePRZ = He partial retention zone.

the SRF footwall (Figure 6B, "*SRF*", "*SRR*" samples) display a T-t path indicating slow cooling during the middle Miocene; then at 8 Ma the cooling rate increased to ca. 8 – 9 °C/Ma and continued through the Pleistocene. The lowest 4 – 5 samples likely resided below the HePRZ during the early Miocene, and thus their cooling ages probably reflect rapid vertical advection through the HePRZ. While the independent T-t paths agree on synchronous onset of late Miocene cooling, there is a slight discrepancy in cooling rates, and thus a brief discussion of the model results is in order.

First, inverse model results show a T-t path from Martinez Canyon samples that indicates slower cooling than the T-t path from the SRF samples (ca. 5 – 6 °C/Ma vs. ca. 8 – 9 °C/Ma, respectively). Possible causes for discrepancies in the inverse models are numerous, and include possible local variability in geothermal gradient, sample errors, variation in elevation, isochron geometry, and possible local structural complexities. We note the position of the WSDF directly above Martinez Canyon samples might have resulted in rapid cooling relative to the SRF sample, yet observe the opposite in model results. One possible influence on the T-t paths could be the interpreted long duration of residence in the HePRZ for Martinez Canyon samples. While the cumulative effect of uncontrolled variables results in somewhat imprecise modeled T-t paths, the model results taken together indicate a broadly self-consistent thermal history for the SRM block, which indicates a late-Miocene increase in cooling of the Santa Rosa Mountains starting at 8 Ma.

2.5.0 DISCUSSION

Qualitative and quantitative analyses of the 3-D spatial patterns and ages of AHe samples from the SRM indicate an abrupt increase in cooling rates beginning at ~8 Ma in the late Miocene. Available structural data indicate that late Miocene cooling was caused by tectonic exhumation along the low-angle WSDF in the eastern SRM. During middle Pleistocene time, a second phase of tectonism along the southwest flank of the SRM exhumed a structurally lower section of WSDF footwall via the high-angle SRF. The geomorphology of the SRM, including catchment and fan areas, relative steepness and relief [*Dorsey and Langenheim*, 2015], along with the timing of SJFZ initiation [*Lutz et al*. 2006; *Janecke et al*., 2010], provide constraints on the kinematics of late phase tectonic exhumation and extension. In the following sections we present detailed interpretations of thermochronologic data from across the SRM block that constrain timing of WSDF slip (*5.1*). We then discuss constraints on the magnitudes and rates of extension and exhumation in the SRM within a regional tectonic context (*5.2*). Finally, we discuss the implications of different geologic rates related to each phase of normal faulting in the context of plate tectonics and local fault geometry associated with evolving major strike-slip faults of the southern SAF system (*5.3*).

2.5.1 8-MA ONSET OF EXHUMATION OF THE WSDF FOOTWALL

While elevation-age relationships from AHe samples in Martinez Canyon and the SRF footwall broadly constrain initiation of the WSDF to between ca. 10 – 6 Ma, tighter age constraints can be achieved by integrating these estimates with quantitative model results. Figure 6 shows synchronous increased cooling starting at 8 Ma for sample transects along the east and southwest SRM block (Fig. 6A and 6B, respectively). These results of thermal history modeling,

combined with elevation-age relationships, demonstrate tectonic exhumation of the SRM most likely occurred beginning at ca. 8 Ma. Our preferred age of ca. 8 Ma for initiation of the WSDF using AHe data from the SRM is consistent with onset of regional extension and fault-controlled basin formation deduced from stratigraphic records on the northeast flank of the SRM [*Cox et al*., 2002] and in the Fish Creek – Vallecito basin; [*Dorsey et al*., 2007; 2011]. It also is consistent with studies in the northern Gulf of California that date onset of strong regional extension and transtension at ca. 9 – 7 Ma (e.g., *Bennett et al*., 2013; *Seiler et al*, 2013), which likely was caused by a change in direction of Pacific-North America relative motion at ca. 8 Ma (*Atwater and Stock*, 1998; *Bennett et al*., 2016).

The relative paleo-depth of the SRF transect below the Martinez Canyon transect, as inferred from elevation-age data, is supported by thermal modeling results. Figure 7 shows that the SRF samples cooled from temperatures as high as ~100 – 90 °C since the late Miocene, while samples from the eastern SRM, essentially the low angle fault plane surface, were likely within or near the base of the HePRZ (~80 – 65 °C) before late Miocene fault initiation. This configuration is consistent with the low gradient of the Martinez Canyon transect in elevation-age space, and the relatively steep gradient of the SRF transect (0.012 vs. 0.15 km/Ma). Another result of this configuration is an apparent increase in spacing between the isochrons in the SRM compared to those from Martinez Canyon, which have a smaller spacing due to prolonged residence in the HePRZ [*Stockli*, 2005].

Young AHe ages from the southeast SRM ("*ESR*" samples) record extension-related cooling starting in late Miocene time. Older AHe ages (> 45 Ma) do not fit into the overall context of other footwall samples in the southern SRM. The quality and quantity of apatite from samples in this area were generally poor, yielding fewer aliquots that typically displayed

significant age dispersion (Table S1 in supporting information; *ESR* samples). Several plausible explanations can be offered for anomalous old ages and elevation-age reversals in the southeastern SRM (some outlined in section 4.1), including multi kilometer-scale lateral separation of samples that could cause elevation-age reversals when plotted together. Recent deformation related to the initiation of the SJFZ could affect the anticipated pattern of AHe cooling ages in elevation-age space, but lack of detailed structural mapping or strain markers preclude a robust evaluation of sub-km-scale recent deformation. We suspect that older AHe ages may reflect small unmapped allochthonous klippen that were excised during extension; in other words, we may have sampled remnants of WSDF hanging wall that cooled in Eocene time. This idea is consistent with low-relief Eocene surfaces in the surrounding Peninsular Ranges [*Minch*, 1979; *Abbott and Smith*, 1989]. *Shirvell et al*. [2009] observed thin middle plate slices between strands of the WSDF south of the SRM. Detailed structural mapping would aid in reconciliation of anomalous old ages juxtaposed with late Miocene – Pleistocene ages. Whatever the mechanism, a lack of monotonic elevation-age relationship precludes a robust slip history analysis for "*ESR*" samples. Nevertheless, AHe ages do fit broadly into the context of Eastern Peninsular Range cooling histories, and indicate active exhumation of the southeast SRM block between 6.5 and 1.3 Ma.

2.5.2 RATES AND MAGNITUDES OF EXHUMATION

Rates of vertical exhumation along the low-angle WSDF aid reconstructions of the insipient plate boundary in Coachella Valley, but assigning rates and magnitudes of slip to the WSDF depends upon the measure of cooling, and there are several possible scenarios that should be examined. For instance, elevation-age gradients yield a measure of long-term vertical

exhumation associated with the WSDF. For the SRF transect, this rate is ~0.15 km/Ma (tilt-corrected) since WSDF initiation. The elevation-age gradient for Martinez Canyon is low due to residence in the HePRZ, and tells us little about exhumation rate. However, a second measure of vertical exhumation uses the results of thermal history modeling, which show cooling rates of ~5 – 9 °C/Ma (Martinez Canyon and SRF footwall, respectively), translating to vertical exhumation rates of 0.20 – 0.36 km/Ma, from depths of up to 3.4 km (25 °C/km geothermal gradient). Yet a third approach uses closure temperature estimates for vertical exhumation. For all "*SRF*" and "*ESR*" samples, we calculated a mean closure temperature of 65 °C ± 4 °C (1σ standard deviation of the variance) [*Wolf et al*., 1996, 1998; *Farley and Stockli*, 2002; *Ehlers and Farley*, 2003]. We then used a geothermal gradient of 25 °C/km, a closure temperature depth of 2.2 ± 0.2 km, and estimates of post-WSDF sample paleodepth (tilt-corrected) and AHe cooling ages to calculate rates of time-averaged vertical uplift [After *Stockli*, 2005; *Spotila*, 2005]. The results are minimum vertical exhumation rates between ~0.15 – 0.22 km/Ma for structurally low samples from the SRF footwall. The use of non-tilt-corrected, modern sample elevations yield rates between 0.4 – 0.6 km/Ma, somewhat higher than those derived from elevation-age gradients, T-t paths, and closure technique using post-WSDF-tilt corrected sample paleodepths. In summary, it is difficult to assess which measure most accurately tracks WSDF exhumation rates, however the remarkable similarity between rates using the first three techniques may indicate vertical exhumation along the WSDF was between 0.15 – 0.36 km/Ma, from ca. 8 Ma through the inception of the SJFZ at ca. 1.2 Ma. Using this framework, we may then infer WSDF slip rates, and partition vertical exhumation into WSDF- or Pleistocene SRF-related exhumation.

Low to moderate rates of vertical exhumation since 8 Ma may not necessarily reflect slow fault slip rates. Since Martinez Canyon samples represent an uplifted HePRZ, AHe data do

not directly constrain slip rates along the WSDF footwall [*e.g. Foster et al*., 1993]. However, geometric relationships between vertical exhumation rate and assumed fault dip permit coarse slip-rate estimates. For vertical exhumation rates of 0.15 – 0.36 km/Ma, and a fault-plane dip of 30° northeast, the resulting range of slip rates is 0.3 – 0.7 km/Ma. The distribution of northeast dips along the eastern SRM cluster near 15° to the northeast (Fig. 3), and restoration of Pleistocene tilting results in a shallower dip of ~7°. Using this configuration, fault slip rates could have been ~1.2 – 3.0 km/Ma in a direction orthogonal to the SRM block (~060º – 080º northeast).

Intermediate and low slip rates for detachment faults associated with diffuse deformation along the Pacific-North America plate boundary have been previously documented; in Death Valley, the Black Mountain detachment slipped at a modest rate of <1 mm/yr (equivalent to 1 km/Ma) during the Pleistocene, while in eastern Searles Valley, a detachment bounding the Slate Range slipped at a low rate of 0.2 – 0.35 km/Ma during the Pleistocene [*Hayman et al*., 2003; *Numelin et al*., 2007]. Detachment-related core complexes in the Basin and Range and Colorado River extensional corridor corresponding to longer timescales of extension yield fault slip rates on the order of 6 – 8 km/Ma, and 3 – 6 km/Ma respectively [summarized in *Foster and John*, 1999]. The late Miocene to Pleistocene evolution of the proto southern SAF zone from transtension to transpression may have precluded major rapid east-west directed extension in the northern Salton Trough. Another speculative explanation is a paleo-fault slip gradient for the northern tip of a regional detachment system with lower rates in the northern Salton Trough than further south.

Rocks from the SRF footwall cooled through the HePRZ in the late Miocene through Pleistocene during slip on the WSDF from depths >3 km, but probably resided within the upper

1.5 km of Earth's surface until they were further exhumed by slip on the high-angle SRF beginning ca. 1.2 Ma [*Dorsey et al*., 2012; *Kirby et al*., 2007; *Lutz et al*., 2006; *Steely et al*., 2009; *Janecke et al*., 2010]. AHe ages were not reset by exhumation on the SRF and therefore do not reflect the youngest phase of tectonism. However, using the same estimates for tilt-corrected post-WSDF paleodepth, we may constrain the rate and absolute magnitude of Pleistocene exhumation (Fig. 7). We may rule out exhumation from depths below the closure temperature of apatite (>2.2 km), in agreement with our tilt-reconstructed sample paleo-depths that indicate maximum post-WSDF paleodepths of ~1.4 km for samples from the SRF. If the lowest samples along the SRF were exhumed to their modern elevations from a tilt-corrected position starting at 1.2 Ma, the range of vertical exhumation rates is then ~1.3 – 1.4 km/Ma. Rock uplift magnitude associated with SRF slip is difficult to constrain independently, but one slip-rate estimate based on faceted-spur morphology brackets our estimate at 0.5 – 2.0 km/Ma [*Dorsey and Langenheim*, 2015; after *dePolo and Anderson*, 2000]. While initiation of the SJFZ was a major tectonic event responsible for rapid dextral translation of crust and major vertical motions associated with releasing geometry along the southwest SRM, the thermal history of the SRM was not significantly affected by these processes. It is clear however that post 1.2 Ma in the SRM represents a period of punctuated and high-rate uplift along a broad swath of the western central Salton Block, which may have been driven in part by transpression along the SAF during the middle-late Pleistocene.

Rates of vertical exhumation in the SRM yield new insights into the kinematics of two extensional fault systems over two timescales: (1) initiation of WSDF resulted in relatively slow to intermediate vertical exhumation rates of ~0.15–0.36 km/Ma, ca. between 8 – 1.2 Ma; and (2) vertical rates increased at least three-fold to ~1.3 km/Ma during initiation of the SJFZ. The total

vertical exhumation attributable to slip on the WSDF, as constrained by interpretations of the Miocene HePRZ and thermal modeling, was ~3.4 km for the crustal section along the SRF footwall, and closer to 2.2 km for samples from Martinez Canyon. The WSDF-related vertical rates can be associated with fault-slip-parallel rates as high as 1.2 – 3.0 km/Ma, depending on an assumed geometry of the WSDF footwall dip. Subsequent faulting on the SRF in the southwest SRM may have exhumed an additional 1.3 – 1.7 km of crustal section since SJFZ/SRF initiation at ca. 1.2 Ma (Fig. 7), at relatively high rates compared to WSDF-related exhumation. These estimates are dependent upon our reconstructions of post-WSDF paleodepth using a regional tilt model supported by isochron geometries in the SRM, and independent evidence (summarized in section 2.3). Still, uncertainty in the geothermal gradient, tilt magnitude, location of fulcrum, and in the elevation of the base of the HePRZ causes some uncertainty in the absolute magnitude of exhumation of the SRM block, and thus the exhumation budgets associated with late Miocene and Pleistocene uplift. Still, results of our exhumation budget for the SRM, indicate total exhumation since 8 Ma was highest in the southwest SRM, and was ~30 – 40% less for the northeastern SRM over the same timescale. Finally, low to intermediate vertical exhumation rates beginning at 8 Ma may indicate different kinematics of late-Miocene extension in the northern Salton Trough than in the Gulf Extensional Province to the south.

2.5.3 IMPLICATIONS

The SRM and greater central Salton block have undergone a complex late Cenozoic tectonic evolution, and the vertical kinematics of the SRM block tracks with two phases of tectonism since the late Miocene. Figure 7 displays reconstructed modern- and paleo-elevation-age relationships for each resolvable timeframe within this study, and offers illustrative

conceptual tectonic block diagrams that are consistent with interpretations made herein using AHe and thermal history modeling. The initiation of WSDF extension at ca. 8 Ma is undoubtedly responsible for an increase in cooling rate of the SRM block from temperatures of up to ~100 – 90 ºC, and thus exhumation from ~3.4 km depth (Fig. 6B). However, the generation of modern topographic relief in the southern SRM is the product of recent and relatively rapid uplift associated with initiation of the SJFZ and modern crustal tilting possibly driven by crustal loading along a steeply dipping SAF in Coachella Valley. The relative magnitudes and rates of deformation along these two different normal fault systems yield new insight regarding relationships between local fault geometry and rock uplift associated with major strike-slip faults, and new insight into the Pacific-North America plate boundary within Coachella Valley.

Initiation of the WSDF at ca. 8 Ma indicates a link between clockwise rotation in Pacific-North America plate velocities and formation of the southern SAF system [*Atwater and Stock*, 1998]. Furthermore, the timing of extension and plate boundary localization in Coachella Valley is nearly synchronous with 8 – 6 Ma plate boundary localization along the length of the Salton Trough and the Gulf of California [*Pacheco et al*., 2006; *Dorsey et al*., 2011; *Seiler et al*., 2011; 2013; *Bennett et al*., 2013; 2016]. These results indicate deformation in the northern Salton Trough was strongly partitioned between extension and strike-slip beginning with the inception of the transform plate boundary in the Salton Trough at ca. 8 Ma. These results require reexamination of interpreted tectonic drivers related to an early (>12 Ma) inception of the WSDF southwest of our study area [*Shirvell*, et al., 2009]; In the case of the northern Salton Trough, we emphasize that inception of the WSDF and SAF in Coachella Valley occurred simultaneously, and little evidence exists for progression from extension to transform style deformation. Thus, the pre-8 Ma history of the Salton Trough is quite different from that of the Gulf of California.

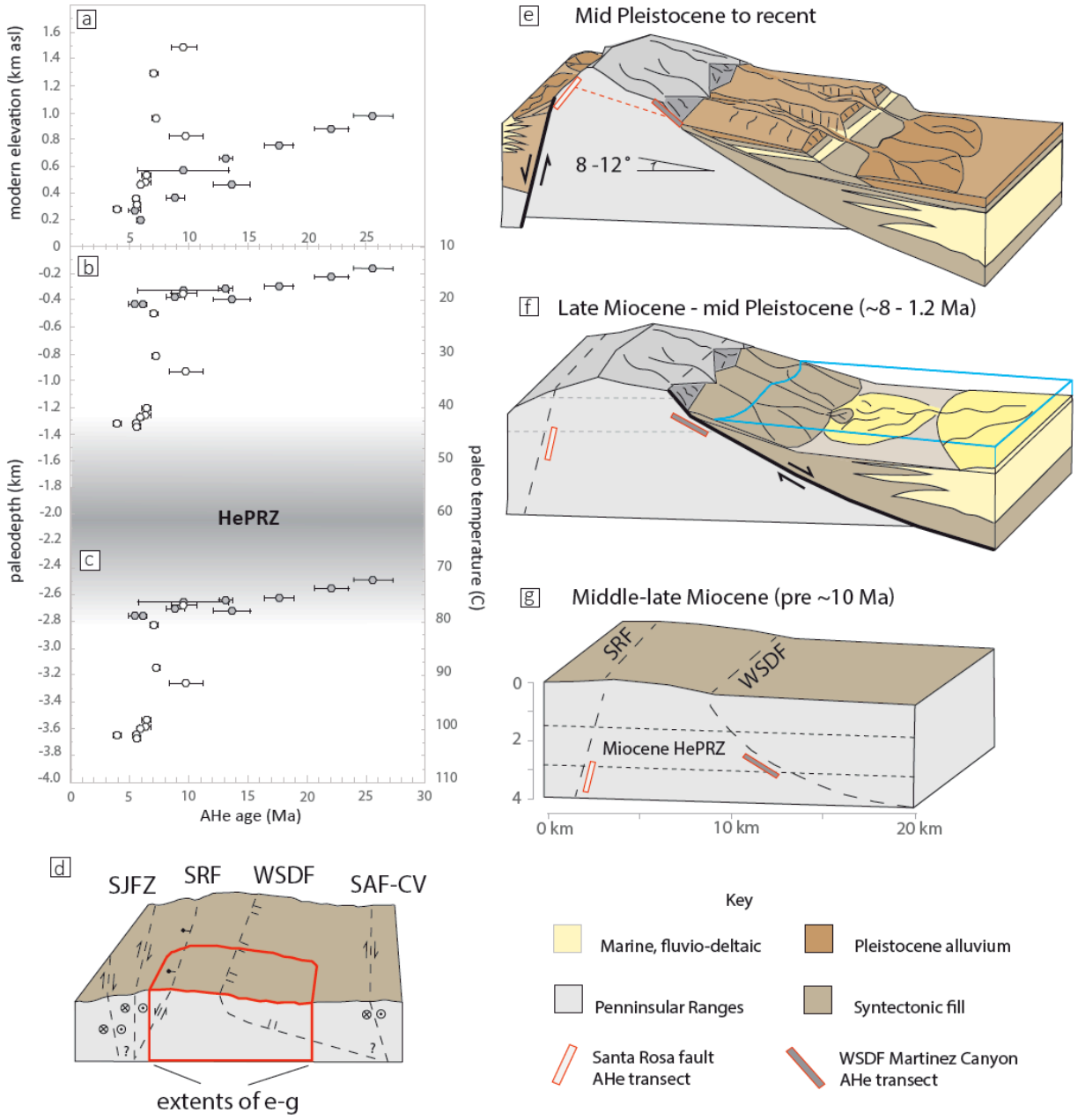

Figure 2.7: Paleo elevation-age relationships for samples from the Santa Rosa Mountains (SRM) with structural block diagrams for each relevant time step. **a**: modern sample age-elevation relationships. White hexagons are samples from the Santa Rosa fault (SRF), while grey filled hexagons are from the west Salton detachment fault (WSDF) footwall in Martinez Canyon. **b**: Post-WSDF tilt-corrected elevation-age relationships (See text for details). **c**: Pre-detachment paleodepth and paleo-temperature reconstruction for WSDF footwall rocks. **d**: Block diagram showing schematic tectonic configuration

between the San Jacinto (SJFZ) and San Andreas in Coachella Valley (SAF-CV). **e – f** Evolution of the WSDF-SRM system from thermochronologic results. Sample transect locations denoted by rectangles along west and east flanks of SRM. **e**: Modern configuration of the SRM block, showing active Santa Rosa fault and inactive WSDF. **f**: Active to post-detachment phase of the SRM, showing deposition of coarse-grained alluvial fans and marine to fluvio-deltaic deposits derived from the Colorado River. **f**: Detailed schematic pre-detachment configuration. Location of block diagrams within SRM similar to topographic profile 1 in Figure 3.

However, the post-8 Ma tectonic history of the Salton Trough is synchronous with initiation of strong dextral shear and basin subsidence between 9 – 7 Ma along much of the plate boundary in the Gulf of California. This might be because the east Pacific Rise had already impinged on continental crust at the latitude of the northern Salton Trough by late Oligocene to early Miocene time, shutting off subduction and back-arc spreading in southern California and imposing an early transpressive regime.

Regional tectonic reorganization during the Pleistocene led to punctuated, high rate vertical deformation along the southwest SRM. High-angle normal faulting along the SRF may have separated hanging wall from footwall by up to ~5 – 6 km in the Clark Valley, while uplift along the western margin of the central Salton block elevated syn- and post-tectonic strata on the east flank of the SRM to ~1.4 km above sea level [*Matti et al*., 2002; Dorsey and Langenheim, 2015]. The total magnitude of uplifted sedimentary deposits, ~1.4 km, is similar to estimates of vertical rock uplift in the SRM since ca. 1.2 Ma, using a regional tilt model constrained by thermochronometry and independent evidence [*Fuis et al*., 2012; *Fattaruso et al*., 2014; *Dorsey and Langenheim*, 2015]. Transpression and structural complexity within strands of the southern

SAF zone is known to result in rapid vertical exhumation of spatially restricted crustal slivers [*Spotila et al*., 2001]. Deformation of the central Salton block is accommodated by the high-angle geometry of the SRF, which is most likely a negative flower structure that roots into the Clark fault of the SJFZ at depth, but the recent broad uplift of the SRM may be driven by oblique convergence along a steeply dipping SAF in Coachella Valley [*Dorsey and Langenheim*, 2015]. The spatial extent of vertical deformation along the western central Salton block between the SJFZ and the SAF implies changes in local fault geometries can result in both high rates of spatially restricted exhumation, and affect far off-fault deformation over relatively short timescales (~1 Ma) and over relatively large regions (100s km^2) of transform plate boundaries.

CONCLUSIONS

New low-temperature thermochronometry (apatite U-Th/He; AHe) and thermal history modeling from the Santa Rosa Mountains (SRM), western Coachella Valley, constrain two phases of extensional faulting. The first starting first at ca. 8 Ma along the low-angle east-dipping west Salton detachment fault (WSDF)—a major regional fault within the southern San Andreas fault (SAF) system—followed by a second phase close to 1.2 Ma along the high-angle west-dipping Santa Rosa Fault (SRF), an extensional splay of the San Jacinto fault zone. Elevation-age data from vertical transects of AHe samples from the eastern SRM indicate an uplifted Miocene helium partial retention zone, while samples from the SRF footwall on the southwest SRM represent a deeper crustal section, which cooled initially during WSDF slip, then was fully exhumed during slip on the high-angle SRF. Pre-WSDF footwall paleodepth for structurally low samples from the SRF footwall were between ~4.5 – 3 km (geothermal gradient = 25 ± 5 °C/km) at the onset of WSDF related exhumation, and vertical exhumation rates were

likely between 0.15 – 0.36 km/Ma since WSDF initiation at ca. 8 Ma through ca. 1.2 Ma. Fault slip rates between 8 – 1.2 Ma are constrained by the vertical component of exhumation; assuming a low-angle WSDF with a dip of 15º – 7º, slip rates were ~1.2 – 3.0 km/Ma. Total exhumation was partitioned between the low-angle detachment phase, and a second high-angle phase along the SRF, responsible for ~1.3 – 1.7 km of vertical displacement at rates of ~1.3 km/Ma, as constrained by a regional tilt model, geometry of AHe isochrons in the SRM, and elevations of uplifted Neogene sediments along the eastern SRM.

Initiation of the WSDF at ca. 8 Ma supports a model in which plate boundary localization in the Salton Trough was driven by the ~15 – 20º clockwise rotation of Pacific-North America plate velocities [*Bennett and Oskin*, 2014]. The lack of early to middle Miocene extension in the western Salton Trough implies a very different tectonic evolution than that of the Gulf Extensional province, likely related to the early cessation of subduction due to impingement of the east Pacific rise, and earlier inception of the San Andreas transform boundary northwest of the Salton trough. High-angle normal faulting associated with post-late Miocene transpression within the southern SAF system has partially overprinted the kinematics of the rifted western margin by dissecting the WSDF and asymmetrically tilting the central Salton block toward the northeast. While low-temperature thermochronology has defined restricted, high-magnitude exhumation of crustal slivers between major strike-slip fault splays [e.g. *Spotila et al*, 2001], this study highlights the occurrence of punctuated, wide-spread relatively rapid vertical deformation of a crustal-scale block between the SAF zone and the SJFZ. These results indicate local fault geometry, and not plate tectonic obliquity, exerted a fundamental control on rock uplift rates along the SJFZ during an overall evolution from transtension to transpression within the Pleistocene southern SAF system.

ACKNOWLEDGMENTS

Support for this study was provided by National Science Foundation grant EAR-1145115 (Spotila), and EAR-0125307, EAR-0337775 and EAR-0809638 (Axen), and EAR-1144946 (Dorsey). CM would like to acknowledge the Tectonics and Geomorphology Research Group and the Sedimentary Systems Research Group at Virginia Tech for constructive feedback. CM acknowledges Paul O'Sullivan for assistance with sample preparation. All sample location and isotopic data used in this study are available as supplementary material in Table S1.

REFERENCES

Abbott, P.L., T.E. Smith (1989), Sonora, Mexico, source for the Eocene Poway Conglomerate of southern California, *Geology*, 17, 329-332, doi: 10.1130/0091-7613[1989]017<0329:SMSFTE>2.3.CO;2.

Atwater, T., (1970), Implications of Plate Tectonics for the Cenozoic Tectonic Evolution of Western North America, *Geol. Soc. Am. Bull*., 81, 3513–3536.

Atwater, T., (1989), Plate tectonic history of the northeast Pacific and western North America, *in* Winterer, E.L., Hussong, D.M., and Decker, R.W., eds., The eastern Pacific Ocean and Hawaii: Boulder, Colorado, Geological Society of America, Geology of North America, N, p. 15–72.

Atwater, T., Stock, J.M. (1998), Pacific-North America plate tectonics of the Neogene southwestern United States: An update, *Int. Geol. Rev*., 40, 375–402.

Axen G.J. (1999), Low-angle normal fault earthquakes and triggering, *Geophysical Research Letters*, 26 (24), 3693-3696.

Axen, G. J., J. M. Fletcher (1998), Late Miocene-Pleistocene extensional faulting, northern Gulf of California, Mexico and Salton Trough, California, *Int. Geol. Rev*., 40, 217–244.

Axen, G.J., Grove, M., Stockli, D., Lovera, O. M., Rothstein, D.A., Fletcher, J.M., Farley, K., Abbott, P.L. (2000), Thermal evolution of Monte Blanco dome: Low-angle normal faulting during Gulf of California rifting and late Eocene denudation of the eastern Peninsular Ranges, *Tectonics*, 19, 197–212, doi:10.1029/1999TC001123.

Behr, W.M., Rood, D.H., Fletcher, K.E., Guzman, N., Finkel, R., Hanks, T.C., Hudnut, K.W., Kendrick, K.J., Platt, J.P., Sharp, W.D., Weldon, R.J., Yule, J.D. (2010), Uncertainties in slip-rate estimates for the Mission Creek strand of the southern San Andreas Fault at Biskra Palms Oasis, southern California, *Bull. Geol. Soc. Am*., 122, 1360-1377.

Bennet, S.K., Oskin, M.E. (2014) Oblique rifting ruptures continents: Example from the Gulf of California shear zone, *Geology*, 42, (3), 215–218, doi:10.1130/G34904.1.

Bennett, S.E.K., Oskin, M.E., Iriondo, A., (2013), Transtensional rifting in the proto-Gulf of California, near Bahía Kino, Sonora, México. *Geol. Soc. of Am. Bull.* 125, 1752–1782. http://dx.doi.org/10.1130/B30676.1.

Bennett, S.E.K., Oskin, M.E., Dorsey, R.J., Iriondo, A., Kunk, M.J., (2015), Stratigraphy and structural development of the southwest Isla Tiburón marine basin: Implications for latest Miocene tectonic opening and flooding of the northern Gulf of California, *Geosphere*, doi: 10.1130 /GES01153.1.

Bennett, S.E.K., Oskin, M.E., Iriondo, A., Kunk, M.J., (2016), Slip history of the La Cruz fault: development of a late Miocene transform in response to increased rift obliquity in the northern Gulf of California: *Tectonophysics,* http://dx.doi.org/10.1016/j.tecto.2016.06.013.

Bot, A., Geoffroy, L., Authemayou, C., Bellon, H., Graindorge, D., Pik, R., (2016), Miocene detachment faulting predating EPR propagation: Southern Baja California, Tectonics, (35), 1153-1176, doi:10.1002/2015TC004030.

Brown, R.W., Beucher, R., Roper, S., Persano, C., Stuart, F., Fitzgerald, P., (2013), Natural age dispersion arising from the analysis of broken crystals. Part I: Theoretical basis and implications for the apatite (U–Th)/He thermochronometers, *Geochimica et Cosmochimica Acta,* 122, 478-497.

Burchfiel, B.C., Cowan, D.S., Davis, G.A. (1992), Tectonic Overview of the Cordilleran Orogen in the western United States, in Burchfiel B. C., Lipman, P. W., and Zoback, M. L., eds., The Cordilleran Orogen: Conterminous U. S.: Boulder Colorado, Geological Society of America, *The Geology of North America*, G3.

Buscher, J.T., Spotila, J.A. (2007), Near-field response to transpression along the southern San Andreas fault, based on exhumation of the northern San Gabriel Mountains, southern California, *Tectonics*, 26, TC5004, doi:10.1029/2006TC002017.

Cox, B.F., Matti, J.C., King, T., Morton, D.M. (2002), Neogene strata of southern Santa Rosa Mountains, California, and their significance for tectonic evolution of the western Salton Trough, *Geol. Soc. of Am. Abst. with Prog.*, 34, no. 6, paper 57–5.

Crowell, J.C. (1982), The tectonics of Ridge Basin, southern California, in Geologic History of Ridge Basin, edited by J. C. Crowell and M. H. Link, pp. 25–42, *Pac. Sect., Soc. of Econ. Paleontol. And Mineral*., Los Angeles, Calif.

Crowell, J.C. (1981), An outline of the tectonic history of southeastern California, *in* Ernst, W.G., ed., *The geotectonic development of California; Rubey Volume I: Englewood Cliffs*, New Jersey, Prentice-Hall, p. 583–600.

Darin, M.H., Bennett, S.E.K., Dorsey, R.J., Oskin, M.E., Iriondo, A., (2016), Late Miocene extension in coastal Sonora, México: Implications for the evolution of dextral shear in the proto-Gulf of California oblique rift. *Tectonophysics,* http://dx.doi.org/10.1016/j.tecto.2016.04.038.

dePolo, C.M., Anderson, J.G., (2000), Estimating the slip rates of normal faults in the Great Basin, USA, *Basin Research*, 12, 227-240, doi: 10.1046/j.1365-2117.2000.00131.x.

Dibblee, T.W. (1984), Stratigraphy and tectonics of the San Felipe Hills, Borrego Badlands, Superstition Hills, and vicinity, *in* Rigsby, C.A., ed., *The Imperial Basin—Tectonics, sedimentation, and thermal aspects*: Los Angeles, California, Pacific Section, *Soc. of Econ. Paleontol. And Mineral*., 31–44.

Dibblee, T.W., Jr. (1954), Geology of the Imperial Valley region, California, *in* Jahns, R.H., ed., *Geology of southern California*: California Division of Mines Bulletin, 170, p. 21–28.

Dickinson, W.R., (1996), Kinematics of transrotational tectonism in the California Transverse Ranges and its contribution to cumulative slip along the San Andreas transform fault system: *Geological Society of America Special Paper* 305, 46 p., doi:10.1130/0-8137-2305-1.1.

Dodson, M.H. (1973), Closure temperature in cooling geochronological and petrological systems, Contrib. Mineral. Petrol., 40, 259–274.

Dorsey, R.J., Axen, G.J., Peryam, T.C., Kairouz, M.E. (2012), Initiation of the Southern Elsinore Fault at ~1.2 Ma: Evidence from the Fish Creek-Vallecito Basin, southern California, *Tectonics*, 31, TC2006. doi: 10.1029/2011TC003009.

Dorsey, R.J., Housen, B. A., Janecke, S.U., Fanning, C.M., Spears, A.L.F. (2011), Stratigraphic record of basin development within the San Andreas fault system: Late Cenozoic fish

Creek-Vallecito basin, Southern California. *Bull. Geol. Soc. Am*. 123, 771–793. doi:10.1130/B30168.1

Dorsey, R.J., Langenheim, V.E. (2015) Crustal-scale tilting of the central Salton block, southern California. Geosphere 11, 1365–1383. doi:10.1130/GES01167.1

Dorsey, R.J., Roering, J.J., (2006) Quaternary landscape evolution in the San Jacinto fault zone, Peninsular Ranges of Southern California: Transient response to strike-slip fault initiation. *Geomorphology,* 73, 16–32. doi: 10.1016/j.geomorphology,2005.06.013.

Dumitru, T.A., (1990), Subnormal Cenozoic Geothermal Gradients in the Extinct Sierra Nevada Magmatic Arc: Consequences of Laramide and Post-Laramide Shallow-Angle Subduction, *Journal of Geophysical Research*, 95, (B4), 4925-4941.

Ehlers, T.A., Farley, K.A. (2003), Apatite (U–Th)/He thermochronometry: methods and applications to problems in tectonic and surface processes, *Earth and Planetary Science Letters*, 206 (1–2), 1–14. doi: 10.1016/S0012-821X(02)01069-5.

Ehlig, P.L., 1981, Origin and tectonic history of the basement terrane of the San Gabriel Mountains, central Transverse Ranges, *in* Ernst, W.G., ed., *The geotectonic development of California; Rubey Volume I*: Englewood Cliffs, New Jersey, Prentice-Hall, p. 253–283.

Farley, K.A. (2000), Helium diffusion from apatite: General behavior as illustrated by Durango fluorapatite, *J. Geophys. Res*., 105, 2903-2914.

Farley, K.A., Stockli, D.F. (2002), (U-Th)/He dating of phosphates: Apatite, monazite, and xenotime, in Phosphates: Geochemical, Geobiological, and Materials Importance, *Rev. Mineral. Geochem.*, 48, edited by M.J. Kohn, J. Rakovan, and J.M. Hughes, p. 559 – 577, Mineral. Soc. of Am., Washington, D. C.

Farley, K.A., Wolf, R.A., Silver, L.T. (1996), The effects of long a-stopping Distances on (U-Th)/He ages, *Geochim. Cosmochim. Acta*, 60, 4223-4229.

Fattaruso, L. A., Cooke, M.L., Dorsey, R.J. (2014). Sensitivity of uplift patterns to dip of the San Andreas fault in the Coachella Valley, California. *Geosphere*, 10, 1235–1246, doi:10.1130/GES01050.1

Fletcher, J.M., Grove, M. Kimbrough, D. Lovera, O., Gehrels, G.E. (2007), Ridge-trench interactions and the Neogene tectonic evolution of the Magdalena shelf and southern Gulf of California: Insights from detrital zircon U-Pb ages from the Magdalena fan and adjacent areas, *Geol. Soc. Am. Bull*., 119, 1313–1336, doi:10.1130/B26067.1.

Flowers, R.M., Ketcham, R.A., Shuster, D.L., Farley, K.A., (2009), Apatite (U–Th)/He thermochronometry using a radiation damage accumulation and annealing model, *Geochim. Cosmochim. Acta,* 73 (8), 2347–2365.

Foster, D.A., Gleadow, A.J.W., Reynolds, S.J., Fitzgerald, P.G., (1993), Denudation of metamorphic core complexes and the reconstruction of the Transition Zone, west central Arizona: Constraints from apatite fission track thermochronology, *J. Geophys. Res*., 98, 2167-2185, doi:10.1029/92JB02407.

Foster, D.A., John, B.E., (1999), Quantifying tectonic exhumation in an extensional orogen with thermochronology: Examples from the southern Basin and Range Province, *In* Ring U, Brandon MT, Lister G, Willett SD (eds) Exhumation Processes: Normal Faulting, Ductile Flow, and Erosion, *Geol. Soc. London Special Publ.* 154:343-364 Geological Society, London, Special Publications, 154, 343-364.

Fuis, G.S., Scheirer, D.S., Langenheim, V.E., Kohler, M.D. (2012), A new perspective on the geometry of the San Andreas fault in southern California and its relationship to

lithospheric Structure, *Seismological Society of America Bulletin*, 102, 236–251, doi: 10.1785/0120110041.

Gallagher, K. (2012), Transdimensional inverse thermal history modeling for quantitative thermochronology. *J. Geophys. Res. Solid Earth,* 117, 1–16. doi:10.1029/2011JB008825.

Gans, P.B. (1997), Large-magnitude Oligo-Miocene extension in southern Sonora: Implications for the tectonic evolution of northwest Mexico, *Tectonics*, 16, 388–408, doi:10.1029/97TC00496.

Gastil, G., Krummenacher, D., Minch, J., (1979), The record of Cenozoic volcanism around the Gulf of California, *Geol. Soc. Am. Bull*, 90, 839-857.

Hayman, N.W., Knott, J.R., Cowan, D.S., Nemser, E., Sarna-Wojcicki, S. (2003), Quaternary low-angle slip on detachment faults in Death Valley, California, *Geology,* 31, 343-346.

Henry, C.D., Faulds, J.E., dePolo, C.M. (2007), Geometry and timing of strike-slip and normal faults in the northern Walker Lane, northwestern Nevada and northeastern California: Strain partitioning or sequential extensional and strike-slip deformation?, *in* Till, A.B., Roeske, S.M., Sample, J.C., and Foster, D.A., eds., *Exhumation Associated with Continental Strike-Slip Fault Systems*: Geological Society of America Special Paper 434, p. 59–79, doi: 10.1130/2007.2434(04).

Herbert, J.W., Cooke, M.L. (2012), Sensitivity of the Southern San Andreas fault system to tectonic boundary conditions and fault configurations: *Seismological Society of America Bulletin*, 102, 2046–2062, doi:10.1785/0120110316.

Herzig, C.T, Jacobs, D.C., (1994), Cenozoic volcanism and two-stage extension in the Salton trough, southern California and northern Baja California, Geology, 22, 991-994.

Ingersoll, R.V., Rumelhart, P.E. (1999), Three-stage evolution of the Los Angeles basin, *Southern California: Geology*, 27, 593–596, doi: 10.1130/0091-7613(1999)027<0593:TSEOTL>2.3.CO;2.

Janecke, S.U., Dorsey, R.J., Steely, A.N., Kirby, S.M., Lutz, A.T., Housen, B.A., Belgarde, B., Langenheim, V., Rittenour, T., Forand, D. (2010), High geologic slip rates since early Pleistocene initiation of the San Jacinto and San Felipe fault zones in the San Andreas fault system: Southern California, USA, *Geological Society of America Special Paper* 475, 48, doi:10.1130/9780813724751.

King, T., Cox, B.F., Matti, J.C., Powell, C.L., Osterman, L.E., and Bybell, L.M., (2002), Previously unreported outcrops of Neogene Imperial Formation in southern Santa Rosa Mountains, California, and implications for tectonic uplift: Geological Society of America Abstracts with Programs, 34, no. 6., paper 57-6.

Kirby, S.H., Janecke, S., Dorsey, R. (2007), Pleistocene Brawley and Ocotillo Formations: Evidence for initial strike-slip deformation, *J. of Geol*., 115, 43–62, doi:10.1086/509248

Kirby, S.M., Janecke, S.U., Dorsey, R.J., Housen, B.A., Langenheim, V., McDougall, K., Steely, A.N., (2007), Pleistocene Brawley and Ocotillo formations: Evidence for initial strike-slip deformation along the San Felipe and San Jacinto fault zones, southern California, Journal of Geology, 115, 43–62, doi:10.1086 /509248.

Langenheim, V.E., Jachens, R.C., Matti, J.C., Hauksson, E., Morton, D.M., Christensen, A. (2005), Geophysical evidence for wedging in the San Gorgonio Pass structural knot, southern San Andreas fault zone, southern California - marked. *Geol. Soc. Am. Bull*. 117, 1554 p., doi:10.1130/B25760.1.

Law, R.D., Ericsson, K.A., Davisson, D., (2001), Formation, evolution, and inversion of the middle Tertiary Diligencia basin, Orocopia Mountains, southern California, Geological society of America Bulletin, 2, 196-221, doi: 10.1130/0016-7606(2001)113<0196:FEAIOT>2.0.CO;2.

Lin, G. (2013), Three-dimensional seismic velocity structure and precise earthquake relocations in the Salton Trough, Southern California: *Bulletin of the Seismological Society of America*, 103, doi: 10.1785/0120120286.

Lin, G., Shearer, P.M., Hauksson, E. (2007), Applying a three-dimensional velocity model, waveform cross correlation, and cluster analysis to locate southern California seismicity from 1981 to 2005: *Journal of Geophysical Research*, 112, p. B12309, doi: 10.1029/2007JB004986.

Lindsey, E.O., Fialko, Y. (2013), Geodetic slip rates in the southern San Andreas fault system: Effects of elastic heterogeneity and fault geometry, *Journal of Geophysical Research*, 118, 689–697, doi: 10.1029/2012JB009358.

Loveless, J.P., Meade, B.J. (2011), Stress modulation on the San Andreas fault by interseismic fault system interactions, *Geology*, 39, 1035–1038, doi: 10.1130/G32215.1.

Luo, G., Liu, M. (2012), Multi-timescale mechanical coupling between the San Jacinto fault and the San Andreas fault, southern California, *Lithosphere*, 4 (3), 221–229, doi: 10.1130/L180.1.

Lutz, A.T., Dorsey, R.J., Housen, B.A., Janecke, S.U. (2006), Stratigraphic record of Pleistocene faulting and basin evolution in the Borrego Badlands, San Jacinto fault zone, Southern California, *Geol. Soc. Am. Bull.,* 118, 1377–1397. doi:10.1130/B25946.1

Mann, P. (2007), Global catalogue, classification and tectonic origins of restraining and releasing bends on active and ancient strike- slip fault systems, *in* Tectonics of Strike- Slip Restraining and Releasing Bends, edited by W. D. Cunningham and P. Mann, *Geol. Soc. Spec. Publ*., 290, 13–142.

Matti, J.C., Morton, D.M. (1993), Paleogeographic evolution of the San Andreas fault in southern California: A reconstruction based on a new cross-fault correlation, in Powell, R.E., et al., eds., The San Andreas fault system: Displacement, palinspastic reconstruction, and geologic Evolution, *Geological Society of America Memoir*, 178, 107–159, doi:10.1130/MEM178-p107.

Matti, J.C., Cox, B.F., Morton, D.M., Sharp, R.V., King, T. (2002), Fault-bounded Neogene sedimentary deposits in the Santa Rosa Mountains, southern California: Crustal stretching or transpressional uplift?, *Geological Society of America Abstracts with Programs*, 34, no. 6, paper 57-4.

Matti, J.C., Morton, D.M., Cox, B.F., Landis, G.P., Langenheim, V.E., Premo, W.R., Kistler, R., Budahn, J.R. (2006), Fault-bounded late Neogene sedimentary deposits in the Santa Rosa Mountains, southern CA: Constraints on the Evolution of the San Jacinto fault, *Eos Transactions, American Geophysical Union*, 87, no. 52, abs. T21B-0407.

Meade, B.J., Hager, B.H. (2005), Block models of crustal motion in southern California constrained by GPS measurements, *Journal of Geophysical Research*, 110, B03403, doi:10.1029/2004JB003209.

Minch, J.A. (1979), The late-Mesozoic-early Tertiary framework of continental sedimentation, northern Peninsular Ranges, Baja California, Mexico, in Eocene Depositional Systems:

San Diego, edited by P. L. Abbott, pp. 43 – 68, Pac. Sect., Soc. Of Econ. Paleontol. and Mineral., San Diego, Calif.

Nicholson, C., Sorlien, T. Atwater, J.C. Crowell, B.P. Luyendyk (1994), Microplate capture, rotation of the western Transverse Ranges, and initiation of the San Andreas transform as a low-angle fault system, *Geology*, 22, 491–495, doi: 10.1130/0091-613[1994]022<0491:MCROTW>2.3.CO;2.

Nicholson, C., Plesch, A., Shaw, J., Sorlein, C., Hauksson, E. (2013), Updating the 3D fault set for the SCEC Community Fault Model (CFM-v4) and revising its associated fault database [poster]: Southern California Earthquake Center Annual Meeting.

Numelin, T. Kirby, E., Walker, J.D., Didericksen, B. (2007), Late Pleistocene slip on a low-angle normal fault, Searles Valley, California, *Geosphere*, 3(3), 163–176.

Oskin, M., Stock, J. (2003), Pacific-North America plate motion and opening of the upper Delfin Basin, northern Gulf of California, Mexico, *Geol. Soc. Am. Bull*., 115, 1173–1190, doi:10.1130/B25154.1.

Oskin, M., Stock, J. (2003), Marine incursion synchronous with plate-boundary localization in the Gulf of California. *Geology,* 31, 23–26. doi:10.1130/0091613(2003)031<0023:MISWPB>2.0.CO;2

Oskin, M., Stock, J., Martin-Barajas, A. (2001), Rapid localization of Pacific-North America plate motion in the Gulf of California, *Geology,* 29, 459–462. doi:10.1130/0091-613(2001)029<0459:RLOPNA>2.0.CO;2.

Pacheco, M., Martín-Barajas, A., Elders, W., Espinosa-Cardena, J.M., Helenes, J., Segura, A., 2006. Stratigraphy and structure of the Altar basin of NWSonora: implications for the

history of the Colorado River delta and the Salton trough. *Rev. Mex. Cienc. Geol*., 23 (1), 22.

Powell, R.E. (1993), Balanced palinspastic reconstruction of pre-late Cenozoic paleogeology, southern California, *in* Powell, R.E., et al., eds., The San Andreas fault system: Displacement, palinspastic reconstruction, and geologic evolution: Geological Society of America Memoir 178, 1–106, doi: 10.1130/MEM178-p1.

Powell, R.E. (1981), Geology of the crystalline basement complex, eastern Transverse Ranges, southern California: constraints on regional tectonic interpretation, Dissertation (Ph.D.), California Institute of Technology, http://resolver.caltech.edu/CaltechETD:etd-07252007-135803.

Powell, R.E., Weldon, R.J., II, (1992), Evolution of the San Andreas Fault: *Annual Review of Earth and Planetary Sciences*, 20, p. 431–468, doi: 10.1146/annurev.ea.20.050192.002243.

Roeske, S.M., Till, A.B., Foster, D.A., Sample, J.C. (2007), Introduction, *in* Till, A.B., Roeske, S.M., Sample, J.C., Foster, D.A., eds., Exhumation Associated with Continental Strike-Slip Fault Systems: Geological Society of America Special Paper 434, vii-ix.

Ruisaard, C.I., (1979), Stratigraphy of the Miocene Alverson Formation, Imperial County, California [M.S. Thesis]: San Diego, California, San Diego State University, 125 p.

Seiler, C., Fletcher, J.M., Kohn, B.P., Gleadow, A.J.W., Raza, A. (2011), Low-temperature thermochronology of northern Baja California, Mexico: Decoupled slip-exhumation gradients and delayed onset of oblique rifting across the Gulf of California, *Tectonics,* 30, doi:10.1029/2009TC002649.

Seiler, C., Quigley, M.C., Fletcher, J.M., Phillips, D., Gleadow, A.J.W., Kohn, B.P., (2013), Stratigraphy and $^{40}Ar/^{39}Ar$ geochronology of the Santa Rosa basin, Baja California: dynamic evolution of a constrictional rift basin during oblique extension in the Gulf of California, *Basin Res.,* 25 (4), 388–418.

Sharp, R.V., (1967), San Jacinto fault zone in the Peninsular Ranges of southern California: *Geol. Soc. Amer. Bull*., 78, 705-730.

Sharp, R.V., (1979), Some characteristics of the eastern Peninsular Ranges mylonite zone, *in* Proceedings of Conference VIII: Analysis of Actual Fault Zones in Bedrock, edited by R. Speed, R. Sharp, and J. F. Evernden, U.S. Geol. Surv., Open File Rep., 79-1239, 258 – 267.

Shirvell, C.R., Stockli, D.F., Axen, G.J., Grove, M. (2009), Miocene–Pliocene exhumation along the west Salton detachment fault, southern California, from (U-Th)/He thermochronometry of apatite and zircon, *Tectonics*, 28, TC2006, doi:10.1029/2007TC002172.

Shuster, D.L., Flowers, R.M., Farley, K.A. (2006), The influence of natural radiation damage on helium diffusion kinetics in apatite, *Earth Planet. Sci. Lett*., 249(3–4), 148-161.

Smith-Konter, B., Sandwell, D.T., (2009), Stress evolution of the San Andreas fault system: Recurrence interval versus locking depth, *Geophysical Research Letters*, 36, L13304, doi: 10.1029/2009GL037235.

Spencer, J.E., W.R. Normark (1979), Tosco-Abreojos fault zone: A Neogene transform plate boundary within the Pacific margin of southern Baja California, Mexico, *Geology*, 7, 554 – 557, doi:10.1130/0091-7613[1979]7<554:TFZANT>2.0.CO;2.

Spotila, J.A., Berger, A.L. (2010), Exhumation at orogenic indentor corners under long-term glacial conditions: Example of the St. Elias orogen, Southern Alaska, *Tectonophysics*, 490 (3–4), 241–256, doi: 10.1016/j.tecto.2010.05.015.

Spotila, J.A., (2005), Applications of low-temperature thermochronometry to tectonic geomorphology, based on examples from transpressional and convergent settings, in Reiners, P.W., ed., Low temperature thermochronometry: Techniques, interpretations, and applications, Reviews in Mineralogy and Geochemistry, *Mineral. Soc. Amer*., 58, 449-466.

Spotila, J.A., Farley, K.A., Yule, J.D., Reiners, P., (2001), Near-field transpressive deformation along the San Andreas fault zone in southern California, based on exhumation constrained by (U-Th)/He dating, *Journal of Geophysical Research*, 106, no. b12, pages 30,909-30,922

Spotila, J.A., Sieh, K. (2000), Architecture of transpressional thrust faulting in the San Bernardino Mountains, southern California, from deformation of a deeply weathered surface, *Tectonics*, 19, 589–615, doi: 10.1029/1999TC001150.

Spotila, J.A., Farley, K.A., Sieh, K. (1998), Uplift and erosion of the San Bernardino Mountains, associated with transpression along the San Andreas fault, CA, as constrained by radiogenic helium thermochronometry, *Tectonics*, 17, 360–378.

Spotila, J.A., Niemi, N.A., Brady, R.C., House, M.A., Buscher, J.T., Oskin, M. (2007), Long-term continental deformation associated with transpressive plate motion: The San Andreas fault, *Geology*, 35, 967-970.

Steely, A.N., Janecke, S.U., Dorsey, R.J., Axen, G.J. (2009), Early Pleistocene initiation of the San Felipe fault zone, SW Salton Trough, during reorganization of the San Andreas fault system*, Geol. Soc. Am. Bull.,* 121, 663–687. doi:10.1130/B26239.1

Stock, J.M., Hodges, K.V. (1989), Pre-Pliocene extension around the Gulf of California and the transfer of Baja California to the Pacific plate, *Tectonics*, 8, 99–115, doi:10.1029/TC008i001p00099.

Stockli, D.F. (2005), Application of low-temperature thermochronometry to extensional settings, in Low- Temperature Thermochronology: Techniques, Interpretations, and Applications, edited by P. W. Reiners and T. A. Ehlers, *Rev. Mineral. Geochem*., 58, 411–448, doi:10.2138/rmg.2005.58.16.

Sylvester, A.G., Smith, R.R. (1976), Tectonic transpression and basement-controlled deformation in San Andreas fault zone, Salton Trough, California, *American Association of Petroleum Geologists Bulletin*, 60, 2081–2102.

Thatcher, W., Savage, J.C., Simpson, R.W. (2016), The Eastern California Shear Zone as the northward extension of the southern San Andreas Fault, *J. Geophys. Res. Solid Earth*, doi:10.1002/2015JB012678.

Todd, V.R., Erskine, B.G., Morton, D.M., (1988), Metamorphic and tectonic evolution of the northern Peninsular Ranges Batholith, southern California, *in* Ernst, W.G., ed., Metamorphism and crustal evolution of the western United States: Rubey Volume VII: Englewood Cliffs, New Jersey, Prentice-Hall, 894–937.

U.S. Geological Survey (and California Geological Survey), (2006), Quaternary fault and fold database for the United States, accessed November 2015, from USGS web site: http//earthquakes.usgs.gov/hazards/qfaults/.

Weldon, R.J., Meisling, K.E., Alexander, J. (1993), A speculative history of the San Andreas fault in the Transverse Ranges, California, *in* Powell, R.E., et al., eds., The San Andreas fault system: Displacement, palinspastic reconstruction, and geologic evolution. Geological Society of America Memoir, 178, 161–198, doi: 10.1130/MEM178-p161.

Winker, C.D., Kidwell, S.M. (1986), Paleocurrent evidence for lateral displacement of the Pliocene Colorado River delta by the San Andreas fault system, southeastern California, *Geology*, 14, 788–791, doi:10.1130 /0091-7613 (1986)14 <788:PEFLDO>2.0.CO;2.

Wernicke, B. (1985), Uniform-sense normal simple shear of the continental lithosphere, *Canadian Journal of Earth Sciences*, 22 (1), 108–125, 10.1139/e85-009.

Wolf, R.A., Farley, K.A., Kass, D.M. (1998), Modeling of the temperature sensitivity of the apatite (U-Th)/He thermochronometer, *Chemical Geology*, 148, 105–114, doi:10.1016/S0009541(98)00024-2.

Wolf, R.A., Farley, K.A., Silver, L.T. (1997), Assessment of (U-Th)/He thermochronometry: The low-temperature history of the San Jacinto Mountains, California, *Geology*, 25, 65 – 68.

Wolf, R.A., Farley, K.A. Silver, L.T. (1996), Helium diffusion and low-temperature thermochronometry of apatite, *Geochim. Cosmochim. Acta*, 60, 4231–4240, doi:10.1016/S0016-7037(96)00192-5.

Woodcock, N.H., Fischer, M. (1986), Strike slip duplexes, *Journal of Structural Geology,* 8, 725– 735.

Appendix 2.1

SUPPORTING INFORMATION

Contents of this file: Table S1 AHe data

Introduction

Table S2.1 “AHe data” contains location and isotopic data for samples of apatite U-Th-Sm/He thermochronometry from the Santa Rosa Mountains, Southern California, U.S.A. Sampling methods and analytical techniques discussed in detail in the main text.

TABLE S2.1: AHe data.

Sample	Elev. (m)	Lat.	Lon.	Rock type	Mass (mg)	He (pmol)	U (ppm)	Th (ppm)	Sm (ppm)	# grains	F_T	Corr. age	Avg. age (Ma)	Std dev. (Ma)	Std. dev. (%)
SRF06-1	470	33.3757	-116.23901	granitic	0.0079	0.0273	142.0	48.7	294.4	4	0.74	5.84	**6.4**	0.9	13.8
SRF06-3					0.0046	0.0146	119.2	52.3	353.2	1	0.79	5.88			
SRF06-4					0.0080	0.0262	140.9	48.4	305.9	4	0.75	5.52			
SRF06-5					0.0138	0.0477	106.8	31.0	230.6	1	0.76	7.57			
SRF06-6					0.0134	0.0535	138.9	36.5	259.2	1	0.74	6.99			
SRF07-1	527	33.3429	-116.21518	granitic	0.0201	0.0806	146.6	39.8	315.7	5	0.78	6.28	**6.5**	0.7	10.8
SRF07-2					0.0072	0.0233	127.7	41.5	349.8	3	0.74	6.02			
SRF07-3					0.0107	0.0495	140.2	34.7	285.8	5	0.77	7.77			
SRF07-4					0.0064	0.0251	162.2	41.1	325.1	5	0.69	6.36			
SRF07-5					0.0112	0.0475	171.8	28.8	290.9	5	0.73	6.22			
SRF08-1	350	33.3400	-116.21898	granitic	0.0119	0.0216	83.8	21.4	202.0	5	0.73	5.33	**5.6**	0.3	5.0
SRF08-2					0.0069	0.0159	103.9	34.6	258.1	4	0.70	5.64			
SRF08-3					0.0119	0.0268	92.7	30.5	253.5	5	0.77	5.61			
SRF08-4					0.0120	0.0244	77.8	30.5	237.9	1	0.86	5.28			
SRF08-5					0.0086	0.0157	78.8	23.8	199.8	5	0.70	5.92			
SRF09-A	455	33.3416	-116.2169	granitic	0.0068	0.0149	76.0	23.7	182.4	1	0.83	6.23	**6.0**	0.3	5.6
SRF09-B					0.0172	0.0427	97.9	26.8	210.4	3	0.78	5.86			
SRF09-C					0.0113	0.0258	103.0	14.4	212.1	4	0.73	5.57			
SRF09-D					0.0136	0.0313	88.4	19.6	194.8	4	0.76	6.28			
SRF10-A	299	33.3354	-116.2139	granitic	0.0093	0.0402	165.6	50.8	287.9	2	0.80	5.75	**5.7**	0.3	5.4
SRF10-C					0.0087	0.0292	135.6	59.6	325.5	1	0.80	5.32			
SRF10-D					0.0059	0.0380	263.1	82.3	377.4	3	0.73	5.91			
SRF11-A	270	33.3347	-116.2147	granitic	0.0201	0.0058	15.7	9.8	271.9	1	0.86	3.52	**4.0**	0.7	17.7
SRF11-B					0.0136	0.0053	19.3	0.7	224.5	2	0.8	4.5			
SRF11-C					0.0107	0.0194	19.5	2.1	254.8	1	0.8	*20.1*			

TABLE S2.1 (Continued): AHe data.

Sample	Elev. (m)	Lat.	Lon.	Rock type	Mass (mg)	He (pmol)	U (ppm)	Th (ppm)	Sm (ppm)	# grains	F_T	Corr. age	Avg. age (Ma)	Std dev. (Ma)	Std. dev. (%)
SRR-12-1	1473	33.3714	-116.2083	gneiss	0.0091	0.0036	13.4	1.0	259.5	4	0.77	7.12	**9.6**	2.2	22.4
SRR-12-2					0.0043	0.0024	13.4	1.1	277.7	5	0.70	10.90			
SRR-12-3					0.0080	0.0058	15.8	0.8	307.2	2	0.78	10.80			
SRR-12-4					0.0037	0.0276	11.8	1.9	275.3	1	0.79	*144.40*			
SRR13-A	1279	33.3609	-116.2085	gneiss	0.0303	0.0810	7.6	1.5	258.6	1	0.90	*68.26*	**7.1**	0.5	6.9
SRR13-B					0.0162	0.0040	7.1	0.9	229.0	2	0.83	7.55			
SRR13-C					0.0066	0.0048	27.6	2.7	287.7	3	0.74	6.57			
SRR13-D					0.0103	0.0145	44.2	3.9	458.4	1	0.84	7.06			
SRR-14-1	818	33.3461	-116.2139	gneiss	0.0023	0.0126	20.2	18.6	311.2	3	0.69	*61.00*	**9.8**	2.9	29.5
SRR-14-2					0.0035	0.0019	9.4	3.8	223.7	2	0.76	13.10			
SRR-14-3					0.0032	0.0010	8.7	2.4	258.1	4	0.65	9.71			
SRR-14-4					0.0035	0.0007	7.9	2.6	242.8	4	0.71	6.09			
SRR-14-5					0.0079	0.0031	8.7	1.8	271.3	2	0.78	10.10			
SRR-15-1	944	33.3454	-116.2103	gneiss	0.0094	0.0416	150.9	38.9	143.4	5	0.74	7.16	**7.3**	0.5	6.2
SRR-15-2					0.0102	0.0483	157.2	74.5	137.4	4	0.75	6.94			
SRR-15-3					0.0062	0.0483	228.8	97.6	161.2	1	0.83	7.08			
SRR-15-4					0.0047	0.0238	166.0	45.6	113.3	1	0.79	6.95			
SRR-15-5					0.0072	0.0462	205.0	63.6	183.9	5	0.70	7.96			
SRR-15-6					0.0101	0.0633	190.2	44.8	163.9	2	0.77	7.82			
ESR17-A	3	33.5682	-116.2163	granitic	0.0113	0.0241	28.3	31.8	33.5	3	0.79	14.44	**15.1**	1.2	8.0
ESR17-B					0.0098	0.0190	25.2	35.5	34.4	2	0.76	14.44			
ESR17-C					0.0083	0.0183	21.5	36.1	44.2	1	0.82	16.95			
ESR17-D					0.0053	0.0084	20.7	19.9	19.9	1	0.81	14.71			
ESR18-A	551	33.4012	-116.1714	gneiss	0.0152	0.0100	21.2	1.4	581.4	1	0.85	6.73	**6.5**	0.3	5.0
ESR18-B					0.0166	0.0128	9.5	0.5	390.0	1	0.88	*16.53*			
ESR18-C					0.0079	0.0037	5.2	0.4	479.0	1	0.81	*18.89*			
ESR18-D					0.0258	0.0085	10.9	0.4	479.0	2	0.87	6.27			

TABLE S2.1 (Continued): AHe data.

Sample	Elevation	Lat.	Lon.	Rock type	Mass (mg)	He (pmol)	U (ppm)	Th (ppm)	Sm (ppm)	# grains	F_T	Corr. age	Avg. age (Ma)	Std dev. (Ma)	Std. dev. (%)
ESR19-A	675	33.4006	-116.1767	gneiss	0.0044	0.0422	46.6	0.4	394.7	1	0.79	5.02	**4.5**	0.8	17.8
ESR19-B					0.0030	0.0273	55.3	1.0	292.7	1	0.79	3.90			
ESR19-C					0.0013	0.0058	41.7	0.7	335.2	2	0.73	*26.51*			
ESR19-D					0.0102	0.1490	100.8	3.7	426.8	3	0.79	*34.62*			
ESR21-A	900	33.3741	-116.1514	gneiss	0.0035	0.0036	18.6	0.4	98.0	1	0.71	14.50	**14.5**	0.7	5.00
ESR21-B					0.0058	0.0321	25.3	23.9	268.5	2	0.78	*43.05*			
ESR22-A	779	33.3744	-116.1485	gneiss	0.0180	0.0147	139.2	0.2	279.8	2	0.88	1.27	**1.3**	0.1	5.0
ESR22-B					0.0266	0.0414	71.7	0.3	271.4	2	0.87	*4.75*			
ESR22-C					0.0072	0.0540	144.0	2.1	283.6	1	0.89	*11.22*			
ESR22-D					0.0106	0.0121	199.3	0.6	152.0	1	0.85	1.29			
ESR23-1	908	33.3895	-116.1774	gneiss	0.0115	0.6271	234.5	412.5	277.1	5	0.75	41.94	**45.8**	5.5	12.0
ESR23-2					0.0071	0.3001	133.8	319.8	192.2	2	0.77	49.70			
ESR24-A	776	33.3929	-116.1753	gneiss	0.0036	0.0079	17.1	0.3	157.4	1	0.75	32.17	**44.9**	10.1	22.5
ESR24-B					0.0169	0.2562	74.5	0.5	217.0	2	0.82	47.34			
ESR24-C					0.0046	0.0653	59.8	0.7	197.5	1	0.79	56.59			
ESR24-D					0.0229	0.3425	75.7	0.2	229.5	2	0.87	43.40			
SRM03-A	1345	33.5673	-116.4327	granitic	0.0054	0.0105	25.3	29.6	125.6	4	0.70	*16.26*	**8.8**	0.7	7.7
SRM03-B					0.0024	0.0035	37.7	62.2	106.2	3	0.57	9.33			
SRM03-C					0.0015	0.0010	18.8	25.3	80.4	3	0.57	8.36			
SRM04-A	1414	33.5687	-116.4860	granitic	0.0101	0.2591	117.6	6.9	396.5	3	0.75	54.16	**50.8**	5.4	10.6
SRM04-B					0.0066	0.0632	52.3	2.9	265.6	3	0.72	47.97			
SRM04-C					0.0066	0.0533	39.5	1.3	262.9	1	0.81	47.48			
SRM04-D					0.0127	0.6695	211.2	19.2	534.9	2	0.80	58.53			
SRM04-E					0.0057	0.0877	90.0	4.7	347.3	3	0.70	45.76			

TABLE S2.1 (continued): AHe data.

Sample	Elevation	Lat.	Lon.	Rock type	Mass (mg)	He (pmol)	U (ppm)	Th (ppm)	Sm (ppm)	# grains	F_T	Corr. age	Avg. age (Ma)	Std dev. (Ma)	Std. dev. (%)
P2P05-A	1200	33.5842	-116.4316	granitic	0.0232	0.2647	47.3	98.6	88.8	3	0.82	37.44	**38.9**	3.5	9.1
P2P05-B					0.0224	0.2805	47.2	97.7	95.5	2	0.85	39.80			
P2P05-C					0.0190	0.2069	45.9	89.0	98.0	1	0.88	35.07			
P2P05-D					0.0146	0.2154	50.6	111.8	98.4	2	0.83	43.34			
291202-1	963	33.4952	-116.2425	granitic	0.0093	0.0361	30.4	60.9	32.0	2	0.73	21.99	**25.7**	3.3	12.9
291202-2					0.0060	0.0364	42.2	67.5	27.2	2	0.68	28.30			
291202-3					0.0043	0.0186	33.9	51.2	24.6	2	0.65	26.86			
291203-1	872	33.4952	-116.2382	granitic	0.0064	0.0327	47.7	65.2	18.7	2	0.67	22.33	**22.2**	2.92	13.1
291203-2					0.0071	0.0202	31.6	38.1	16.8	3	0.67	19.24			
291203-3					0.0039	0.0768	169.1	244.0	78.5	2	0.64	25.06			
291211-1	744	33.4952	-116.2362	granitic	0.0048	0.0057	14.3	17.9	8.8	1	0.73	16.22	**17.8**	2.4	13.5
291211-2					0.0040	0.0204	55.0	71.7	34.5	2	0.64	20.35			
291211-3					0.0046	0.0212	51.5	63.9	22.7	2	0.66	19.27			
291211-4					0.0039	0.0121	43.4	53.4	31.0	2	0.66	15.42			
291212-1	646	33.4966	-116.2240	granitic	0.0037	0.0080	41.4	49.3	25.7	3	0.58	12.96	**13.3**	1.1	8.3
291212-2					0.0032	0.0125	66.0	78.5	39.9	3	0.57	14.89			
291212-3					0.0045	0.0118	49.1	56.6	32.6	3	0.63	12.25			
291212-4					0.0018	0.0057	53.5	74.0	35.7	1	0.63	13.09			
291213-1	555	33.4948	116.2219	granitic	0.0021	0.0052	50.0	207.6	72.7	1	0.65	7.03	**9.6**	7.7	80.2
291213-2					0.0012	0.0133	131.2	225.0	44.0	1	0.61	18.16			
291213-3					0.0038	0.0033	48.0	70.5	26.5	1	0.71	3.48			
291214-1	454	33.4983	-116.2163	granitic	0.0088	0.0249	62.3	67.1	20.5	3	0.69	9.64	**13.8**	3.2	23.0
291214-2					0.0087	0.0426	76.8	83.6	25.0	3	0.69	13.58			
291214-3					0.0050	0.0302	92.4	103.9	28.0	2	0.65	14.61			
291214-4					0.0062	0.0315	63.7	65.4	25.2	2	0.69	17.30			

TABLE S2.1 (continued): AHe data.

Sample	Elevation	Lat.	Lon.	Rock type	Mass (mg)	He (pmol)	U (ppm)	Th (ppm)	Sm (ppm)	# grains	F_T	Corr. age	Avg. age (Ma)	Std dev. (Ma)	Std. dev. (%)
291221-1	360	33.4993	-116.2087	granitic	0.0056	0.0058	25.4	33.7	13.9	2	0.68	8.48	**8.9**	1.6	18.0
291221-2					0.0029	0.0076	56.7	85.2	31.0	2	0.61	10.31			
291221-3					0.0023	0.0022	22.2	27.9	17.2	2	0.60	9.98			
291221-4					0.0054	0.0055	31.3	43.2	14.1	2	0.67	6.74			
291222-1	262	33.4992	-116.2065	granitic	0.0044	0.0016	16.1	22.6	32.1	2	0.65	4.72	**5.5**	1.1	19.9
291222-2					0.0056	0.0048	36.7	51.1	60.1	3	0.63	5.13			
291222-3					0.0028	0.0024	25.1	56.3	65.0	2	0.60	6.73			
291223-1	192	33.4971	-116.2017	granitic	0.0035	0.0018	17.1	16.6	107.1	1	0.71	6.04	**6.0**	0.30	5.0
291223-2					0.0028	0.0012	19.2	11.5	65.1	2	0.62	5.73			
291223-3					0.0017	0.0006	15.4	14.4	66.2	2	0.57	6.34			

Table S2.1 AHe data: Sample information for apatite U-Th-Sm/He thermochronometry (AHe) from the Santa Rosa Mountains. Latitude and Longitude datum is WGS84. Mass based on measured Ca content. F_T = alpha ejected correction factor. Corr. age = alpha decay-corrected age. Avg. age = average of aliquots. Std dev. is deviation of the replicate analyses. Ages in red italics are excluded from averages (see text for explanation).

Chapter Three

Climate-driven unsteady denudation and sediment flux in a high-relief unglaciated catchment-fan system using ^{26}Al and ^{10}Be: Panamint Valley, California

AUTHORS

[a]*Cody C. Mason and [a]Brian W. Romans

[a]Department of Geosciences, Virginia Polytechnic Institute and State University, Blacksburg, Virginia, 24061

Corresponding Author: Cody C. Mason

Email: cmason80@vt.edu

KEYWORDS

Signal Propagation, Climate, Catchment-fan, Cosmogenic Radionuclides, Paleodenudation, Panamint Valley

HIGHLIGHTS

- Burial ages/paleodenudation rates measured in Pleistocene alluvial-lacustrine strata
- Paleodenudation variability documented in arid, high relief, unglaciated catchment
- No monotonic trend indicates ~constant rock uplift in Panamints since >1.5 Ma
- High-frequency changes suggest multi-millennial timescale climate forcing
- Transition to 100 kyr periods possibly resulted in climate-forced denudation change

ABSTRACT

Empirical models and numerical simulations of coupled erosive catchment-sediment dispersal systems make specific predictions for relationships between changing catchment boundary conditions and sediment fluxes to depositional basins. However, testing whether changes in catchment boundary conditions modulate sediment flux in natural systems over multi-millennial timescales proves challenging because of a lack of methods to quantify sediment flux from stratigraphy. Tectonic and climatic boundary conditions in the Panamint Range, California, are relatively well-constrained, and catchment-fan systems present there minimize sediment storage and recycling dynamics in the transfer zone, presenting an excellent natural laboratory to test conceptual models of climate-sedimentary dynamics. We used stratigraphic characterization and cosmogenic radionuclides (CRNs; ^{26}Al & ^{10}Be) in the Pleasant Canyon complex (PCC), a linked catchment-fan system, to examine the effects of well documented Pleistocene high magnitude (Δ temperature ~5 ºC, Δ Precipitation up to +100%, -50%), high frequency (400 & 100 kyr) climate change on denudation and sediment flux rates in an arid, high relief, unglaciated catchment. Calculated ^{26}Al/^{10}Be burial ages from 13 samples collected in an ~180 m thick stratigraphic succession range from ca. 1.55 Ma in basal strata, to ca. 0.6 – 0.3 Ma near the fan surface. The mean long term paleodenudation rate, 36 ± 8 mm/kyr (1σ), is significantly higher than the modern rate of 24 ± 0.6 mm/kyr, and paleodenudation rates demonstrate high frequency changes through stratigraphy, up to ~2x in some cases. The overall pattern of paleodenudation lacks a monotonic temporal trend, and support conclusions that (1) post mid-Pleistocene transition 100 ka periodicity modulates erosion and sediment flux rates from source to sink in this catchment-fan system and (2) rock uplift rates in the Panamint Range have remained approximately constant since >1.5 Ma. Association of the highest sediment flux rates with evidence of increased

precipitation that are represented by vertical changes from alluvial-lacustrine-alluvial fan facies in the PCC, are consistent with climate transitions driving the observed variability in catchment denudation and sediment flux.

3.1.0 INTRODUCTION

The creation and preservation of stratigraphy is the sum of complex processes that includes up-system forcings, sediment storage and recycling dynamics in the fluvial transfer zone, and changes in accommodation and internal system dynamics in depositional basins (Schumm, 1977; Paola et al., 1992; Allen, 2008a). Some geoscientists have conceptualized sediment storage and remobilization dynamics in terms of signal propagation (Castelltort and Van Den Driessche, 2003; Romans et al., 2016). In this framework, noise, signal delay, attenuation, or 'shredding' may preclude preservation or inversion of signals of up-system forcing from sedimentary basins (Jerolmack and Paola, 2010; Romans et al., 2016). Given this context, *a priori* assumptions of minimal signal attenuation, delay, or shredding are required to invert or explore effects of up-system drivers on magnitude and variability of signals of erosion-deposition dynamics. A catchment-fan system may react rapidly to changes in boundary conditions because it has a short or no transfer zone and thus represents an ideal natural laboratory for the investigation of sedimentary signal propagation (Allen, 2008b). A fundamental question then is what are the magnitudes of signals emitted from the erosive source of a catchment-fan system? And a related question is by how much do such magnitudes vary through time? Constraining sediment supply magnitude and variability allows for examination of environmental signal propagation from source to sink, and effects of sediment supply variation on stratigraphic architecture. Catchment-fan systems have previously been used to explore

effects of environmental change on sediment flux and deposition (Allen and Densmore, 2000; Armitage et al., 2013; D'Arcy et al., 2016). In such a framework, changes in catchment-scale erosion and sediment flux from catchment to fan are direct signals of environmental change.

Empirical studies of sediment flux using sediment loads in modern fluvial systems of various length scales across the globe have delineated catchment parameters and boundary conditions that exert fundamental control on sediment fluxes (Syvitski and Milliman, 2007; Milliman and Farnsworth, 2011). First-order controls on magnitudes of river sediment yields and loads are water discharge, catchment relief, and catchment area, while second-order controls are lithology, climate, and land use practices. Another major suite of studies examines cosmogenic radionuclide-derived (CRN-derived) erosion rates with respect to orogen- to catchment-scale boundary conditions. Positive correlations have been found between uplift rate, relief, and various climatic and hydrologic parameters (Densmore et al., 2009; Portenga and Bierman, 2011; Whittaker and Boulton, 2012; Covault et al., 2013; Bellin et al., 2014). These empirical data sets define a framework that might be used to make predictions regarding system response to past and future climate change. In the absence of changes in tectonics, which modifies catchment relief and/or area, or lithology and land use, changes in climate should modulate catchment denudation rates and sediment flux in system segments. However, using modern spatially distributed data sets from various climate zones to predict a response to orbital-timescale climate fluctuations is problematic because measured paleodenudation or sediment flux rates from stratigraphic archives often yield conflicting results or a lack of correlation to hypothesized controls (*e.g.* Granger and Muzikar, 2001; Stock et al., 2006; Cyr and Granger, 2008; Anthony and Granger, 2007). Global syntheses of modern CRN-derived erosion neglect multi-millennial

records of erosion and sediment flux variability, impacting the capacity to know magnitudes of possible effects due to changing boundary conditions.

Predicting catchment response to climate change on a global to individual catchment basis is challenging, because with a few exceptions there is a lack of empirical data sets that constrain high resolution and long-term (10^{3-4} yr, and 10^{6} yr, respectively) records of changes in catchment scale erosion or sediment flux (Charreau et al., 2011; Granger and Schaller, 2014; Haeuselmann et al., 2007; Schaller et al., 2002; Val et al., 2016; Oskin et al., in press). Researchers have addressed this topic by measuring CRNs in alluvial stratigraphy to derive a time series of paleodenudation rates, by utilizing volumetric estimates of basin fill, or by analyzing provenance of dated sedimentary deposits spanning climatic changes; results indicate glaciated source-to-sink systems have responded to changing climatic boundary conditions, and often within resolution of the various chronometers (Stock et al., 2005; Wolkowinsky and Granger, 2004; Glotzbach et al., 2013; Marshall et al., 2015; Gulick et al., 2015; Fildani et al., 2016; Mason et al., 2017), whereas other records show no measurable change in denudation rate or fluxes to basins across major climate transitions (Davis et al., 2012; Granger et al., 2001; Métivier and Gaudemer, 1999). For instance, in the Tibetan Plateau, denudation rates across the Plio-Pleistocene transition show a complex, asynchronous, or weak transient response to onset of glaciation, (Chareau et al., 2011; Puchol et al., 2016), while in the unglaciated Peninsular Ranges of southern California, paleodenudation rates across the Plio-Pleistocene transition remained constant (Oskin et al., in press), complicating conceptual models for catchment response to changing climate, or perhaps suggesting only glaciogenic processes significantly modify catchment erosion over Milankovitch timescales. However, the question persists as to whether

sediment flux is affected by multi-millennial timescale climate change, and if the signal can be inverted from stratigraphy.

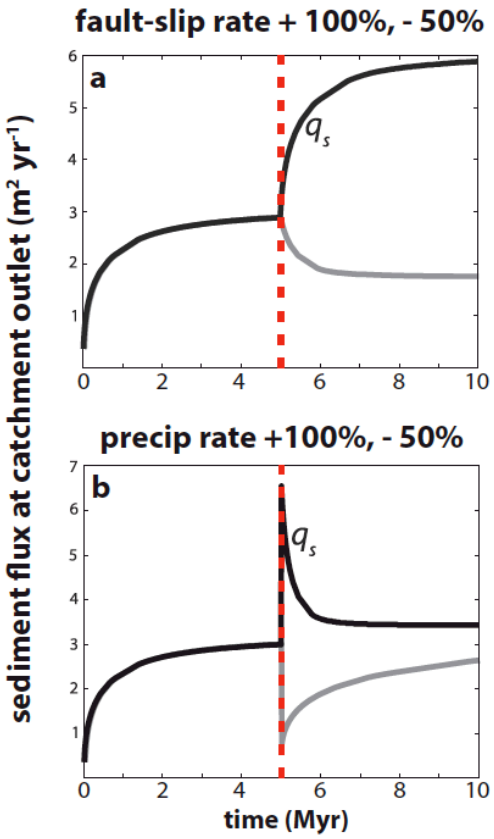

Figure 3.1: Modeled changes in sediment flux (q_s per unit width) and associated timescales resulting from perturbations in tectonic and climatic boundary conditions in a catchment-fan system bound by a range-front normal fault. **a**: q_s response to stepwise increase (+100%) or decrease (-50%) in fault slip rate. **b**: q_s response to stepwise increase (+100%) or decrease (-50%) in precipitation. Dashed vertical red line indicates timing of change in forcing. Note precipitation induces a relatively instantaneous and high magnitude response in q_s, where slip rate produces a lagged response (~10^5 – 10^6 yrs). Modified from Densmore et al. (2007).

Numerical simulations of linked catchment-fan systems represent a tool to bridge the gap between modern and geologic empirical studies. Simulations impose changes in catchment or orogen-scale boundary conditions—typically precipitation and fault-slip rate—and measure various model outputs including channel incision, catchment denudation, sediment flux at catchment outlet, and spatial distribution of grainsize variations in the depositional segment (Tucker and Slingerland, 1997; Allen and Densmore, 2000; Armitage et al., 2011). Such studies predict distinct timescales of system response and equilibrium for various forcings, with reaction times to tectonic perturbations occurring over $10^{5\text{-}6}$ yr timescales, and reactions to perturbations in precipitation occurring over 10^{3} yr timescales (Figure 3.1) (Kooi and Beaumont, 1996; Tucker and Slingerland, 1997; Allen, 2008b; Armitage et al., 2013, 2011). Models that modulate precipitation rates mimicking Milankovitch-timescale climate change result in concomitant modulation of catchment denudation and sediment flux rates (Tucker and Slingerland, 1997; Allen and Densmore, 2000; Carretier and Lucazeaut, 2005). To test the predictions of numerical models in natural systems, two fundamental conditions must be met: (1) boundary conditions should be relatively well-constrained, and (2) the system must preserve a record of changes in denudation or sediment flux and deposition through time.

In this paper, we present new data from 13 CRN samples collected throughout a 180 m thick succession of outcropping Pleistocene alluvial-lacustrine strata, and two new CRN samples collected from sediment at the modern catchment outlets, to determine the range of magnitude and variability in denudation-sediment supply rates within a single high-relief, unglaciated catchment-fan system in the Panamint Mountains, California, over the span of >1.5 Ma. The late Cenozoic tectonic history of the Panamint Mountains is well-constrained, as is the general Pleistocene climate history of the Panamint/Death Valley area. We use this empirical record of

denudation and sediment supply, as stored in the depositional segment of a linked catchment-fan, as a test of conceptual, numerical, and empirically derived predictions for the effects of multi-millennial timescale climate change on catchment-erosion/fan-deposition dynamics. In addition to addressing the above fundamental questions, the chronology from the PCC offers new constraints on the Quaternary tectonic history of specific faults in the Panamint Valley.

3.2.0 BACKGROUND

3.2.1 Pleasant Canyon Complex Source-to-sink Parameters

Panamint Range and Valley is located west of Death Valley and east of the Argus and Slate Ranges in eastern California (Figure 3.2). The Pleasant Canyon catchment, in the western Panamint Range is a high-relief catchment-fan system (~2350 meters), which drains 32.8 km^2 of the central Panamint Range. The mean catchment elevation is ~1700 m. Figure 3.3 displays catchment parameters including elevation, surface slope, and hypsometry for Pleasant Canyon catchment.

The exhumed depositional segment of the PCC (Figures 3.4 and 3.5) is composed of ~180 m of mixed alluvial and lacustrine deposits of Pleistocene age (Smith, 1976; Vogel et al., 2002). Stratigraphic surfaces in the PCC were once alluvial fan, lake bed, or playa floor, until relatively recent exhumation along a series of normal faults associated with the Panamint Valley fault zone inverted the deposit at the mouth of Pleasant Canyon (Cichanski, 2000). Small headward eroding gullies now afford excellent 3-D exposures of PCC stratigraphy, where the deposits record changing depositional environments through time.

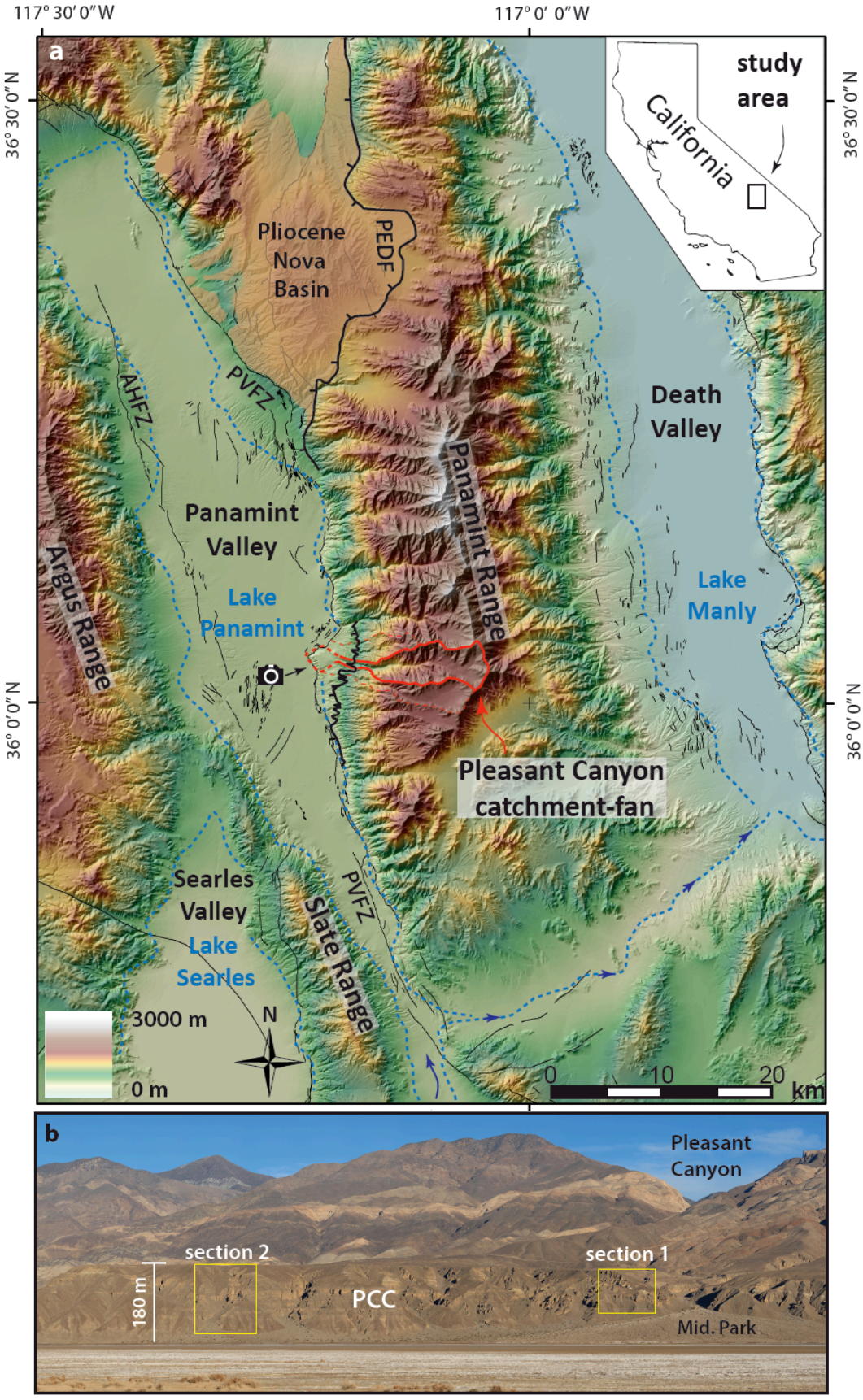
117° 30′ 0″W
117° 0′ 0″W
36° 30′ 0″N
36° 0′ 0″N
a
study area
California
Pliocene Nova Basin
PEDF
AHFZ
PVFZ
Death Valley
Panamint Range
Panamint Valley
Argus Range
Lake Panamint
Lake Manly
Pleasant Canyon catchment-fan
Searles Valley
Lake Searles
Slate Range
3000 m
0 m
N
0
10
20
km
b
Pleasant Canyon
section 2
section 1
180 m
PCC
Mid. Park

Figure 3.2: Study area shaded relief map and photopanorama of the Pleasant Canyon Complex (PCC). **a**: Topography, and active faults of the Panamint/Death Valley area. Pleasant Canyon catchment-fan system highlighted in red dashed lines. Pleistocene pluvial lakes of the Owens River system highlighted in dashed blue lines, and blue arrows denote pluvial lake flow directions into and out of Panamint Valley (Reheis et al., 2014). **B**: Photopanorama of the PCC with locations of measured sections (Photo credit: Ron Schott). AHFZ = Ash Hill fault zone, Mid. Park = Middle Park Canyon, PEDF = Panamint Emigrant detachment fault, PVFZ = Panamint Valley fault zone. Fault data from U.S. Geological Survey Quaternary fault database (https://earthquake.usgs.gov/hazards/qfaults/). Elevation data from U.S. Geological Survey (https://viewer.nationalmap.gov).

3.2.2 Late Cenozoic Tectonic History

The tectonic history of the Panamint Mountains is a first-order control on the pace of catchment denudation and sediment flux to linked alluvial fans. The Panamint Mountains are located within the eastern California-Walker Lane shear zone, a region of diffuse dextral plate boundary deformation east of the San Andreas fault, which accommodates 25 – 35% of total Pacific-North America deformation (Thatcher et al., 2016). Panamint Valley is defined by active structures displaying complex Plio-Quaternary deformation patterns; eastern Panamint Valley is bound by the low angle Panamint-Emigrant detachment system along the Panamint range front, while another set of high-angle oblique dextral faults accommodate active deformation along the Panamint Valley fault zone (See Figure 3.2; Cichanski, 2000; Andrew and Walker, 2009). Western Panamint Valley is bound by the dextral-oblique Ash Hill fault system near the foot of the Argus Range (Densmore and Anderson, 1997). Extension of the Panamint Valley may have initiated along one master detachment fault close to 12 Ma ago (Bidgoli et al., 2015). This detachment system was cut into discrete segments during a Mio-Pliocene transition to dextral

oblique deformation (Andrew and Walker, 2009). Low-temperature thermochronometry (zircon U- Th/He) from the central Panamint Range shows exhumation-related cooling initiated after ca. 12 Ma, while apatite U-Th/He samples cluster at 4 – 3 Ma, and indicate rapid Pliocene cooling and

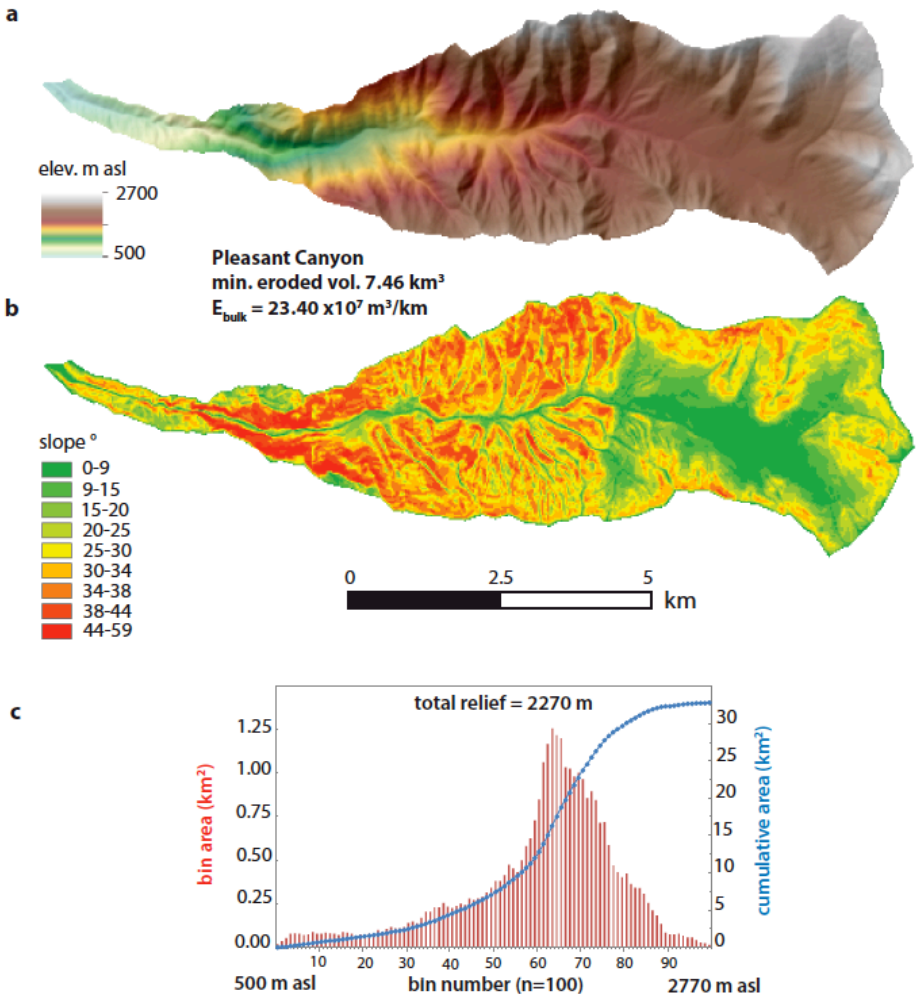

Figure 3.3: Pleasant Canyon catchment metrics. **a**: digital elevation model. **b**: Surface slope map. **c**: Pleasant Canyon catchment hypsometry. Left y-axis represents total catchment area within each bin, x-

axis represents elevation of catchment increasing from left to right (in 100 equal bins), and right y-axis is the cumulative catchment area vs. bin number.

exhumation (Bidgoli et al., 2015). Rapid sediment accumulation within the Nova Basin in northeast Panamint Valley occurred between ca. 4.4 – 3 Ma, consistent with Pliocene tectonic rejuvenation and exhumation of the Panamint Range, followed by inversion of basin depocenters (Snyder and Hodges, 2000). Rates of dip-slip motion for the Panamint Valley fault zone are ~0.35 mm/yr, and were derived using detrital zircon maximum depositional ages from basal stratigraphy of the PCC, and correlations of the prominent lacustrine interval in the upper section of the PCC to ash deposits in Death Valley thought to be Lava Creek B tuff (ca. 630 ka; Vogel et al., 2002; Jayko et al., 2008). Dextral deformation rates are debated, but are thought to be 1 – 4 mm/yr (Smith, 1976; Oswald and Wesnousky, 2002). No evidence exists for a major change in rock uplift rate or dextral translation rate along the Panamint range-front faults since ca. 4 – 3 Ma (Smith, 1976; Zhang et al., 1990; Bidgoli et al., 2014), thus catchment denudation rates should reflect equilibrium with respect to uplift of the central Panamint Range since ca. 4 – 3 Ma. Modeled erosional response timescales to changes in uplift rate support this interpretation, and equilibrium response timescales are on the order of one to three million years (Figure 3.1) (Allen and Densmore, 2000; Armitage et al., 2011; Densmore et al., 2007; Whipple and Meade, 2006). Predicted patterns in long-term denudation driven by a stepwise change in tectonics should result in monotonic increase or decrease in denudation rates during the recovery interval, and our time series of paleodenudation rates should test the hypothesis that rock uplift rates have remained constant over the timescale of the record.

3.2.3 Pleistocene Climate History

Panamint Valley is an arid endorheic basin located in a major rain shadow east of the Sierra Nevada Range. Precipitation is scarce at low elevations in Panamint Valley, but increases with elevation in a semi-logarithmic way in the Panamint range (Jayko, 2005). The Wildrose Ranger station (1250 m asl) is in the northern Panamint Range, and receives an average of 19 cm of precipitation annually (Jayko, 2005). No long-term record of precipitation exists for Pleasant Canyon, but the mean elevation of ~1700 m asl results in > 25 – 30 cm of mean annual precipitation. Observations of modern sedimentation events in Death and Panamint Valley indicates catchment hillslopes and fluvial channels transmit material to alluvial fans during low-frequency, high magnitude storm events (Hooke, 1972), so frequency of major storms, as well as longer term processes such as weathering and soil formation should influence sediment production and transfer from catchment to fan over geomorphological timescales.

The hydrology of endorheic basins east of the Sierra Nevada was influenced by global and regional climate patterns and glacial runoff from the Sierra Nevada. Pluvial lakes filled Panamint Valley multiple times during the Pleistocene (Smith, 1976) via runoff from the paleo Owens River system—a chain of pluvial lakes initiating along the eastern Sierra Nevada and flowing from Owens to Death Valley (Jannik et al., 1991; Phillips, 2008). Various episodes of late Pleistocene pluvial highstands are abundant in the geomorphic record, and include wave-cut shorelines, tufa deposits, and constructional beach or shoreline features (Smith, 1976; Jayko, 2005). These features in Panamint Valley are thought to postdate deposition of lacustrine stratigraphic intervals preserved in the PCC (Smith, 1976; Vogel et al., 2002).

Pleistocene climate in the Great Basin was on average much wetter and colder than the late Holocene interglacial. Recent work by D'Arcy et al. (2017) reviewed the climatic conditions

for the Death Valley area during the last mid-glacial to full glacial maximum; continental paleoclimate records including pollen, hydrological restorations of pluvial lakes, oxygen isotope data and mass-balance models of Pleistocene Sierra Nevada glaciers agree that temperatures during the last glacial maximum were ~5 – 6 °C colder, and precipitation was ~2x greater than during the late Holocene (D'Arcy et al., 2016, and references therein). Mid-glacial climate conditions spanned more of the Pleistocene than full glacial or interglacial, and were approximately 2 – 3 °C colder and precipitation rates were ~1.5x those of modern conditions (D'Arcy et al., 2017). D'Arcy et al. (2017) found that climatic forcing, specifically increased precipitation and water fluxes from mountainous catchments to fans during the mid-glacial resulted in measurable differences in patterns of down-system fining of alluvial sediments. The total fluxes from catchment to fan remain unresolved, but if grainsize variation tracks systematically with climate variability, so might CRN-derived estimates of sediment fluxes.

3.2.4 Previous Regional Paleodenudation Studies

The ages of alluvial fans in the Death Valley area have been used to understand rates of tectonic deformation and effects of climate on alluvial fan morphology (Machette et al., 2008). Unfortunately, few employed paleodenudation rate techniques. Frankel et al., (2007) dated faulted alluvial fans in northern Death Valley using ^{36}Cl depth profiles, and used inherited concentrations to derive paleodenudation rates of ~40 and ~80 mm/kyr for two catchment-fan systems along the western Grapevine Mountains (Big Dip and Redwall Canyon-fans, respectively) during the early last mid-glacial (ca. 70 ± 10 ka).

Late Pleistocene denudation rates for catchments in the central Panamint Mountains may be a function of mean catchment elevation and precipitation (Jayko, 2005). Alluvial fan

volumetric estimates and rough age constrains were used to quantify time averaged denudation for catchments in the western Panamint Mountains, and indicate rates between ca. 40 – 230 mm/kyr, with larger catchment-fans associated with higher denudation rates (Jayko, 2005). A time series of denudation rates from a single high-relief, unglaciated catchment within the Great Basin represents a crucial missing component to understanding variability of erosion-deposition rates during glacial-interglacial climate change over Milankovitch timescales.

3.3.0 METHODS

3.3.1 Sedimentary Lithofacies & Stratigraphic Architecture

We characterized the stratigraphy of the PCC using measured lithostratigraphic sections, and high-resolution photopanoramas for inaccessible outcrops. For our two measured sections (Figure 3.2b), stratigraphy and sedimentology were characterized at the cm to decimeter scale using a Jacob staff and hand lens. We recorded dominant grain size, bed thickness, sedimentary structures, sorting, particle roundness, clast vs. matrix support, and lateral continuity of beds. We then constructed lithofacies and lithofacies associations using sedimentary characteristics defined in measured sections that we use to interpret depositional environments.

3.3.2 Field Sampling, Laboratory Preparation, and Measurement of cosmogenic $^{26}Al/^{10}Be$

We took advantage of the linked nature of the Pleasant Canyon catchment-fan system by collecting quartz-rich sediment in a vertical succession from Pleistocene alluvium derived directly from Pleasant Canyon. Samples taken vertically through a stratigraphic succession represent a record of catchment denudation rates through time. Pleistocene sediment was

sampled within the stratigraphic framework defined during fieldwork. All samples were located within, or correlated to our measured sections (Section locations depicted in Figure 3.2b).

Our sampling strategy was designed to minimize effects of modern exposure to cosmic rays. We collected sediment from well-shielded vertical or overhanging canyon walls, mostly within narrow canyons. In each case, sediment was excavated from at least 50 cm depth horizontally into outcrops and parallel to bedding. We sieved sediment in the field and collected only the medium sand sized fraction (250 – 500 μm). A total of 15 samples were collected during this study; 13 samples were collected from outcrop, and 2 samples were collected from modern wash sediment at catchment outlets. Our goal was to quantify both paleodenudation through time and modern catchment averaged denudation rates for the feeder catchments, Pleasant Canyon, and adjacent Middle Park Canyon.

Samples of Pleistocene and modern sediment underwent standard physical separation and chemical purification procedures at the Purdue Rare Isotope Measurement Laboratory (PRIME Lab). Samples were washed and wet sieved to remove fine particles, then underwent a technique of froth-floatation to separate quartz from feldspar. Samples underwent magnetic separation and were then treated with heavy liquids to isolate quartz. Purified quartz was then leached in dilute $HF\text{-}HNO_3$ baths in an ultrasonic tank to remove the meteoric CRN components. All samples of pure quartz were screened using inductively coupled plasma optical emission spectrometry (ICP-OES). Samples of pure quartz were spiked with ^{27}Al or ^{9}Be carrier of known concentration, and dissolved using concentrated HF/HNO_3 acid. Samples were then filtered through cation and anion exchange columns, then Al and Be hydroxides were dried and converted to oxides, and loaded into targets to be measured using accelerator mass spectrometry (AMS) at the PRIME

Lab. AMS results were corrected using blank concentrations following standard PRIME Lab procedures.

3.3.3 Sediment Provenance

Sediment preserved in the PCC was mainly derived from the Pleasant Canyon catchment, as indicated by the position of deposit at the canyon mouth, the progradation direction of the PCC, a closed drainage in the upper portions of Middle Park catchment, and sediment provenance (clast compositions) in measured sections. Pleasant Canyon contains a unique geologic unit known as the World Beater complex, a foliated gneiss with well-developed augen porphyroblasts (Albee et al., 1981). The World Beater is not present in Middle Park catchment, thus the presence of World Beater clasts support a model where sediment preserved in the PCC was derived from the Pleasant Canyon. We conducted reconnaissance-level field work to survey for the presence of this unique lithology in our measured lithostratigraphic sections; clasts of World Beater were ubiquitous at all levels of strata, in float along canyons, and in outcrop (Supplementary Figure S3.1). We are confident that sediment in the PCC was derived from Pleasant Canyon, and that the use of a catchment average production rate derived from the hypsometry of Pleasant Canyon is justified. We note Middle Park catchment may have contributed minor amounts of sediment to the PCC, yet the small difference in catchment hypsometry only affects the production of CRNs to a minor degree (~1 atom/g SiO_2/yr) and thus we elect to use one catchment production rate for all outcrop samples in the PCC.

3.3.4 Cosmogenic $^{26}Al/^{10}Be$ Burial Dating and Paleodenudation Calculations

Quartz sediment eroded from a catchment and mixed in a fluvial system retains a concertation of CRNs (^{26}Al and ^{10}Be) inversely proportional to the spatially averaged denudation rate within that catchment (Lal, 1991; Granger et al, 1996; Bierman and Steig, 1996; von Blanckenburg, 2006). Rapidly eroding landscapes result in low concentrations of CRNs in fluvial sediment, while the opposite is true for slowly eroding landscapes. Sediment in catchment-fan systems is evacuated and rapidly deposited on the fan, and assuming the pre-burial concentration of CRN found in sediment is due to steady vertical advection during erosion, the concentration ($N_{Al,Be}$ in atoms/g SiO_2) is simply a function of the erosion rate (E) in cm/yr:

$$(1)\ N_{Al}(0) = \frac{A_0}{\frac{1}{\tau_{Al}} + \frac{E}{L_0}} + \frac{A_1}{\frac{1}{\tau_{Al}} + \frac{E}{L_1}} + \frac{A_2}{\frac{1}{\tau_{Al}} + \frac{E}{L_2}} + \frac{A_3}{\frac{1}{\tau_{Al}} + \frac{E}{L_3}}$$

$$(2) N_{Be}(0) = \frac{B_0}{\frac{1}{\tau_{Be}} + \frac{E}{L_0}} + \frac{B_1}{\frac{1}{\tau_{Be}} + \frac{E}{L_1}} + \frac{B_2}{\frac{1}{\tau_{Be}} + \frac{E}{L_2}} + \frac{B_3}{\frac{1}{\tau_{Be}} + \frac{E}{L_3}}$$

Where A_j and B_j are constants, with values of A_0 = 28.5, A_1 = 0.72. A_2 = 0.16, A_3 = 0.19, B_0 = 5, B_1 = 0.09, B_2 = 0.02, and B_3 = 0.02, and in units of atoms/yr/g SiO_2, (Granger and Muzikar, 2001; Borchers et al., 2016). L_j represents an attenuation length scale for CRN production reactions; L_0 refers to the attenuation length for spallogenic reactions, L_1 and L_2 are attenuation lengths for negative muon capture, and L_3 is the attenuation length for fast muon capture. We assign values of L_0 = 160/ ρ, L_1 = 738/ ρ, L_2 = 2688/ ρ, and L_3 = 4360/ ρ, where ρ represents rock density covering a sample in g/cm^3 (Granger and Muzikar, 2001). Density of overlying mass in the catchment during erosion is assumed to be 2.6 g/cm^3, and the bulk density of sediment in the PCC is assumed to be 2.2 g/cm^3.

Buried sediment derived from a steadily eroding source retains a concentration of CRNs that evolves through time as a function of the pre-burial concentration (itself a function of erosion rate), and the time since burial (Granger and Muzikar, 2001):

$$(3)\ N_{Al}(t) = N_{Al}(0)\exp\left(\frac{-t}{\tau_{Al}}\right) + P_{Al}(d)\tau_{Al}\left[1-\exp\left(\frac{-t}{\tau_{Al}}\right)\right]$$

$$(4)\ N_{Be}(t) = N_{Be}(0)\exp\left(\frac{-t}{\tau_{Be}}\right) + P_{Be}(d)\tau_{Be}\left[1-\exp\left(\frac{-t}{\tau_{Be}}\right)\right]$$

Where $N_{Al,Be}$ is the number of atoms/g SiO_2, t is time in years, $P_{al,Be}$ are production rates in atoms/yr/g SiO_2, d is sample depth in cm, and τ_{Al} and τ_{Be} represent the radioactive mean lives for ^{26}Al and ^{10}Be (Norris et al., 1983; Nishiizumi et al., 2007; Chmeleff et al., 2010). In equations three and four, the first term describes post-burial radioactive decay, and the second term describes post-burial production of CRNs. At depths greater than several 10s of m, the right hand term may be considered negligible, but post-burial production in shallowly buried sediment may be significant (Granger and Muzikar, 2001). While lacustrine environments such as pluvial lakes provide extra post-depositional shielding to sediment from cosmic rays, we use an equation with terms that describe muonogenic post-burial CRN production:

$$(5)P_{Al}(d) = A_0\exp\left(\frac{-d}{L_0}\right) + A_1\exp\left(\frac{-d}{L_1}\right) + A_2\exp\left(\frac{-d}{L_2}\right) + A_3\exp\left(\frac{-d}{L_3}\right)$$

$$(6)P_{Be}(d) = B_0\exp\left(\frac{-d}{L_0}\right) + B_1\exp\left(\frac{-d}{L_1}\right) + B_2\exp\left(\frac{-d}{L_2}\right) + B_3\exp\left(\frac{-d}{L_3}\right)$$

Where *A* and *B* are mechanisms of CRN production as given in equations one and two. Equations one through six combine to form a system of two equations and two unknowns, time (*t*) and erosion rate (*E*), and using measured CRN concentrations ($N_{Al,Be}$) and the depth of each sample (*d*), we may solve for both *t* and *E*. To recover *t* and *E*, we forward model pre-burial concentrations of CRNs, and use a least-squares optimization to determine a best fit burial age and denudation rate for each measured pair of CRN concentrations (Craddock et al., 2010). We used published sea-level high latitude reference production rates for ^{26}Al and ^{10}Be of 28.5 and 4 atoms/g SiO_2/yr, respectively (Borchers et al., 2016), and scaled them to the catchment average production rates using latitude and catchment hypsometry to correct for altitude and shielding by the horizon, resulting in catchment average production rates for ^{26}Al and ^{10}Be of 102 and 14.3 atoms/yr/g SiO_2 (Stone, 2000; and code described in Dortch et al., 2011).

3.3.5 Assumptions Associated with Burial Age and Paleodenudation Rate Calculations

To calculate the ^{26}Al/^{10}Be burial age and paleodenudation rate from sediment in the PCC we assumed the sampled bed was instantaneously buried to the modern depth below the fan surface, ~500 m asl. In reality, sediment was deposited and aggraded through accumulation of debris flows on the alluvial-fan surface and rapid subsidence of the hanging wall. A conservative estimate for the average aggradation rate in the PCC is at least ~100 – 400 m/Ma (Vogel et al., 2002). Craddock et al. (2010) calculated burial ages and denudation rates in northeastern Tibet using a depth dependent model, and again using an instantaneous emplacement model; they found calculating burial ages/denudation rates using the instantaneous emplacement model only resulted in significant bias when aggradation rates were very low, on the order of 10 m/Ma.

We assumed uniform distribution of quartz-bearing lithology in the catchment, and while most units contain quartz, there are mixed siliciclastic-carbonate units present along a portion of the range front (Noonday Dolomite and Kingston Peak Formation; Albee et al., 1981). However, the distribution of these units within Pleasant Canyon is minor, occurs at low altitude, and has a negligible effect on production rates.

We made no corrections for recent exposure to cosmic rays during exhumation, because (1) we have no way to constrain the timing and rate of headward erosion in the PCC, except that incision occurred after deposition of the youngest strata, and (2) we feel the measures taken during sampling, as outlined in section 3.2, ensure samples were well-shielded from modern exposure. Reported errors for burial ages-denudation rates were calculated using only the analytical uncertainties, and we do not include uncertainties in production rate or mean life of the CRNs (Craddock et al., 2010; Oskin et al., in press).

3.3.6 Mass Fluxes and Catchment Morphometrics

Minimum eroded volumes of catchments represent a useful check on CRN-derived mass fluxes (Covault et al., 2011; Bellin et al., 2014). If long term CRN-derived denudation/mass flux rates have been steady for millions of years, then the product of the long-term CRN-derived denudation rate and the duration since tectonic exhumation of the Panamint Range (*e.g.* since ca. 12 – 4 Ma) should yield results of similar magnitude to those from estimates of minimum eroded volume. However, a large discrepancy in total flux between techniques would support a model of unsteady long-term rates of catchment erosion and sediment supply to alluvial fans in Panamint Valley.

We calculated mass loads as the product of CRN-derived denudation rate (linear rate), the catchment area, and an average rock density of 2.6 t/m^3 (after Covault et al., 2011). To complement CRN-derived paleodenudation and mass flux estimates, we analyzed the hypsometry of Pleasant Canyon, and calculated a minimum eroded volume and bulk erosion rate (E_{bulk} = eroded volume/catchment area; after Bellin et al., 2014) to constrain volumetric-based denudation and mass flux estimates.

3.4.0 RESULTS

3.4.1 Depositional Lithofacies and Stratigraphic Architecture of the PCC

A robust three-dimensional stratigraphic framework is crucial to interpretation of CRN-derived burial age/paleodenudation rates for the PCC. We used data from measured lithostratigraphic sections to construct depositional lithofacies and facies associations for units in the PCC (after Miall, 1985; Blair and Mcpherson, 2008; Blair and McPherson, 2009). The following sections describe lithofacies associations and their interpreted facies components. Example lithofacies and lithofacies associations are pictured in Figure 3.4, and the large-scale stacking patterns of facies associations are presented in Figure 3.5.

Lithofacies of the PCC fall under one of two broad groups of depositional environments, those deposited on a subaerial alluvial fan surface termed the alluvial facies associations, or those deposited in or modified by subaqueous lacustrine environments during pluvial intervals termed the lacustrine facies association (Blair and McPherson, 2008). In addition, we use the term ‘transitional facies association’ to denote possible lacustrine influence of mainly alluvial facies, or of coarse grained deposits of unknown association but found in close proximity to lacustrine facies.

3.4.1.2 Alluvial Lithofacies Association

Alluvial fan facies are ubiquitous within the PCC, and are like those described in numerous publications (*e.g.* Blair and McPherson, 2009). In the PCC these facies are composed primarily of cobble to boulder conglomerates interbedded with sands of varying lateral continuity (Figure 3.4m, n).

Lithofacies Gm: matrix supported gravel conglomerate

Lithofacies Gm is found throughout the PCC in continuous to laterally discontinuous beds of 10 cm to >1-3 m thickness. Gm matrix is brown to greyish green, sand to silt sized grains, with pebble to cobble to boulder sized angular to subangular clasts. Lithofacies Gm usually lacks internal structure, but may contain faint organization. Facies Gm is interpreted to be the product of pseudoplastic, unconfined to channelized mud supported debris flows.

Lithofacies Gc: clast supported gravel conglomerate

Lithofacies Gc is found throughout the PCC, and is often laterally continuous to discontinuous over 1s to 10s of meters, can be <10 cm to >3 m in thickness, is composed of angular and subangular pebble to boulder cobbles, with interstitial sand and silt sized grains. Clast may be imbricated with evidence for bedload traction structures and faint stratification. Matrix in Gc is typically fine to coarse sand with little mud present. Lithofacies Gc is interpreted to be water-lain debris flow deposits, reworked debris flow material, or sieve deposits. Gc pictured in Figure 3.4m.

Lithofacies Sg: Granule-pebble rich Sand

Lithofacies Sg occurs in the transition from fine grained units to conglomerate alluvium in section one in the south PCC. Granule to pebble rich coarse to medium sand in beds 10 cm – >1 m thick are faintly laminated or contain low angle cross stratification. Traction structures indicate a water-lain origin, either subaerial or subaqueous deposition, while the association of these facies to fine-grained facies (discussed below) indicates a possible shallow lacustrine origin. Facies Sg pictured in Figure 3.4a.

Lithofacies Sh: horizontally laminated or featureless sand

Lithofacies Sh is found throughout the PCC in laterally continuous to discontinuous beds ranging from 1 cm up to 3 m thickness. Laminations of very fine to medium upper sand may be graded, or display load structures and deformation along bed contacts. Faintly bedded to featureless sand may exist in association with laminated beds. Lithofacies Sh is interpreted to represent unconfined sheetwash deposits in distal alluvial environment, possible waning stage subaerial dilute sediment flows, or subaqueous sandy turbidity currents in the case of stacked normally graded beds displaying contorted beds, or dewatering structures. Lithofacies Sh is pictures in Figure 3.4a, d, and h.

3.4.1.3 Transitional Lithofacies Association

A transitional lithofacies association, is defined by lithofacies present in both alluvial and lacustrine associations. In the PCC we observe fine and coarse-grained lithofacies interbedded, and in close proximity to typical alluvial fan and lacustrine facies. Where fine-grained units interpreted as lacustrine (F, Sl) are interbedded with sands (Sl, Sg), and coarse-grained gravel

conglomerates (Gc, Gm), we interpret a shallow ephemeral lake or rapidly fluctuating environment of deposition. Examples of the Transitional Lithofacies Association are pictured in Figure 3.4a, b, and at the upper 1/3 of Figure 3.4k, and i.

3.4.1.4 Lacustrine Lithofacies Association

The Lacustrine lithofacies association is defined by finely laminated to featureless beds of fine silt to clay, and in section one, several meters of rhythmically bedded sandy turbidites. Lithofacies Sh, F, and Sg are the most common facies in the lacustrine association, and are pictured in Figure 3.4d – j.

Lithofacies F: Fine silt to clay

Lithofacies F crops out in laterally-continuous (km to 100s m) deposits across the PCC, specifically in section two at ~115 – 119 m, and in section one at ~19 – 28 m above the base of sections. Lithofacies F contains CaCO3 and reacts to HCl, is white or greyish green or yellow in color, and composed of very fine sand, silt and clay sized grains. sparse disarticulated ostracod or gastropod(?) fossils are observed in thin section. Bedforms include mm to cm scale horizontal, wavy, and crinkly lamination, minor ripple cross laminations, and reddish siderite filled root traces or burrows. Facies F is often interbedded with Gm, and grades into Sf, Sl, and Gc, Gm up section. Lithofacies F is interpreted to represent a shallow to deep lacustrine environment. The complexity of preserved bedforms and dominant grainsize argues against deposition in a fluvial or alluvial environment. Facies F might best be described as a lacustrine marl.

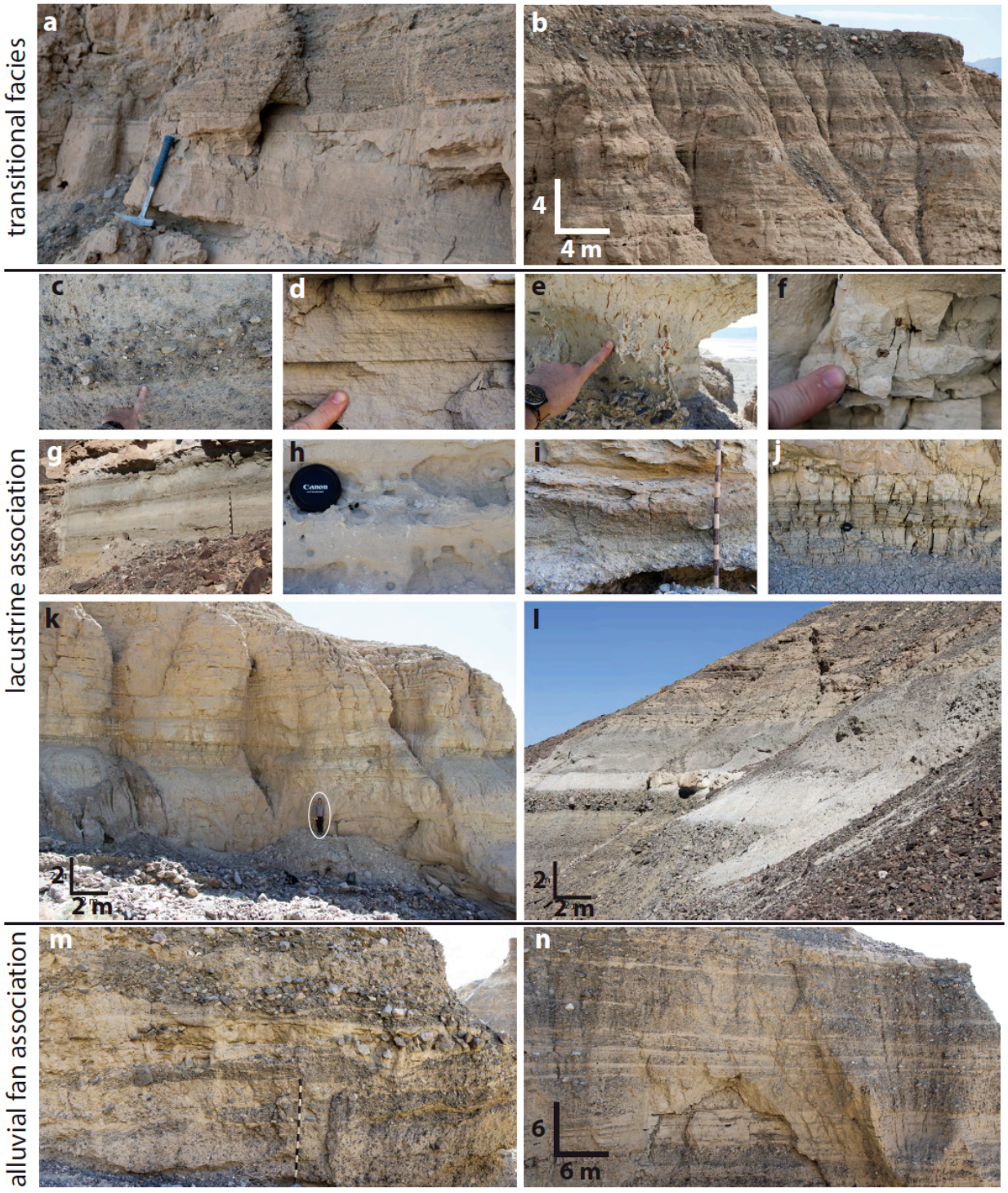

Figure 3.4: Lithofacies of the Pleasant Canyon complex**. a**, **b**: Horizontally laminated and low angle cross stratified sand and granule to pebble rich beds (Facies Sl, Sg) that compose the gradational transition in lithofacies from lacustrine association to alluvial association. Note thick gravel debris flow capping units

in **b** (facies Gc, Gm). **c** – **l**: dominantly fine-grained silt and clay (facies F, Sl, Sg) that composes the lacustrine facies association. **c**: Pebble-granule rich sand facies (Sg). **d**: Laminated sand facies (Sl). **e**, **f**: Fine grained and pebble-granule rich facies (Sf, Sg, and F), with small burrows or root-traces. **g**: interbedded fine grained and granule rich facies (F, Sg). **h**: Sandy turbidites with contorted bedding (Sl). **i**: Laminated to cross laminated sand with weakly developed paleosol (Sl). **j**: fine grained lacustrine facies (F) with possible varves. **k**: Thick exposure (note person for scale) of fine-grained facies (F, Sl) composing the lacustrine association in section one. **l**: Interbedded fine grained and gravel facies (F, Gm, Gc) that compose the lacustrine to transitional association in section two. **m**, **n**: Interbedded clast- and matrix-supported debris flow gravels with lenticular to laterally continuous sands (facies Gc, Gm, Sl, Sf) typical of the alluvial fan association.

Lithofacies Gcr: rounded clast supported gravel conglomerate

Lithofacies Gcr is found at only one location, in the base of section one (southern PCC; Figure 3.5). Gcr has the same sedimentary characteristics as Gc, with the crucial difference of abundant subrounded to rounded pebble to cobble clasts and little matrix, or loose coarse grained sand and granule matrix. We interpret facies Gcr as wave reworked beach gravel deposits. Modern gravels near catchment outlets are typically angular with little rounding of clasts.

3.4.2 Stratigraphic Architecture and Correlation

Figure 3.5 shows two views of the PCC with interpreted lithofacies associations and large scale stratigraphic stacking patterns. Lacustrine lithofacies associations represent the only units that we correlated across the PCC (~2 km). Figure 3.6 Shows interpreted correlations between measured sections one and two. We interpret the upper interval of lacustrine facies association in

the two sections to correlate across the exposure area, with section one containing a significantly expanded thickness of the lacustrine facies association.

3.4.3 Depositional Evolution of the PCC

Here we use our scheme of facies associations, and large-scale stratigraphic architecture to describe the overall depositional history. The PCC is dominantly composed of poorly-sorted polymictic gravels (lithofacies Gc, Gm), with interbedded sand and fine-grained intervals (lithofacies Sl, F). Basal deposits of the PCC indicate early depositional environments were dominated by coarse grained, muddy debris flows, most likely on an alluvial fan surface, separated by laterally discontinuous and patchy lacustrine-influenced conglomerate (transitional facies Gcr, Gc), as evidenced by clast rounding, open framework, and relatively coarse matrix content. Above the debris flow dominated alluvial fan association, the sedimentological record shows a significant episode of system flooding, deepening, and backstepping of coarse grained facies (between ~115 – 120 m in section two, between ~19 – 30 m in section one). The lacustrine facies association (facies F, Sl) signals the greatest water depth relative to all other facies. Overlying the lacustrine facies association, we interpret a transitional facies association, where thin sands, granule to pebbly sands, and muddy alluvial sediments prograde across, and grade laterally in the dip direction into lacustrine facies. The transitional facies association of distal alluvial facies (Sl, Sg) grades vertically into coarsening upward bundles of sand, pebble, and cobble to boulder conglomerate (Sl, Sg, Gm, Gc). This evolution is likely in response to changes in base level associated with lake desiccation. In the north wall of Middle Park Canyon, the upper lacustrine unit is offset by a syndepositional normal fault displaying approximately 3 – 4

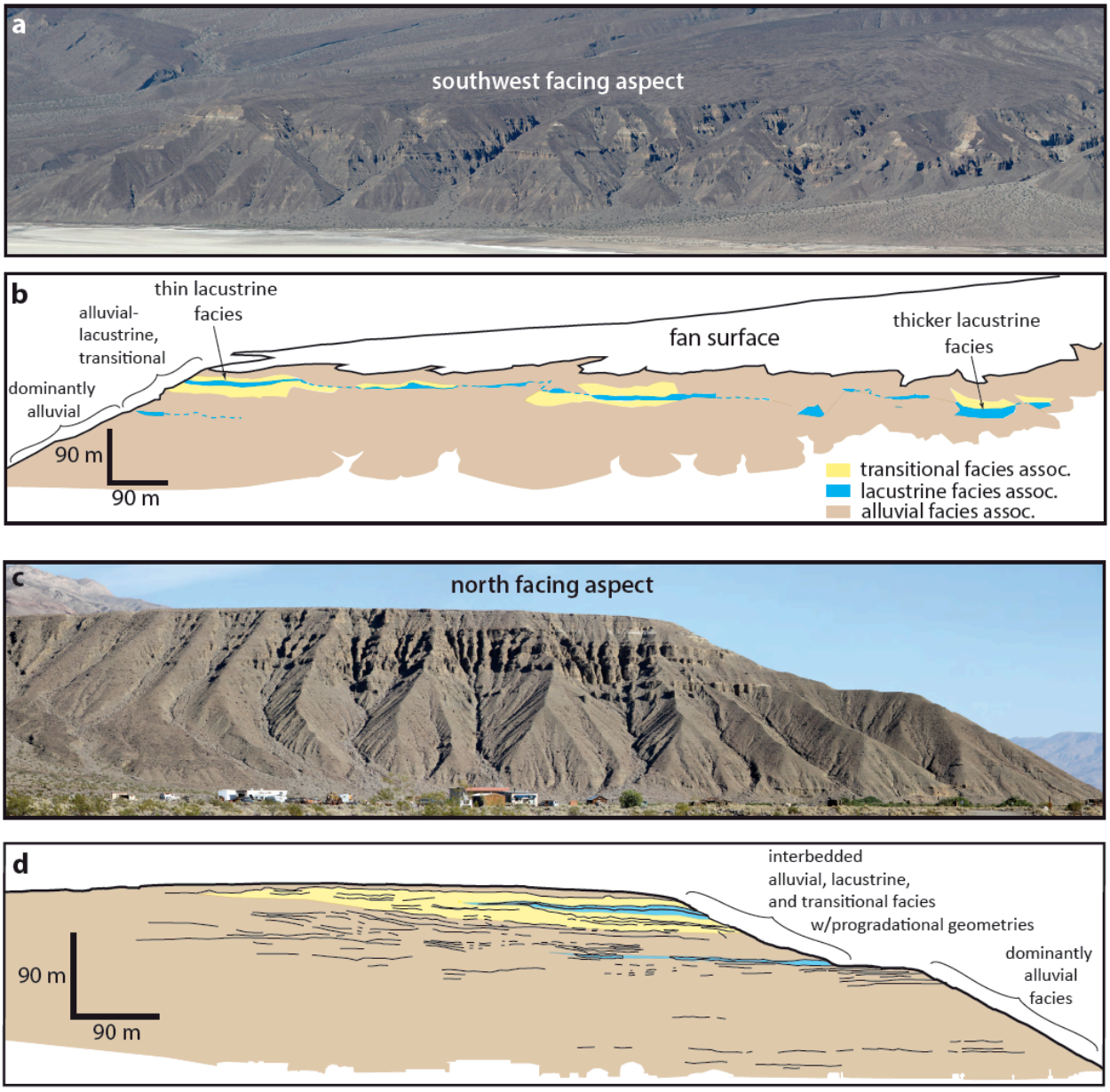

Figure 3.5: Photomosaics and large scale facies associations and stratigraphic architecture of the Pleasant Canyon Complex (PCC). **a:** Uninterpreted photomosaic of the southwest PCC. **b**: interpreted photomosaic with colored facies associations. **c**: Uninterpreted photomosaic of the northwest PCC with the ghost town of Ballarat in the foreground. **d**: Interpreted panel illustrating subtle inclined geometries of progradational foresets within alluvial-lacustrine facies. Lacustrine units pinch-out or grade into transitional or alluvial facies up dip.

meters of displacement (west side down; See supplementary Figure S3.2). The lacustrine unit thickens in the hanging wall, and paleo-fault-scarp topography was healed by subsequent deposition of lacustrine and transitional facies. Normal faulting may explain the overall thickening, and lower stratigraphic position of the lacustrine unit in section one compared to section 2. However, the change in elevation of the base of the fine-grained unit between section two in the north and section one in the south is also likely related to subtle depositional geometry of the paleo-fan surface, and related compensational stacking of fan lobes.

3.4.4 CRN-derived Stratigraphic Ages and Paleodenudation Rates

Table 3.1 displays results of AMS measurements, $^{26}Al/^{10}Be$ burial ages, and paleodenudation rates for samples from the PCC and modern catchment outlets. The results of burial dating in the PCC yield a depositional age model that supports previous interpretations for the age of basal stratigraphy of at least ca. 0.9 Ma (ca. 20 m above playa floor; Vogel et al., 2002). However, our results indicate that the deposit was actively aggrading in a proximal to medial alluvial fan environment as early as ca. 1.55 ± 0.16 Ma (Figure 3.6). Basal burial ages of ca. 1.55 ± 0.156 Ma, and 1.16 ± 0.20 Ma obey stratigraphic superposition, and samples young up-section overall. Stratigraphically-highest $^{26}Al/^{10}Be$ burial ages are ca. 0.52 ± 0.18 Ma, 0.36 ± 0.16 Ma, 0.33 ± 0.14 Ma, and 0.65 ± 0.22 Ma (Figure 3.6).

Samples of modern sediment from Pleasant Canyon and Middle Park Canyon outlets yield denudation rates of 24 ± 0.6 mm/kyr and 28 ± 1.6 mm/kyr, respectively, averaged over ca. 25 – 21 kyr timescales. Paleodenudation rates derived from PCC outcrop samples demonstrate variability, and range from 28 ± 5 mm/kyr up to 54 ± 7.5 mm/kyr, with a long term mean denudation rate for the PCC of 36 ± 8 mm/kyr (1σ for all PCC CRN-derived denudation rates).

Table 3.1: AMS results, ^{26}Al and ^{10}Be burial ages and denudation rates for samples from the Pleasant Canyon Complex and modern catchment outlets, Panamint Range and Valley, USA

sample location information						AMS Results				Burial ages and denudation rates			
sample ID	lat.	lon.	elevation (m asl)	depth (cm)	location	^{26}Al (a/g SiO_2)	error	^{10}Be (a/g SiO_2)	error	Al/Be burial age (yr)	error (yr)	denudation rate (mm/kyr)	error (mm/kyr)
PAN01	36.02861	-117.21487	430	7000	PCC	1309759	43805	252927	6311	705,000	124,500	28	5
PAN02	36.0293	-117.21377	466	3400	PCC	1564624	55644	263806	9493	425,000	158,000	31	7
PAN03	36.0293	-117.21377	466	3400	PCC	1564426	77465	262072	7548	410,000	173,500	31	3.5
PAN04	36.02942	-117.21354	476	2400	PCC	1103834	40630	177904	5627	359,000	159,500	49	5
PAN05	36.0295	-117.21344	481	1900	PCC	1214501	48460	209390	6973	518,000	177,500	39	4
PAN06	36.02905	-117.21461	435	6500	PCC	1258579	64415	218528	7525	486,000	184,000	36	4.5
PAN07	36.03671	-117.21848	482	1800	PCC	1600021	59776	256047	6211	326,000	143,500	34	3
PAN08	36.03579	-117.21942	452	4800	PCC	1046392	51235	195296	5617	654,000	170,500	37	4.5
PAN09	36.03536	-117.22203	366	13400	PCC	671949	33194	160023	7205	1,164,000	201,500	34	5
PAN10	36.04724	-117.21092	412	…	Pleasant Canyon	2225616	77950	362733	8772	…	…	24	0.56
PAN11	36.03868	-117.2192	482	1800	PCC	1341444	57291	245223	11679	645,000	219,500	31	4.5
PAN12	36.02749	-117.21577	390	…	Middle Park	1637336	65025	287452	16818	…	…	28	1.6
PAN13	36.03493	-117.21848	448	5200	PCC	755308	29065	137675	6190	618,000	184,000	54	7.5
PAN14	36.02861	-117.21487	430	7000	PCC	1210537	60013	215151	8287	536,000	188,500	36	5
PAN15	36.04103	-117.22286	336	16400	PCC	471472	20247	134163	4084	1,549,000	156,000	34	4

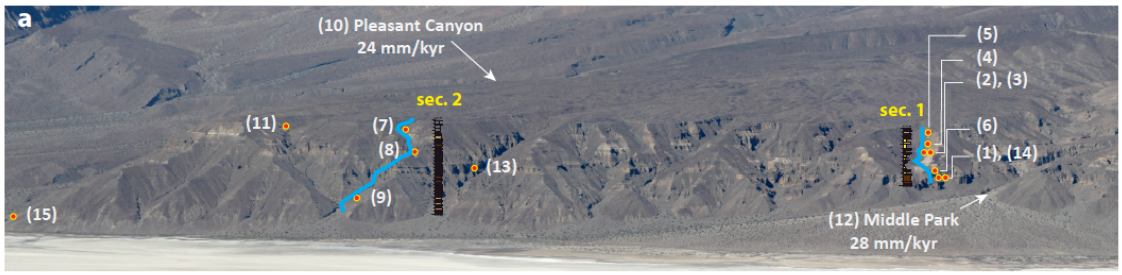
a
(10) Pleasant Canyon
24 mm/kyr
sec. 2
sec. 1
(11)
(7)
(8)
(13)
(9)
(15)
(5)
(4)
(2), (3)
(6)
(1), (14)
(12) Middle Park
28 mm/kyr

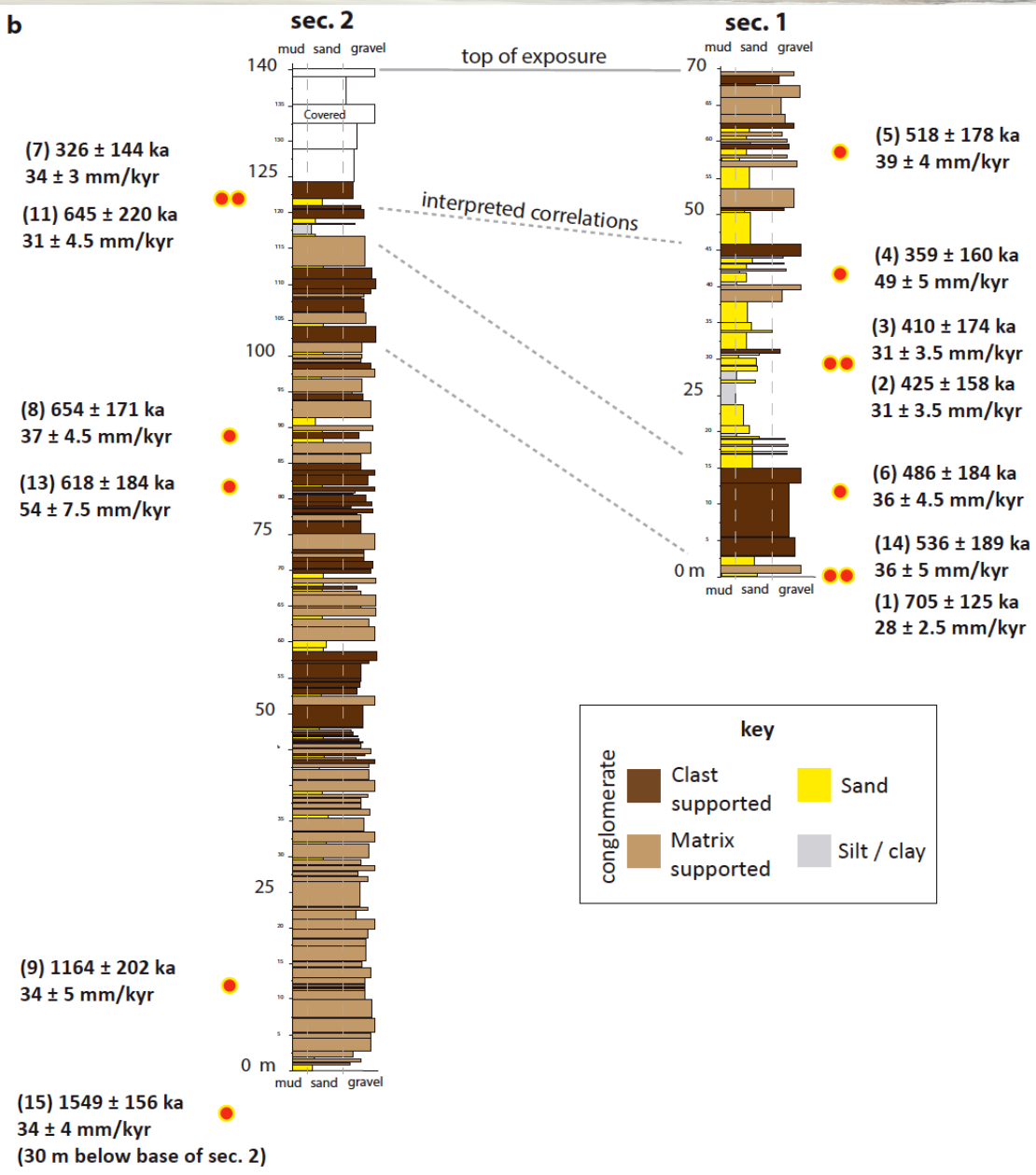
b
sec. 2
sec. 1
mud sand gravel
top of exposure
Covered
interpreted correlations
140
125
100
75
50
25
0 m
70
50
25
0 m
(7) 326 ± 144 ka
34 ± 3 mm/kyr
(11) 645 ± 220 ka
31 ± 4.5 mm/kyr
(8) 654 ± 171 ka
37 ± 4.5 mm/kyr
(13) 618 ± 184 ka
54 ± 7.5 mm/kyr
(9) 1164 ± 202 ka
34 ± 5 mm/kyr
(15) 1549 ± 156 ka
34 ± 4 mm/kyr
(30 m below base of sec. 2)
(5) 518 ± 178 ka
39 ± 4 mm/kyr
(4) 359 ± 160 ka
49 ± 5 mm/kyr
(3) 410 ± 174 ka
31 ± 3.5 mm/kyr
(2) 425 ± 158 ka
31 ± 3.5 mm/kyr
(6) 486 ± 184 ka
36 ± 4.5 mm/kyr
(14) 536 ± 189 ka
36 ± 5 mm/kyr
(1) 705 ± 125 ka
28 ± 2.5 mm/kyr
key
conglomerate
Clast supported
Matrix supported
Sand
Silt / clay

Figure 3.6: Lithostratigraphy and cosmogenic radionuclide (CRN) sample location within the Pleasant Canyon complex (PCC). **a**: Photomosaic of outcrops of the PCC with CRN sample locations marked with red filled circles and associated text with sample numbers. White arrows denote samples taken from catchment outlets and modern CRN-derived denudation rates. **b**: Simplified lithostratigraphic sections one and two from the PCC with CRN results placed within stratigraphy.

Qualitatively, denudation rates fall into one of three groups/domains based upon rate magnitudes and uncertainties (Figure 3.7). The low rate group includes the modern catchment samples and one outcrop sample (n=2 samples; each <30 mm/kyr). Several samples compose an intermediate group, with uncertainties that overlap neither the lowest nor highest rate groups (n = 6 samples; ~30 – 40 mm/kyr). And finally, a small number of samples compose the highest rate group (n = 2; 49 – 54 mm/kyr), which overlap one another, but none of the other samples from the PCC.

The highest measured rates, 54 mm/kyr is a >2x increase over the modern, and lowest rate of 24 mm/kyr for Pleasant Canyon. However, only three samples have rates that fall outside an envelope defined by the mean and standard deviation of all samples. Several samples do have errors that do not overlap, but are within this envelope, thus our results appear to show that periods of enhanced or very low catchment denudation and sediment supply occur, but may be infrequent, at least as defined by 13 paleodenudation rates within the ~180 meters of PCC stratigraphy, and one sample from the modern Pleasant Canyon catchment outlet. We note that the highest magnitudes of paleodenudation rates are observed in samples below and above the lacustrine interval (Figure 3.6).

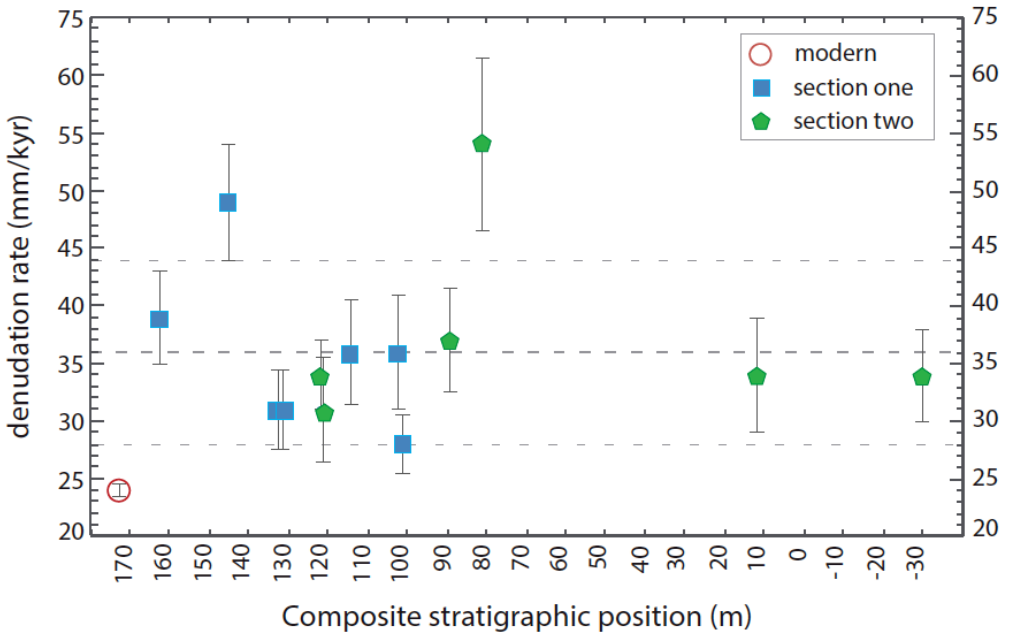

Figure 3.7: Plot of cosmogenic radionuclide-derived denudation rate vs. composite stratigraphic depth. Denudation rates for samples of sediment from the modern catchment outlet plotted at 5 m depth. Dark grey dashed line is the mean of all CRN-derived denudation rates, while light grey dashed lines are the 1σ standard deviation of sample variance. Individual sample error bars represent the average of upper and lower bounds (1σ) on burial age-erosion rate calculations (after Craddock et al., 2010).

We can confidently say the PCC was a relatively long-lived depocenter (>1 Ma), receiving sediment from the Pleasant Canyon catchment. It is unclear whether an apparent pattern of age reversals may indicate recycling of material during a late phase of alluvial fan degradation-aggradation, possibly through reworking of older sediment during a lacustrine transgression. It is also clear that initiation, or westward migration of high-angle faulting along the PVFZ occurred after ca. 0.65 – 0.33 Ma, exhuming the once valley floor.

Relatively large uncertainties for burial ages, and the fact that several samples appear out of stratigraphic order precludes correlation of deposit intervals to specific glacial or interglacial periods. However, the sedimentology of the PCC does record the depositional paleoenvironment

in terms of subaerial or subaqueous fan (Figure 3.5), and thus we have the ability to correlate measured rates to paleoclimate during the time of deposition, assuming glacial times typically lead to pluvial lakes in Panamint Valley (Smith, 1976; Phillips, 2008).

3.4.5 Volumetric-based Mass Flux Estimates

The long-term mean CRN-derived volumetric flux for the PCC is ~109 x10^7 m^3/yr, and is significantly less than estimates of volumetric flux using the minimum eroded volume of the Pleasant Canyon catchment (7.46 km^3; Figure 3.3), if averaged over ca. 4 Ma, or the last interpreted phase of tectonic exhumation (Bidgoli et al., 2015). However, the mean CRN-derived volumetric rate equals the minimum eroded volume if averaged over ca. 6.7 Ma, or several million years after the interpreted initiation of late Miocene extension-driven exhumation of the Panamint Range between ca. 12 – 9 Ma (Bidgoli et al., 2015). Interestingly, the highest CRN-derived volumetric flux rate would allow the erosion of Pleasant Canyon within ca. 4.3 Ma, though given our record of paleodenudation since 1.5 Ma, it seems unlikely that denudation-sediment flux rates were frequently higher than the mean rate of ~36 ± 8 mm/kyr over the timescale of our study.

The volumetric comparisons have several possible implications including: (1) the Pleasant Canyon catchment has eroded since ca. 6.7 Ma, possibly constraining the timing of recent tectonic exhumation, or (2) temporal unsteadiness in catchment denudation and sediment flux to the Panamint Valley before our record contributed to erosion of the catchment (*e.g.* since ca. 4 Ma), or (3) that mass wasting events not constrained by measurements of CRNs in medium sand contributed to excavation of the catchment volume (Yanites et al., 2009). Thus, perhaps one more important implication from comparing volumetric rates to eroded volumes, might be that

CRN-derived rates should be viewed as minimum estimates for long-term erosion (>10^6 yrs) in response to tectonic exhumation.

3.5.0 DISCUSSION

3.5.1 Climate-driven Variability in Catchment-fan System Response

Our primary objective was to test the effects of changing climate on the magnitudes and temporal variability of catchment denudation and sediment flux in a natural catchment-fan system. We documented the stratigraphic evolution of the PCC and used CRN-derived paleodenudation rates as a proxy for catchment-fan sediment fluxes through time. Figure 3.8 shows a synthesis of our data including a composite stratigraphic section and CRN-derived ages/paleodenudation rates against the global $\delta^{18}O$ curve.

CRN-derived paleodenudation rates for the PCC are not constant through time; the long-term denudation rate of 36 ± 8 mm/kyr, representing a span of time between ca. 1.5 and 0.33 Ma include a paleodenudation rate of 24 mm/kyr from the modern Pleasant Canyon catchment outlet, and rates of 49 and 54 mm/kyr. These three measurements fall outside an envelope defined by the mean and standard deviation of the sample variance, and several other samples have errors that do not overlap samples, but which do fall within the envelope (Figure 3.7). These data suggest that denudation and sediment supply have varied by as much as a factor of ~2x numerous times between 1.5 Ma to present.

Paleoclimate reconstructions for the region show ~1.5 – 2x increases in precipitation during the last mid and full glacial, respectively (D'Arcy et al., 2017). Empirical and numerical models indicate changes in precipitation and temperature influence rates of erosion and sediment

flux (Allen and Densmore, 2000; Syvitski and Milliman, 2007), thus a likely driver for variability in rates of denudation is multi-millennial timescale climate change.

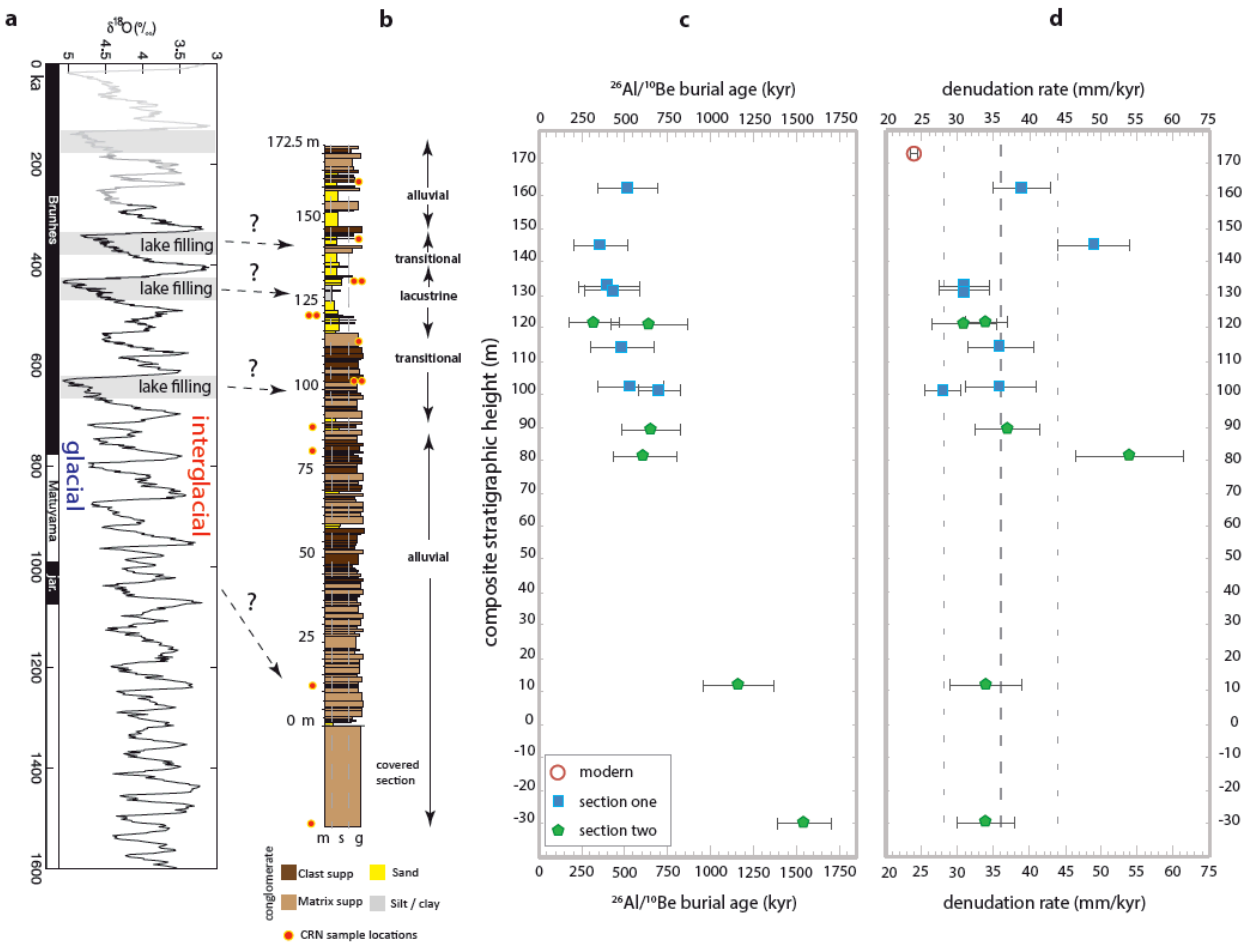

Figure 3.8: Pleistocene paleoclimate, Pleasant Canyon complex (PCC) stratigraphic framework, and paleodenudation rates for the PCC since ca. 1.5 Ma. **a**: Oxygen isotope curve of Lisieki and Raymo, (2005), with known Pluvial lake events in Panamint Valley after Jannick et al. (1991). **b**: Composite stratigraphic section with interpreted facies associations and cosmogenic radionuclide (CRN) sample positions. **c**: Cosmogenic radionuclide-derived paleodenudation rates vs. stratigraphic depth, since ca. 1.5 Ma. Modern catchment averaged rates plotted at 5 meters depth. Refer to Figure 3.6 for schematic explanation of composite stratigraphic depth.

Denudation and sediment supply rates may not have been sustained at the relatively high levels indicated by the highest rates; the two samples of elevated catchment denudation (Table 3.1; samples 4 & 13) may be anomalous with respect to the mean catchment denudation rate over geological timescales. It is plausible that: (1) these two samples represent short-lived intervals, as suggested by their erosion timescales of ca. 11.4 – 12.5 kyr, and that (2) due to the resolution of our study, the sample distribution did not capture other high or low denudation/sediment-supply intervals from the record. However, our integrated stratigraphic framework and the presence of a significant interval of lacustrine facies suggests denudation rate and sediment supply were variable some time before and after a major lake highstand, a time of increased local precipitation and glacial run off from non-local sources (Jannik et al., 1991; Phillips, 2008).

Punctuated changes in sediment supply apparent in our record hints at higher-resolution climatic fluctuations (*e.g.* glacial-interglacial timescales). We interpret the erosion (supply) and depositional (accommodation) response of facies to be related to the same shift in climate regime, namely a shift from dry to wetter climate that led to both increased precipitation and lake development in Panamint Valley. Others have noted that erosion and associated sediment production in catchments appear to increase during changes in long term precipitation patterns (e.g., transition from wet-to-dry or transition from dry-to-wet) and is less variable during stable climates, whether dry or wet (Dorn, 2009, and references therein).

Constant paleodenudation across the Plio-Pleistocene transition from catchments in the Eastern Peninsular Range, California, indicates climate cooling and increased variability did not affect paleodenudation rates there (Oskin et al., in press). Post middle-Pleistocene transition paleodenudation rates from Fisher Valley, Utah, between ca. 0.7 – 0.6 Ma, varied by as much as >2x, and are up to 2x higher than the modern catchment averaged denudation rates (Balco and

Stone, 2005). Our study documents variability in paleodenudation rates across, and after the middle Pleistocene transition, a time when Milankovitch periodicity shifted from ca. 40 to 100 kyr. Thus, a viable interpretation of our data, and that of other similar studies is that 100 kyr periods may be more efficient than 40 kyr periods at modulating catchment scale denudation.

Warmer temperatures increase chemical weathering and denudation rates, but periglacial processes may also increase physical weathering through enhanced frost cracking during wetter/colder periods (Marshall et al., 2015). During the early Pleistocene, the duration of full glacial maxima were shorter by ca. 10 – 15 kyr (Figure 3.8). Then during the middle and late Pleistocene, full maxima corresponding to the coldest/wettest periods of climate would have lasted longer, up to ca. 30 – 35 kyr; long enough for the erosion of two CRN attenuation length scales in the case of rates >50 mm/kyr for the PCC, thus potentially resulting in a new dynamic equilibrium of CRN and mass fluxes.

We make no claim to interpret glacial-interglacial cyclicity from our data set (*e.g.* Balco and Stone, 2005), but 100 kyr periods of climate change represent the most plausible driver of change in source-to-sink sediment fluxes in this high-relief, unglaciated catchment-fan system at the observed timescale. Patterns of periodicity may be observable in other locations within the Great Basin of North America, and other arid, high-relief, unglaciated landscapes worldwide, as shown for tectonically quiescent, low relief, unglaciated landscapes (Hidy et al., 2014).

3.5.2 Implications for Pleistocene Tectonics of Panamint Valley

Our CRN data set allows us to examine both the erosional response to long-term rock uplift rates in the Panamint Range and shorter timescale fault-slip-rates on Quaternary faults in Panamint Valley. Changes in denudation rate appear to occur at high frequency relative to

proposed tectonic timescales (Figure 3.1), and support an interpretation that tectonic uplift of the Panamint Range has not changed significantly since at least ca. 1.5 Ma. Nevertheless, the chronology for strata of the PCC may have value to constraints of paleoseismicity and slip rates along this segment of PVFZ. The youngest, highest ages for samples, ca. 0.52 – 0.36 Ma, and the difference in elevation between the sampled strata in the upper fan and the basin floor (~164 m) yield an average vertical slip rate between 0.3 – 0.8 mm/yr for this element of the PVFZ (Figure 3.2). The large range of slip rates is due to high uncertainties in burial ages, but overlaps published estimates (Vogel et al., 2002). Active normal faulting during deposition of the laterally continuous lacustrine facies association south of measured section one (Supplementary Figure S3.2) can be temporally constrained by $^{26}Al/^{10}Be$ burial ages that bracket the stratigraphic unit; we find offset of ~3 – 5 m occurred between ca. 486 ± 184 ka and ca. 410 ± 174 ka. The fault scarp may be a composite feature, or the product of a single rupture; the difference between the two scenarios may have implications for regional seismic hazards. For instance, a fault scarp of 3 m from a single event may indicate an earthquake magnitude of up to 6.5 – 7.2 for (Zhang et al., 1990).

An interesting aspect of this data set is its potential implications for the kinematic evolution from low-angle to high-angle faulting, and its role in subsidence of the Panamint sedimentary basin. Aggradation of alluvium in the PCC occurred between ca. 1.5 and at least ca. 0.6 – 0.3 Ma along a low-angle range front fault (Cichanski, 2000). We argue that it is unlikely the deposit could aggrade and remain preserved in the stratigraphic record without accommodation created by active slip along the low-angle range-bounding fault system and active subsidence in the hanging wall. Our depositional synthesis demonstrates a tectonostratigraphic evolution of subsidence of a hanging wall, likely driven by slip on the

Panamint-Emigrant detachment system between ca. 1.5 – 0.6 or 0.3 Ma, then an abrupt westward stepping (or resumption) of high-angle faulting after ca. 0.6 – 0.3 Ma, which inverted strata in the PCC—the new footwall of this segment of the Panamint Valley fault zone.

3.5.3 Implications to Stratigraphic Concepts

Understanding the drivers of observable patterns in stratigraphy remains a foundational motivation of inquiry in sedimentary geoscience and has wide-ranging implications to both basic and applied geoscience (Romans et al., 2016). Concepts developed early in sedimentary geology have led to the distillation of two fundamental controls: the space available for sediment accumulation (accommodation) in a depositional basin, and the supply of sediment to that basin (Barrell, 1917; Wheeler, 1958). Conceptual and simplified numerical models have investigated the variable relationship of accommodation and supply (*e.g.* A/S ratio; Swift and Thorne, 1991) in an effort to explain patterns of basin filling observed around the world and through geologic time (Paola, 2000). The magnitude of accommodation from preserved stratigraphy can be estimated for depositional systems wherein base level is coincident with sea or lake level (Holbrook et al., 2006), for progradational clinoform systems (Steckler et al., 1999; Hubbard et al., 2010) and, at larger and longer-term scales, with basin subsidence (Allen and Allen, 2013). However, the estimation of magnitude of sediment supply from stratigraphy has been problematic. Several methods of estimation have been employed, including volumetric mass-balance (*e.g.* Covault et al., 2011), scaling relationships for stratigraphically preserved geomorphic bodies (*e.g.* Bhattacharya et al., 2016), and source-area exhumation rates from detrital mineral analysis (*e.g.* Painter et al., 2014). Additionally, studies of modern sedimentary systems have discussed the role of sediment supply on stratigraphic development (*e.g.* Goodbred

and Kuehl, 2000) and have noted relationships between system morphometrics and sediment flux (*e.g.* Sømme et al., 2009). However, these methods are indirect estimates and commonly consider products with timescales longer than the scale of stratigraphy that records the influence of climate fluctuations. Thus, the quantification of sediment flux through time presented here provides a rare opportunity to investigate the relationship of sediment supply to stratigraphic patterns.

Our study of the PCC since ca. 1.5 Ma, shows that since the middle Pleistocene transition, signals of sediment supply exiting this unglaciated, high-relief catchment varied by a factor of ~2x over multi-millennial timescales. One possible implication of this work is that arid internally drained basin stratigraphy may preserve patterns of Milankovitch timescale cyclicity in physical sedimentology or CRN concentrations that is not strictly driven by base level changes or autogenic dynamics (*e.g.* lake fill-desiccation cycles, or fan lobe avulsions). Resolvable patterns in signals of higher sediment flux to basins with respect to Milankovitch climate may be recoverable from sedimentary archives, but chronologic resolution remains an issue in terrestrial stratigraphy. In Panamint Valley, deep lake formation associated with glacial maxima and arguably higher sediment flux rates was seen to accompany a system backstepping, rather than an aggressive progradation of a coarse gravel front as seen in modeling studies (Armitage et al, 2011; Figure 3.2b). A complicating factor in scaling up our results to the global scale is the potential lag time between increased sediment supply from catchment to fan, and subsequent transport to basin center, or to rivers linked to coasts. Considering these challenges, future research might focus on application of this technique to short and steep terrestrial to marine systems using sediment cores with robust age control.

An apparent imbalance between catchment minimum eroded volume and CRN-derived catchment denudation is intriguing, and show there is opportunity for future work to understand aspects of post-tectonic landscape evolution in arid regions using paleodenudation time series. Specifically, the relationship between tectonic exhumation, erosion, stochastic sedimentation events, climate change, and long term patterns of catchment to fan sediment flux may be explored using aspects of the methods presented herein.

CONCLUSIONS

We measured cosmogenic radionuclides (CRNs; ^{26}Al and ^{10}Be; n=13 samples) vertically through a succession of Pleistocene alluvium, and in modern sediment from catchment outlets (n= 2 samples), in a linked catchment-fan system to examine the effects of climate change on catchment denudation (erosion) rates and source-to-sink sediment transfer over the last ca. 1.5 Ma. The resultant paleodenudation rates from the Pleasant Canyon complex (PCC) have a mean rate of 36 ± 8 mm/kyr (1σ), and can be sorted into roughly three groups corresponding to low, medium, and high paleodenudation rates, based on rate magnitude and uncertainties. The lack of observed monotonic increase or decrease in paleodenudation rates supports a hypothesis that rock uplift rates in the central Panamint Range have remained constant over the period of record (>1.5 Ma). Pleistocene climate in the Panamint Valley region was on average 1.5 – 2x wetter than the current interglacial. While sample age resolution prevents us from delineating specific relationships between denudation magnitude and Milankovitch cyclicity, the highest recorded rates, ~49 and 54 mm/kyr, are >2x higher than the modern catchment denudation rate of ~24 mm/kyr, and occur in close stratigraphic association with the transition in PCC lithofacies associations from alluvial fan to lacustrine and from lacustrine to alluvial fan facies. Thus, the

apparent high frequency changes in paleodenudation rates from the PCC are consistent with a climate driver. The middle Pleistocene transition associated with a change from 40 to 100 kyr periods, may provide the duration necessary for steep, arid unglaciated catchment-fan systems to reach a new dynamic equilibrium with respect to sediment and CRN fluxes and climatic boundary conditions.

ACKNOWLEDGEMENTS

Financial support was provided by an American Chemical Society-Petroleum Research Fund-Doctoral New Investigator grant (#53553-DNI8) to BWR with additional analytical support from a seed grant from the Purdue Rare Isotope Measurement Laboratory (PRIME Lab) to CM and BWR. We wish to acknowledge William Craddock and Andrew Cyr for constructive conversations and insightful feedback. CM acknowledges Neal Auchter and Theodore Them for assistance in the field, and others from the Virginia Tech Sedimentary Systems Research Group for constructive feedback. Ron Schott photographed the Pleasant Canyon complex in beautiful detail. Gigapans may be found at: http://www.gigageology.org/Collections/PanamintValley.html

REFERENCES

Allen, P.A., 2008a. From landscapes into geological history. Nature 451. doi:10.1038/nature06586

Allen, P.A., 2008b. Time scales of tectonic landscapes and their sediment routing systems. Geol. Soc. London, Spec. Publ. 296, 7–28. doi:10.1144/SP296.2

Allen, P.A., Densmore, A.L., 2000. Sediment flux from an uplifting fault block. Basin Res. 12, 367–380. doi:10.1046/j.1365-2117.2000.00135.x

Andrew, J.E., Walker, J.D., 2009. Reconstructing late Cenozoic deformation in central Panamint Valley, California: Evolution of slip partitioning in the Walker Lane. Geosphere 5, 172–198. doi:10.1130/GES00178.1

Anthony, D.M., and G., D.E., 2007. A new chronology for the age of Appalachian erosional surfaces determined by cosmogenic nuclides in cave sediments. Earth Surf. Process. Landforms 32, 874–887. doi:10.1002/esp

Armitage, J.J., Duller, R. a., Whittaker, A.C., Allen, P. a., 2011. Transformation of tectonic and climatic signals from source to sedimentary archive. Nat. Geosci. 4, 231–235. doi:10.1038/ngeo1087

Armitage, J.J., Dunkley Jones, T., Duller, R.A., Whittaker, A.C., Allen, P.A., 2013. Temporal buffering of climate-driven sediment flux cycles by transient catchment response. Earth Planet. Sci. Lett. 369–370, 200–210. doi:10.1016/j.epsl.2013.03.020

Barrell, J., 1917. Rhythms and the Measurements of Geologic Time. Geol. Soc. Am. Bull. 28, 745–904.

Bellin, N., Vanacker, V., Kubik, P.W., 2014. Denudation rates and tectonic geomorphology of the Spanish Betic Cordillera. Earth Planet. Sci. Lett. 390, 19–30. doi:10.1016/j.epsl.2013.12.045

Bhattacharya, J.P., Copeland, P., Lawton, T.F., Holbrook, J., 2016. Estimation of source area, river paleo-discharge, paleoslope, and sediment budgets of linked deep-time depositional systems and implications for hydrocarbon potential. Earth-Science Rev. 153, 77–110. doi:10.1016/j.earscirev.2015.10.013

Bidgoli, T.S., Amir, E., Walker, J.D., Stockli, D.F., Andrew, J.E., Caskey, S.J., 2015. Low-temperature thermochronology of the Black and Panamint mountains, Death Valley,

California: Implications for geodynamic controls on Cenozoic intraplate strain. Lithosphere 7, 473–480. doi:10.1130/L406.1

Bierman, P., Steig, E.J., 1996. Estimating Rates of Denudation Using Cosmogenic Isotope Abundances in Sediment. Earth Surf. Process. Landforms 21, 125–139. doi:10.1002/(SICI)1096-9837(199602)21:2<125::AID-ESP511>3.0.CO;2-8

Blair, T.C., Mcpherson, J.G., 2008. Quaternary sedimentology of the Rose Creek fan delta, Walker Lake, Nevada, USA, and implications to fan-delta facies models. Sedimentology 55, 579–615. doi:10.1111/j.1365-3091.2007.00913.x

Blair, T.C., McPherson, J.G., 2009. Processes and forms of alluvial fans, Geomorphology of Desert Environments. doi:10.1007/978-1-4020-5719-9_14

Borchers, B., Marrero, S., Balco, G., Caffee, M., Goehring, B., Lifton, N., Nishiizumi, K., Phillips, F., Schaefer, J., Stone, J., 2016. Geological calibration of spallation production rates in the CRONUS-Earth project. Quat. Geochronol. 31, 188–198. doi:10.1016/j.quageo.2015.01.009

Carretier, S., Lucazeaut, F., 2005. How does alluvial sedimentation at range fronts modify the erosional dynamics of mountain catchments? Basin Res. 17, 361–381. doi:10.1111/j.1365-2117.2005.00270.x

Castelltort, S., Van Den Driessche, J., 2003. How plausible are high-frequency sediment supply-driven cycles in the stratigraphic record? Sediment. Geol. 157, 3–13. doi:10.1016/S0037-0738(03)00066-6

Charreau, J., Blard, P.-H., Puchol, N., Avouac, J.-P., Lallier-Vergès, E., Bourlès, D., Braucher, R., Gallaud, a., Finkel, R., Jolivet, M., Chen, Y., Roy, P., 2011. Paleo-erosion rates in

Central Asia since 9Ma: A transient increase at the onset of Quaternary glaciations? Earth Planet. Sci. Lett. 304, 85–92. doi:10.1016/j.epsl.2011.01.018

Chmeleff, J., von Blanckenburg, F., Kossert, K., Jakob, D., 2010. Determination of the 10Be half-life by multicollector ICP-MS and liquid scintillation counting. Nucl. Instruments Methods Phys. Res. Sect. B Beam Interact. with Mater. Atoms 268, 192–199. doi:10.1016/j.nimb.2009.09.012

Cichanski, M., 2000. Low-angle, range-flank faults in the Panamint, Inyo, and Slate ranges, California: Implications for recent tectonics of the Death Valley region. Bull. Geol. Soc. Am. 112, 871–883. doi:10.1130/0016-7606(2000)112<871:LRFITP>2.0.CO;2

Covault, J.A., Romans, B.W., Graham, S.A., Fildani, A., Hilley, G.E., 2011. Terrestrial source to deep-sea sink sediment budgets at high and low sea levels: Insights from tectonically active Southern California. Geology 39, 619–622. doi:10.1130/G31801.1

Covault, J. a., Craddock, W.H., Romans, B.W., Fildani, a., Gosai, M., 2013. Spatial and Temporal Variations in Landscape Evolution: Historic and Longer-Term Sediment Flux through Global Catchments. J. Geol. 121, 35–56. doi:10.1086/668680

Craddock, W., Kirby, E., Zhang, H., 2011. Late Miocene–Pliocene range growth in the interior of the northeastern Tibetan Plateau. Lithosphere 3, 420–438. doi:10.1130/L159.1

Craddock, W.H., Kirby, E., Harkins, N.W., Zhang, H., Shi, X., Liu, J., 2010. Rapid fluvial incision along the Yellow River during headward basin integration. Nat. Geosci. 3, 209–213. doi:10.1038/ngeo777

Cyr, A.J., Granger, D.E., 2008. Dynamic equilibrium among erosion, river incision, and coastal uplift in the northern and central Apennines, Italy. Geology 36, 103–106. doi:10.1130/G24003A.1

D'Arcy, M., Whittaker, A.C., Roda-Boluda, D.C., 2016. Measuring alluvial fan sensitivity to past climate changes using a self-similarity approach to grain-size fining, Death Valley, California. Int. Assoc. Sedimentol. Spec. Publ. doi:10.1111/sed.12308

Davis, M., Matmon, a., Rood, D.H., Avnaim-Katav, S., 2012. Constant cosmogenic nuclide concentrations in sand supplied from the Nile River over the past 2.5 m.y. Geology 40, 359–362. doi:10.1130/G32574.1

Densmore, A.L., Anderson, R.S., 1997. Tectonic geomorphology of the Ash Hill fault, Panamint Valley, California. Basin Res. 9, 53–63. doi:10.1046/j.1365-2117.1997.00028.x

Densmore, A.L., Gupta, S., Allen, P. a., Dawers, N.H., 2007. Transient landscapes at fault tips. J. Geophys. Res. 112, F03S08. doi:10.1029/2006JF000560

Densmore, a. L., Hetzel, R., Ivy-Ochs, S., Krugh, W.C., Dawers, N., Kubik, P., 2009. Spatial variations in catchment-averaged denudation rates from normal fault footwalls. Geology 37, 1139–1142. doi:10.1130/G30164A.1

Dorn, R.I., 2009. The Role of Climatic Change in Alluvial FanDevelopment, in: Parson, A.D. and Abrahams, A.D. (Ed.), Geomorphology of Desert Environments. Springer Science+Business Media B.V., pp. 1–831. doi:10.1007/978-1-4020-5719-9

Dortch, J.M., Owen, L.A., Schoenbohm, L.M., Caffee, M.W., 2011. Asymmetrical erosion and morphological development of the central Ladakh Range, northern India. Geomorphology 135, 167–180. doi:10.1016/j.geomorph.2011.08.014

Fildani, A., McKay, M.P., Stockli, D., Clark, J., Dykstra, M.L., Stockli, L., Hessler, A.M., 2016. The ancestral Mississippi drainage archived in the late Wisconsin Mississippi deep-sea fan. Geology 44, 479–482. doi:10.1130/G37657.1

Frankel, K.L., Brantley, K.S., Dolan, J.F., Finkel, R.C., Klinger, R.E., Knott, J.R., Machette, M.N., Owen, L.A., Phillips, F.M., Slate, J.L., Wernicke, B.P., 2007. Cosmogenic 10Be and 36Cl geochronology of offset alluvial fans along the northern Death Valley fault zone: Implications for transient strain in the eastern California shear zone. J. Geophys. Res. Solid Earth 112, 1–18. doi:10.1029/2006JB004350

Glotzbach, C., Van Der Beek, P., Carcaillet, J., Delunel, R., 2013. Deciphering the driving forces of erosion rates on millennial to million-year timescales in glacially impacted landscapes: An example from the Western Alps. J. Geophys. Res. Earth Surf. 118, 1491–1515. doi:10.1002/jgrf.20107

Goodbred, S.L., Kuehl, S. a., 2000. The significance of large sediment supply, active tectonism, and eustasy on margin sequence development: Late Quaternary stratigraphy and evolution of the Ganges-Brahmaputra delta. Sediment. Geol. 133, 227–248. doi:10.1016/S0037-0738(00)00041-5

Granger, D.E., 2006. A review of burial dating methods using 26 Al and 10 Be. Geol. Soc. Am. Spec. Pap. 415, 1–16. doi:10.1130/2006.2415(01).

Granger, D.E., Fabel, D., Palmer, A.N., 2001. Pliocene - Pleistocene incision of the Green River, Kentucky, determined from radioactive decay of cosmogenic 26Al and10Be in Mammoth Cave sediments. Bull. Geol. Soc. Am. 113, 825–836. doi:10.1130/0016-7606(2001)113<0825:PPIOTG>2.0.CO;2

Granger, D.E., Kirchner, J.W., Finkel, R., 1996. Spatially Averaged Long-Term Erosion Rates Measured from in Situ-Produced Cosmogenic Nuclides in Alluvial Sediment Author (s): Darryl E . Granger , James W . Kirchner and Robert Finkel Published by : The University of Chicago Press Stable URL : http://w 104, 249–257.

Granger, D.E., Muzikar, P.F., 2001. Dating sediment burial with in situ-produced cosmogenic nuclides: Theory, techniques, and limitations. Earth Planet. Sci. Lett. 188, 269–281. doi:10.1016/S0012-821X(01)00309-0

Granger, D.E., Schaller, M., 2014. Cosmogenic Nuclides and Erosion at the Watershed Scale. Elements 10, 369–373. doi:10.2113/gselements.10.5.369

Gulick, S.P.S., Jaeger, J.M., Mix, A.C., Asahi, H., Bahlburg, H., Belanger, C.L., Berbel, G.B.B., Childress, L., Cowan, E., Drab, L., Forwick, M., Fukumura, A., Ge, S., Gupta, S., Kioka, A., Konno, S., LeVay, L.J., März, C., Matsuzaki, K.M., McClymont, E.L., Moy, C., Müller, J., Nakamura, A., Ojima, T., Ribeiro, F.R., Ridgway, K.D., Romero, O.E., Slagle, A.L., Stoner, J.S., St-Onge, G., Suto, I., Walczak, M.D., Worthington, L.L., Bailey, I., Enkelmann, E., Reece, R., Swartz, J.M., 2015. Mid-Pleistocene climate transition drives net mass loss from rapidly uplifting St. Elias Mountains, Alaska. Proc. Natl. Acad. Sci. 1–6. doi:10.1073/pnas.1512549112

Haeuselmann, P., Granger, D.E., Jeannin, P.Y., Lauritzen, S.E., 2007. Abrupt glacial valley incision at 0.8 Ma dated from cave deposits in Switzerland. Geology 35, 143–146. doi:10.1130/G23094A

Hidy, A.J., Gosse, J.C., Blum, M.D., Gibling, M.R., 2014. Glacial–interglacial variation in denudation rates from interior Texas, USA, established with cosmogenic nuclides. Earth Planet. Sci. Lett. 390, 209–221. doi:10.1016/j.epsl.2014.01.011

Holbrook, J., Scott, R.W., Oboh-Ikuenobe, F.E., 2006. Base-Level Buffers and Buttresses: A Model for Upstream Versus Downstream Control on Fluvial Geometry and Architecture Within Sequences. J. Sediment. Res. 76, 162–174. doi:10.2110/jsr.2005.10

Hubbard, S.M., Fildani, a., Romans, B.W., Covault, J. a., McHargue, T.R., 2010. High-Relief Slope Clinoform Development: Insights from Outcrop, Magallanes Basin, Chile. J. Sediment. Res. 80, 357–375. doi:10.2110/jsr.2010.042

Jannik, N.O., Phillips, F.M., Smith, G.I., Elmore, D., 1991. A 36Cl chronology of lacustrine sedimentation in the Pleistocene Owens River system. Geol. Soc. Am. Bull. 103, 1146–1159. doi:10.1130/0016-7606(1991)103<1146:ACCOLS>2.3.CO;2

Jayko, A.S., 2005. Late Quaternary denudation, Death and Panamint Valleys, eastern California. Earth-Science Rev. 73, 271–289. doi:10.1016/j.earscirev.2005.04.009

Jayko, A.S., Forester, R.M., Kaufman, D.S., Phillips, F.M., Yount, J.C., McGeehin, J., Mahan, S.A., 2008. Late Pleistocene lakes and wetlands, Panamint Valley, Inyo County, California. Geol. Soc. Am. Spec. Pap. 439, 151–184. doi:10.1130/2008.2439(07)

Jerolmack, D.J., Paola, C., 2010. Shredding of environmental signals by sediment transport. Geophys. Res. Lett. 37, 1–5. doi:10.1029/2010GL044638

Kooi, H., Beaumont, C., 1996. Large-scale geomorphology: Classical concepts reconciled and integrated with contemporary ideas via a surface processes model. J. Geophys. Res. 101, 3361–3386. doi:10.1029/95JB01861

Lal, D., 1991. Cosmic ray labeling of erosion surfaces: in situ nuclide production rates and erosion models. Earth Planet. Sci. Lett. 104, 424–439. doi:10.1016/0012-821X(91)90220-C

Machette, M.N., Slate, J.L., Phillips, F.M., 2008. Terrestrial Cosmogenic-Nuclide Dating of Alluvial Fans in Death Valley, California. US Geol. Surv. Prof. Pap. 1–54.

Marshall, J.A., Roering, J.J., Bartlein, P.J., Gavin, D.G., Granger, D.E., Rempel, A.W., Praskievicz, S.J., Hales, T.C., 2015. Frost for the trees: Did climate increase erosion in

unglaciated landscapes during the late Pleistocene? Sci. Adv. 1, e1500715–e1500715. doi:10.1126/sciadv.1500715

Mason, C.C., Fildani, A., Gerber, T., Blum, M.D., Clark, J.D., Dykstra, M., 2017. Climatic and anthropogenic influences on sediment mixing in the Mississippi source-to-sink system using detrital zircons: Late Pleistocene to recent. Earth Planet. Sci. Lett. 466, 70–79. doi:10.1016/j.epsl.2017.03.001

Métivier, F., Gaudemer, Y., 1999. Stability of output fluxes of large rivers in south and east Asia during the last 2 million years: Implications on floodplain processes. Basin Res. 11, 293–303. doi:10.1046/j.1365-2117.1999.00101.x

Miall, A., 1985. Architectural-Element Analysis : A New Method of Facies Analysis Applied to Fluvial Deposits. Earth Sci. Rev. 22, 261–308.

Nishiizumi, K., Imamura, M., Caffee, M.W., Southon, J.R., Finkel, R.C., McAninch, J., 2007. Absolute calibration of 10Be AMS standards. Nucl. Instruments Methods Phys. Res. Sect. B Beam Interact. with Mater. Atoms 258, 403–413. doi:10.1016/j.nimb.2007.01.297

Norris, T.L., Gancarz, A.J., Rokop, D.J., Thomas, K.W., 1983. Half-life of26Al. J. Geophys. Res. 88, B331. doi:10.1029/JB088iS01p0B331

Oskin, M.E., Longinotti, N.E., Peryam, T., Dorsey, B., Deboer, C., n.d. Steady 10 Be-derived paleo-erosion rates across the Plio-Pleistocene climate transition , Fish Creek-Vallecito basin , California. J. Geophisical Res.

Oswald, J.A., Wesnousky, S.G., 2002. Neotectonics and quaternary geology of the Hunter Mountain fault zone and Saline Valley region, Southeastern California. Geomorphology 42, 255–278. doi:10.1016/S0169-555X(01)00089-7

Painter, C.S., Carrapa, B., DeCelles, P.G., Gehrels, G.E., Thomson, S.N., 2014. Exhumation of the North American Cordillera revealed by multi-dating of Upper Jurassic-Upper Cretaceous foreland basin deposits. Bull. Geol. Soc. Am. 126, 1439–1464. doi:10.1130/B30999.1

Paola, C., 2000. Quantitative models of sedimentary basin filling. Sedimentology. doi:10.1046/j.1365-3091.2000.00006.x

Paola, C., Heller, P.L., Angevine, C.L., 1992. The large scale dynamics of grain size variation in alluvial basins, 1: Theory. Basin Res. doi:10.1111/j.1365-2117.1992.tb00145.x

Phillips, F.M., 2008. Geological and hydrological history of the paleo – Owens River drainage since the late Miocene. History 2439, 1–36. doi:10.1130/2008.2439(06).

Portenga, E.W., Bierman, P.R., 2011. Understanding earth's eroding surface with 10Be. GSA Today 21, 4–10. doi:10.1130/G111A.1

Puchol, N., Charreau, J., Blard, P., Lavé, J., Dominguez, S., Pik, R., Saint-carlier, D., ASTER Team, 2016. Limited impact of Quaternary glaciations on denudation rates in central Asia. Geol. Soc. Am. Bull. 1–21. doi:10.1130/B31475.1

Romans, B.W., Castelltort, S., Covault, J.A., Fildani, A., Walsh, J.P., 2016. Environmental signal propagation in sedimentary systems across timescales. Earth-Science Rev. 153, 7–29. doi:10.1016/j.earscirev.2015.07.012

Schaller, M., Von Blanckenburg, F., Veldkamp, a., Tebbens, L. a., Hovius, N., Kubik, P.W., 2002. A 30 000 yr record of erosion rates from cosmogenic 10Be in Middle European river terraces. Earth Planet. Sci. Lett. 204, 307–320. doi:10.1016/S0012-821X(02)00951-2

Smith, R.S.U., 1976. Late Quaternary Pluvial and Tectonic History of Panamint Valley, Inyo and San Bernardino Coutnies, California. California Institute of Technology.

Snyder, N.P., Hodges, K. V., 2000. Depositional and tectonic evolution of a supradetachment basin: 40Ar/39Ar geochronology of the Nova Formation, Panamint Range, California. Basin Res. 12, 19–30. doi:10.1046/j.1365-2117.2000.00108.x

Sømme, T.O., Helland-Hansen, W., Martinsen, O.J., Thurmond, J.B., 2009. Relationships between morphological and sedimentological parameters in source-to-sink systems: a basis for predicting semi-quantitative characteristics in subsurface systems. Basin Res. 21, 361–387. doi:10.1111/j.1365-2117.2009.00397.x

Steckler, M.S., Mountain, G.S., Miller, K.G., Christie-Blick, N., 1999. Reconstruction of Tertiary progradation and clinoform development on the New Jersey passive margin by 2-D backstripping. Mar. Geol. 154, 399–420. doi:10.1016/S0025-3227(98)00126-1

Stock, G.M., Anderson, R.S., Finkel, R.C., 2005. Rates of erosion and topographic evolution of the Sierra Nevada, California, inferred from cosmogenic26Al and10Be concentrations. Earth Surf. Process. Landforms 30, 985–1006. doi:10.1002/esp.1258

Stock, G.M., Ehlers, T. a., Farley, K. a., 2006. Where does sediment come from? Quantifying catchment erosion with detrital apatite (U-Th)/He thermochronometry. Geology 34, 725–728. doi:10.1130/G22592.1

Stone, J.O., 2000. Air pressure and cosmogenic isotope production 105, 23,753-23,75.

Swift, D.J.P. and Thorne, J.A., 1991. Sedimentation on Continental Margins, I: a General Model for Shelf Sedimentation, Shelf and Sandstone Bodies: Geometry, Facies, and Sequence Stratigraphy. The International Association of Sedimentologists.

Syvitski, J.P.M., Milliman, J.D., 2007. Geology , Geography , and Humans Battle for Dominance over the Delivery of Fluvial Sediment to the Coastal Ocean. J. Geol. 115, 1–19.

Thatcher, W., Savage, J.C., Simpson, R.W., 2016. The Eastern California Shear Zone as the northward extension of the southern San Andreas fault. J. Geophys. Res. Solid Earth n/a-n/a. doi:10.1002/2015JB012678

Tucker, G.E., Slingerland, R., 1997. Drainage basin responses to climate change. Water Resour. Res. 33, 2031. doi:10.1029/97WR00409

Val, P., Hoke, G.D., Fosdick, J.C., Wittmann, H., 2016. Reconciling tectonic shortening, sedimentation and spatial patterns of erosion from 10Be paleo-erosion rates in the Argentine Precordillera. Earth Planet. Sci. Lett. 450, 173–185. doi:10.1016/j.epsl.2016.06.015

Vogel, M.B., Jayko, A.S., Wooden, J.L., Smith, R.S.U., 2002. Quaternary exhumation rate Central Panamint Range, California from U–Pb Zircon Ages. Abstracts with Programs, Geological Society of America 34, 249.

Von blanckenburg, F., 2006. The control mechanisms of erosion and weathering at basin scale from cosmogenic nuclides in river sediment. Earth Planet. Sci. Lett. 242, 224–239. doi:10.1016/j.epsl.2005.11.017

Wheeler, H.E., 1958. Time-stratigraphy. Am. Assoc. Pet. Geol. Bull. 42, 1047–1063.

Whipple, K.X., Meade, B.J., 2006. Orogen response to changes in climatic and tectonic forcing. Earth Planet. Sci. Lett. 243, 218–228. doi:10.1016/j.epsl.2005.12.022

Whittaker, A.C., Boulton, S.J., 2012. Tectonic and climatic controls on knickpoint retreat rates and landscape response times. J. Geophys. Res. Earth Surf. 117, 1–19. doi:10.1029/2011JF002157

Wolkowinsky, A.J., Granger, D.E., 2004. Early Pleistocene incision of the San Juan River, Utah, dated with 26Al and 10Be. Geology 32, 749. doi:10.1130/G20541.1

Yanites, B.J., Tucker, G.E., Anderson, R.S., 2009. Numerical and analytical models of cosmogenic radionuclide dynamics in landslide-dominated drainage basins. J. Geophys. Res. Earth Surf. 114. doi:10.1029/2008JF001088

Zhang, P., Ellis, M., Slemmons, D.B., Mao, F., 1990. Right-lateral displacements and the Holocene slip rate associated with prehistoric earthquakes along the Southern Panamint Valley Fault Zone: Implications for southern Basin and Range tectonics and Coastal California deformation. J. Geophys. Res. 95, 4857. doi:10.1029/JB095iB04p04857

Appendix 3.1 Supplementary Figures

Supplementary Figure S3.1: Clasts of augen gneiss (World Beater complex).

Supplementary Figure S3.2: Syndepositional normal faulting in north wall of Middle Park Canyon.

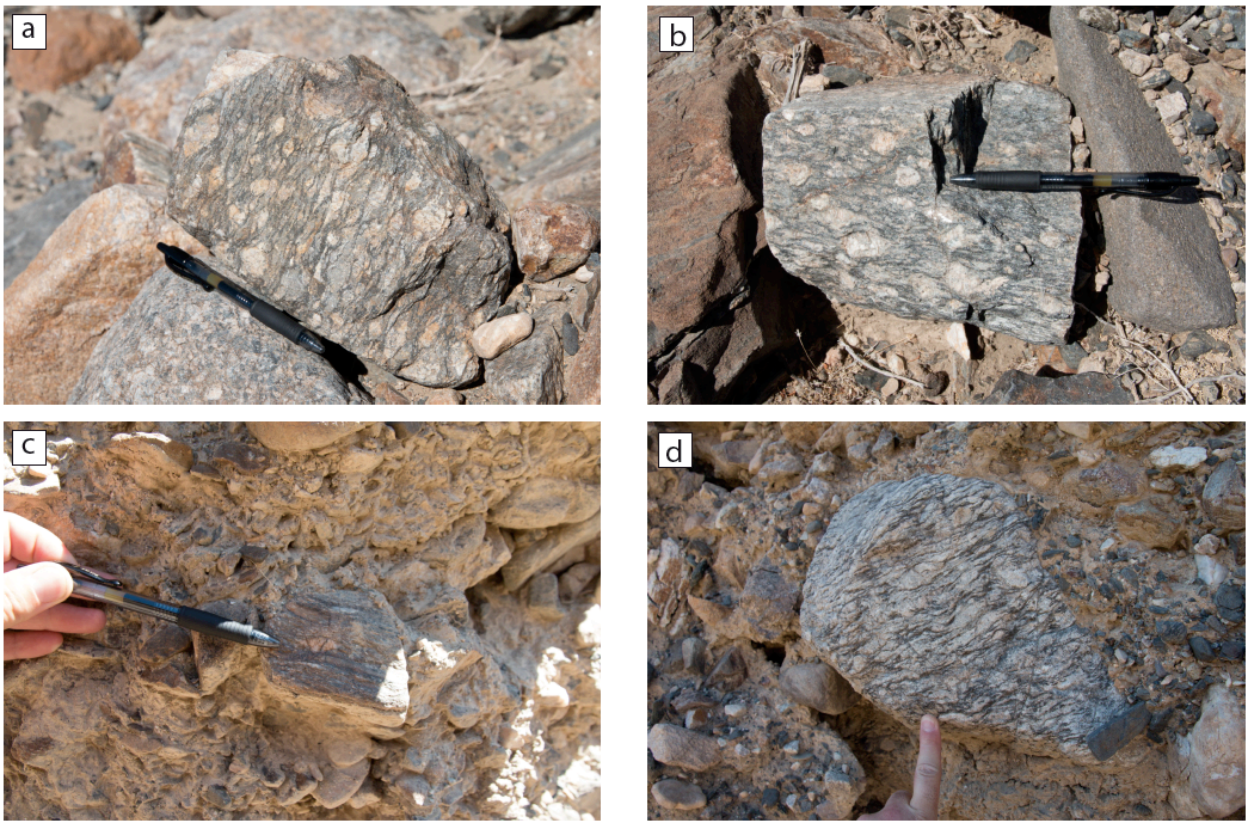

Supplementary Figure S3.1: Clasts of augen gneiss (World Beater complex) unique to the Pleasant Canyon catchment are found throughout measured sections of the Pleasant Canyon complex, in float and in-situ within outcrops. **a**, **b**: Well-formed feldspar augen porphyroblasts in clasts of World Beater found in float in section 1. **c**, **d**: Examples of World Beater clasts found in outcrop in section 1.

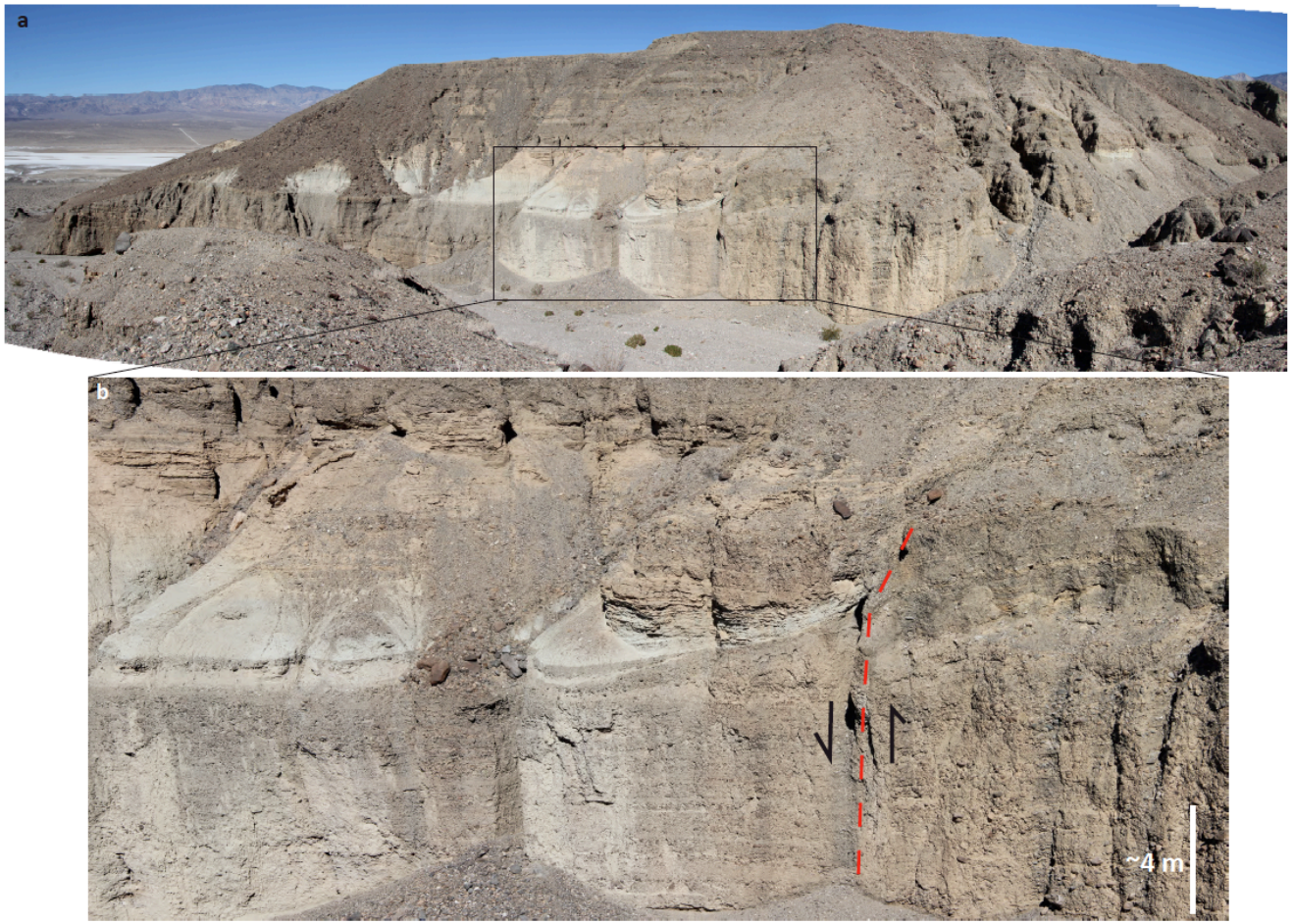

Supplementary Figure S3.2: **a**: Syndepositional normal faulting in north wall of Middle Park Canyon, just south of section one. **b**: three to five meters of throw on a steep normal fault, down toward the basin in photo. Subsidence via active faults in part explains the expanded lacustrine strata in southern Pleasant Canyon complex.